Reasearch Task

Czech
Technical
University
in Prague

F4

Faculty of Nuclear Sciences and Physical Engineering
Department of Physics

Electromagnetic properties of moons and planets

Daniel Procházka

Supervisor: Dr. Ing. Pavel Trávníček
September 2021

Acknowledgements

I would like to express my sincere gratitude for the supervision of Dr. Ing. Pavel Trávníček. Without him providing me the simulation code which he is an author of, and his support, this thesis would not have been possible.

Declaration

Abstract

The interaction of Moon and other moons and planets with surrounding plasma (solar wind or magnetospheric plasma) is influenced by their electromagnetic properties. I have tried to investigate how layers with different conductivity influence the interaction, as well as how a relative drift of ion species of incident plasma influence it. 2D and 3D hybrid numerical simulations of the interactions were used to study this interaction. Different models were created to study the influence of the chosen implementation on the simulation. Without temporal evolution of the external magnetic field, only a highly resistive crust has an impact on the interaction – there are perturbations along the surface of the Mach cone. In the case of 2 species, the interaction is mostly driven by the majority specie.

Keywords: solar wind, Moon, hybrid simulation

Supervisor: Dr. Ing. Pavel Trávníček
/stav fyziky atmosféry Akademie věd
České republiky

Abstrakt

Interakce Měsíce a jiných měsíců a planet s okolním plazmatem (tj. sluneční vítr či magnetosférické plazma) je ovlivněna jejich elektromagnetickými vlastnostmi. Práce se zabývá tím, jak vrstvy s různou vodivostí ovlivňují interakci a také jak ji ovlivňuje vzájemný pohyb dvou specií iontů v plazmatu. Ke studiu interakce byly použity 2D a 3D hybridní numerické simulace. Byly vyvinuty různé modely ke studiu vlivu volby implementace na simulaci. Bez časového vývoje vnějšího magnetického pole má vliv jen vysoce vodivá měsíční kůra – vyskytnou se perturbace na povrchu Machova kuželu. V případě dvou specií je interakce podřízena převládající specii.

Klíčová slova: sluneční vítr, Měsíc, hybridní simulace

Překlad názvu: Elektromagnetické vlastnosti měsíců a planet

Contents

Figures

Tables

Chapter 1

Introduction

Electromagnetic properties of moons and planets play a significant role in their interaction with plasma that surrounds them. The plasma can be of stellar origin – as is the case of solar wind interaction with Mercury, Earth, Moon, Mars, etc., or it can be a plasma of a different origin (e. g. volcanic) trapped within a magnetosphere of a large planet. This is the case of Galilean moons that interact with plasma torus within Jovian magnetosphere.

The existence of a planetary dynamo, the conductivity of the planets' constituents, the density of the ionosphere, and remanent magnetization of crustal rocks – these are the electromagnetic properties contributing to the interaction. Measurements of the surrounding plasma and the magnetic field provides us information about the moons' and planets' composition. In case of Europa, this meant revealing the information that there is a conductive liquid ocean under its frozen surface.

The aim of this work is to study this interaction by employing a hybrid numerical model for the case of Lunar interaction with solar wind. Moon has a conducting metal core and a highly resistive crust. Temporal changes in the external magnetic field, which is frozen in in the incident solar wind, induce eddy currents in the conducting core. This work focuses mainly on the influence of layers with differing conductivity. The influence of the relative drift of species in the solar wind is also investigated.

Chapter 2

Theoretical introduction

In this chapter, the hybrid model approximation is introduced. The theory in the following sections is relevant for the following chapters and the dimensionless parameters that are used as units in the simulation.

2.1 Hybrid Model

There are several approaches to the numerical modelling of the interaction between solar wind and bodies.

Hybrid model is a compromise between magnetohydrodynamic (MHD) description and the calculation of every particle's motion equations together with the field. The first approach is a description of velocity moments evolution and does not provide kinetic effects while the other is too computationally expensive. Hybrid model describes electrons via MHD, assuming they are mass-less fluid. The ions are simulated as macro-particles (i.e. particles representing a number of protons), which decreases computational difficulty.

In hybrid model, the fluid description of electrons is used to derive equations for electromagnetic field. The momentum equation for electron fluid is

$$m_\mathrm{e} n_\mathrm{e} \left(\frac{\partial}{\partial t} + \mathbf{u}_\mathrm{e} \cdot \boldsymbol{\nabla} \right) \mathbf{u}_\mathrm{e} = \rho_\mathrm{e} \mathbf{E} + \mathbf{j}_\mathrm{e} \times \mathbf{B} - \boldsymbol{\nabla} \cdot \mathbf{P}_\mathrm{e} - \rho_\mathrm{e} \eta \mathbf{j}. \tag{2.1}$$

It is necessary to eliminate $\mathbf{j}_\mathrm{e}$ and therefore $\mathbf{j} = \mathbf{j}_\mathrm{i} + \mathbf{j}_\mathrm{e}$ is used. From the low-frequency limit of Ampere law

$$\mu_0 \mathbf{j} = \boldsymbol{\nabla} \times \mathbf{B},$$

we substitute for $\mathbf{j}$. Next, ρ_e can be eliminated using $\rho_\mathrm{i} + \rho_\mathrm{e} = 0$. This will result in equation for electrical field:

$$\mathbf{E} = \frac{1}{\rho_\mathrm{i}} \left(-\mathbf{j}_\mathrm{i} \times \mathbf{B} + \frac{1}{\mu_0} (\boldsymbol{\nabla} \times \mathbf{B}) \times \mathbf{B} - \boldsymbol{\nabla} \cdot \mathbf{P}_\mathrm{e} \right) + \frac{\eta}{\mu_0} \boldsymbol{\nabla} \times \mathbf{B}. \tag{2.2}$$

Using $\mathbf{E}$, velocity, position and magnetic field can be stepped as:

$$\frac{\mathrm{d}\mathbf{v}}{\mathrm{d}t} = \frac{q}{m}\left(\mathbf{E} + \mathbf{v} \times \mathbf{B}\right), \tag{2.3}$$

$$\frac{\mathrm{d}\mathbf{x}}{\mathrm{d}t} = \mathbf{v}, \tag{2.4}$$

$$\boldsymbol{\nabla} \times \mathbf{E} = -\frac{\partial \mathbf{B}}{\partial t}. \tag{2.5}$$

If all the ions' trajectories were to be computed, the problem would be too difficult to solve and therefore would require too many core hours. For this reason, the equations (2.3), (2.4) are not computed for every single ion. Instead, macro-particles are used. These are imaginary particles that represent a high amount of ions (of orders of about 10^{18}). In practice, the electric field is computed and then magnetic field and macro-particle velocities and positions are. Oftentimes, the evolution of electromagnetic field is computed with a smaller time-step than the macro-particle movements.

The equation (2.2) can be simplified using more assumptions. For example, pressure isotropy ($\boldsymbol{\nabla} \cdot \mathbf{P}_\mathrm{e} = \boldsymbol{\nabla} p_\mathrm{e}$) can be assumed in some cases as a simplification . The resulting equation can be further simplified by assuming adiabatic expansion: $p_\mathrm{e} = p_{e,0}(n_\mathrm{e}/n_{e,0})^\kappa$, where κ is the Poisson constant [21].

2.2 Dimensionless parameters

Quantities in the simulation are represented in terms of dimensionless parameters. In the following paragraphs, dimensionless quantities will be denoted by a bar: $\bar{x}$ is a dimensionless version of quantity x.

In case of time, there is a motivation to capture gyration of charged particles - in the case of hybrid simulations, only ions need to be considered, because electrons are treated as fluid. It is therefore convenient to measure time in terms of gyration time, making the dimensionless time

$$\bar{t} = t\omega_\mathrm{ci}, \tag{2.6}$$

where $\omega_\mathrm{ci} = \frac{qB}{m_\mathrm{i}}$ is *ion cyclotron frequency.* Timestep in the simulation then needs to be chosen $\Delta\bar{t} \ll 1$ so that it captures gyration. If lengths are given in terms of *proton inertial length*

$$\Lambda = \frac{c}{\omega_\mathrm{pi}}, \tag{2.7}$$

where $\omega_\mathrm{pi} = \sqrt{\frac{n_e e^2}{m\epsilon_0}}$ is *ion plasma frequency*, i. e.

$$\bar{\mathbf{x}} = \frac{\mathbf{x}}{\Lambda}, \tag{2.8}$$

then velocity will be given in terms of Alfvén velocity:

$$\mathbf{v} = \frac{\mathrm{d}\mathbf{x}}{\mathrm{d}t} = \frac{\mathrm{d}\Lambda\bar{\mathbf{x}}}{\mathrm{d}\bar{t}}\frac{\mathrm{d}\bar{t}}{\mathrm{d}t} = \Lambda\omega_\mathrm{ci}\frac{\mathrm{d}\bar{\mathbf{x}}}{\mathrm{d}\bar{t}} = v_\mathrm{A}\frac{\mathrm{d}\bar{\mathbf{x}}}{\mathrm{d}\bar{t}}. \tag{2.9}$$

Therefore, this dimensionless velocity is also called *Alfvén Mach number*. Its value in the solar wind is a relevant parameter for the interaction. If the Alfvén Mach number of solar wind is higher than one, it means that information cannot travel against the direction of solar wind flow (or, more generally, any incident plasma) [39]. This affects shock wave formation.

Several quantities, namely ion density, ion bulk velocity and magnetic field, are in terms of their value in unperturbed solar wind:

$$\bar{n}_\alpha = \frac{n_\alpha}{n_{\alpha,\mathrm{sw}}}, \qquad \bar{\mathbf{u}}_\alpha = \frac{\mathbf{u}_\alpha}{u_{\alpha,\mathrm{sw}}}, \qquad \bar{\mathbf{B}}_\alpha = \frac{\mathbf{B}_\alpha}{B_{\alpha,\mathrm{sw}}}. \tag{2.10}$$

Dimensionless resistivity, as dimensional analysis suggests, will be

$$\bar{\eta} = \frac{\omega_{\mathrm{ci}}}{\mu_0 v_{\mathrm{A}}^2}\eta. \tag{2.11}$$

A dimensionless parameter relevant for pressure is plasma beta, $\beta_{\mathrm{p}} = p/p_{\mathrm{mg}}$. After substitution for thermodynamic and magnetic pressure, this gives

$$\beta_{\mathrm{p}} = \frac{2\mu_0}{B^2} n k_{\mathrm{B}} T = \frac{2}{\gamma}\left(\frac{c_{\mathrm{s}}}{v_{\mathrm{A}}}\right)^2, \tag{2.12}$$

where B is magnetic field induction, n is plasma density a T its temperature, γ is Poisson constant [39].

2.3 Planetary Magnetic Fields

For planetary magnetic field description, multipole expansion will be used. If the magnetic field can be approximated as a dipole, the multipole expansion of magnetic vector potential gives

$$\mathbf{A} = \frac{\mathbf{m} \times \mathbf{r}}{r^2},$$

where $\mathbf{m}$ is the magnetic dipole moment. Magnetic induction field generated by the dipole will then be

$$\mathbf{B} = \boldsymbol{\nabla} \times \mathbf{A} = \frac{1}{r^3}\left(\frac{3\mathbf{m}\cdot\mathbf{r}}{r^2}\mathbf{r} - \mathbf{m}\right). \tag{2.13}$$

In the case of more complex fields, one can start with Helmholtz magnetic field decomposition:

$$\mathbf{B} = \boldsymbol{\nabla} V + \boldsymbol{\nabla} \times \mathbf{A}. \tag{2.14}$$

Because $\boldsymbol{\nabla} \times \boldsymbol{\nabla} \equiv 0$ and $\boldsymbol{\nabla} \cdot \boldsymbol{\nabla} \times \equiv 0$, the Helmholtz decomposition gives a zero-curl part and a zero-divergence part. In order that the field solves the Maxwell equation $\boldsymbol{\nabla} \cdot \mathbf{B} = 0$, V must additionally solve Laplace equation.

The solution V can be written as $V = V^{\mathrm{i}} + V^{\mathrm{e}}$, where

$$V^{\mathrm{i}}(r,\vartheta,\varphi) = \mathrm{Re}\left\{ R \sum_{n=0}^{\infty} \sum_{m=0}^{n} \left(\frac{r}{R}\right)^{-n-1} g_n^m Y_n^m(\vartheta,\varphi) \right\}, \tag{2.15a}$$

$$V^{\mathrm{e}}(r,\vartheta,\varphi) = \mathrm{Re}\left\{ R \sum_{n=0}^{\infty} \sum_{m=0}^{n} \left(\frac{r}{R}\right)^{n} G_n^m Y_n^m(\vartheta,\varphi) \right\}, \tag{2.15b}$$

where Y_n^m are spherical harmonics, R is the planetary radius and ϑ, φ are spherical coordinates. V^{i} describes an internal part and V^{e} external one. Coefficients g_n^m, G_n^m need to be determined empirically [59].

The magnetopause location is given by the planetary magnetic field and by the solar wind conditions. It is defined as the place where the forces given by pressure gradients of the planetary magnetic field and the solar wind pressure are equal. The total pressure is

$$p = \rho u^2 + n k_{\mathrm{B}} T + \frac{B^2}{2\mu_0},$$

where the first term is the hydrodynamic pressure, the second is the thermal pressure and the third is the magnetic field pressure.

Chapter 3

Background

This chapter features a review of literature on the interaction of the solar wind with moons and planets. There are two sources of information about the interaction; the first being measured data – either in-situ (e.g. a probe mounted with magnetometers), or electromagnetic radiation measured on the Earth. A problem of in-situ measurements is the fact that a probe can not provide us with a global image of the interactions. We only have a sample on a curve – the trajectory of the probe. For determining the properties of planets or moons, it is convenient to measure during several fly-bys, as was the case with e. g. Galileo probe. The other option is to use numerical simulations, which on one hand can provide a global view on the interaction, but on the other hand use simplifications due to computational restraints. Whether a numerical model is correct can be assumed from a comparison with in-situ-measured data.

3.1 Interaction of Moons and Planets With The Solar Wind

The interaction of bodies with solar wind depends on their properties, i. e. the constitution and electromagnetic properties of the constituents, the existence of a planetary dynamo, the existence of an atmosphere, etc. Several types can be distinguished based on that.

Planets and moons with planetary dynamos produce a magnetosphere if the intrinsic magnetic field is sufficiently strong. The magnetosphere pushes the plasma away via magnetic pressure. The second type is bodies that lack a strong intrinsic magnetic field and therefore come in close contact with the solar wind plasma, either absorbing it or reflecting it. If the planet or moon has a conductive core, temporal changes in external field induce eddy currents inside it. This plays a significant role in the Hermean interaction with solar wind. Conductive ionospheres play a role as well – resulting in the so called draping of magnetic field lines. This is the case of Venus, for example.

3.2 Lunar Geological Composition

The Moon is predominantly composed by silicate minerals. As is the case for Earth, the Moon is divided into three fundamentally different layers: the crust, the mantle and the core. By studying the lunar crust, information can be gathered about the history of Solar wind thanks to the fact that the Moon absorbs vast majority of incident plasma (for more on the interaction see chap. 3.3) [38].

Information about the composition of lunar crust can be drawn from its reflectivity. The more reflective areas are composed predominantly by anorthositic rocks (anorthosite is an igneous rock) and plagioclase-rich Mg-suite rocks. Dark spots on the lunar surface are composed by basaltic rocks a pyroclastics [28].

This division, however, is a great simplification. The crust can be divided into terrans – geological units differing in their composition and properties [28]. The two largest terranes are *Procellarum KREEP Terrane* (PKT) and *Feldspathic Highlands Terrane* (FHT) [28]. FHT constitutes approximately 60 % of the lunar surface and is composed by anorthositic rocks, it also has small concentrations of thorium. PKT is composed by KREEP (= potassium, rare earth elements and phosphorus) basalts and has high thorium concentrations [28]. PKT can be mapped by measuring gamma radiation emitted by radioactive isotopes of thorium and potassium [32, e.g.]. KREEP refers exclusively to rocks formed by magma ocean crystallisation, not rock formed by meteor impacts [62]. Another important terrane is the South Pole-Aitken basin, which similarly to PKT has higher FeO concetrations than FHT, but is poorer in thorium than PKT [28].

Moreover, the crust contains magnetized areas (more about their origin and interaction with the solar wind can be found in chap. 3.3).

The interface between an (arbitrary planet's) crust and a mantle is called the Mohorovčić discontinuity and can be determined seismologically by measuring the propagation of longitudinal waves. In the case of the Moon, there are seismometers placed during Apollo 12, 14, 15 and 16 missions. For example near the Apollo 12 and 14 landing site, under Mare Cogitum, the crust is thought to be approximately 58 km thick as was deduced from the inversion of longitudinal wave propagation time [46]. Other measurements pointed at a discontinuity at approximately 20 km [62]. The crust's thickness was also investigated through its impedance [5]. Based on this data the authors of [62] have proposed three models for the lunar crust. One of them includes a further division of the crust into lower and upper crust. They can be seen in tab. 3.1.

Lunar earthquakes do not allow a seismologic investigation of depths of more than 1200 km ($\approx 0{,}7 R_\mathrm{M}$, where $R_\mathrm{M} = 1737$ km is the lunar radius) [28]. However, meteor impacts were analysed as well. From these, conclusions have been drawn on the thickness of the crust ($50 - 60$ km), the upper mantle (250 km), and the core ($170 - 360$ km) [45]; where the upper mantle is composed predominantly by orthopyroxene and the lower by olivine. The

	Model 1	Model 2	Model 3
Reference crust thickness [km]	53,4	43,4	52,0
Reference upper crust thickness [km]	—	—	26,9

Table 3.1: Overview of Lunar crustal models in [62].

mantle may be partially molten beneath 1000 km [62].

The dimensions of the core can be determined by measuring the electric dipole induced by changes in the external magnetic field – either on Moon's orbit around the Earth, or its orbit around the Sun. Induced magnetic dipole moment of $(-2{,}4 \pm 1{,}6) \cdot 10^{23}\ \mathrm{A\,m^2\,T^{-1}}$ was determined from the Lunar Prospector Probe data, which hints at a core with a radius of 340 ± 90 km (assuming very high conductivity of the core and currents being induced on the core's surface) [24].

A resistivity profile of the Moon was determined from transient effects by magnetometers on board Explorer 35, Apollo 12, 15 and 16. Lunar crust is an insulator [8]. Resistivity of $\sigma(r) \approx 10^{-2}\ \mathrm{S\,m^{-1}}$ was determined for $0 < r < 0{,}6R_{\mathrm{M}}$ and $\sigma(r) \approx 10^{-4}\ \mathrm{S\,m^{-1}}$ for $0{,}6R_{\mathrm{M}} < r < 0{,}95R_{\mathrm{M}}$, where r is the distance from the center of Moon and $R_{\mathrm{M}} = 1737$ km is lunar radius [8]. A more detailed description can be seen in graph in Fig. 3.1.

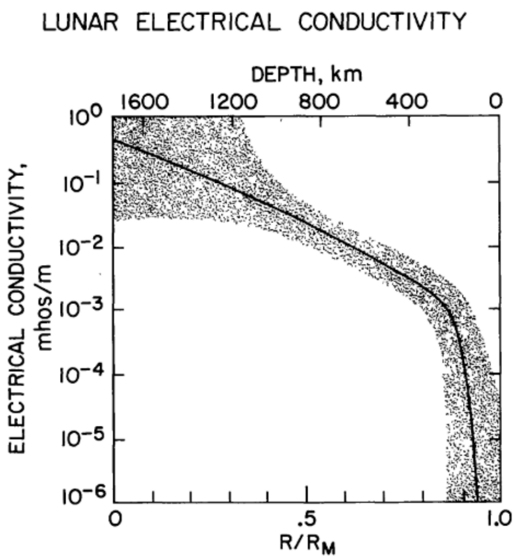

Figure 3.1: Lunar conductivity profile; source: [8]. (Note: $\mathrm{mhos/m} = \mathrm{S\,m^{-1}}$)

A temperature profile of the Moon can be estimated by measuring its conductivity. Most minerals are semi-conductors. Thus, conductivity is given by the number of electrons that transition from a valence band do the conduction band. At absolute zero, the conduction band is empty. With growing temperature, the conduction band is filled by electrons. In general, one can write

$$\sigma = \sum_n \sigma_{0,n} \exp\left\{\left(-\frac{E_n}{k_\mathrm{B}T}\right)\right\},$$

where $\sigma_{0,n}$ is given by electron mobility depending on the material properties and changing only slightly with temperature.

Even though crystal conductivity is usually anisotropic, crystals in rocks are not all oriented in the same direction. Therefore the conductivity of the rock as a whole will be a scalar, not a tensor [53].

3.3 Interaction Between the Moon and the Solar Wind

The interaction of the solar wind with the Moon is different from that with the Earth. Because the Moon lacks a strong magnetic field and an atmosphere, most of the incident plasma is absorbed by its surface. Field perturbations are bounded by the *magnetosonic Mach cone.* Furthermore, the field is perturbed because of plasma compression [14].

3.3.1 First Look at the Interaction

In a first order approximation, the Moon can be assumed to be a resistive obstacle absorbing all incident plasma [14]. The Moon creates a cavity in the plasma in its wake. The shape of the lunar wake depends on the parameters of the solar wind and the interplanetary magnetic field (IMF). If the bulk velocity of the solar wind is larger than the thermal velocity, then the cavity will reach further in the wake. The bigger the thermal velocity relative to the bulk velocity, the faster the lunar cavity will be filled, and therefore the cavity region will be shorter [44]. If we account for IMF, the interaction will be more complicated. If the magnetic field lines are parallel to the solar wind flow, they will prevent the cavity from being filled [44].

In Fig. 3.2, a density graph can be seen in the model of [21] for three different IMF configurations, where the coordinates were chosen so that the solar wind flows in the $-x$ direction and the $\mathbf{B}_\mathrm{IMF}$ vector lines in the xy plane, the z axis is chosen in such a way that it completes x, y to a right-handed set (x, y, z). Fig. 3.2(c) and 3.2(d) show sections perpendicular to x-axis for $x = -10000$ km and $x = -30000$ km, respectively. Another phenomenon worth mentioning is a rarefied plasma cone. For perpendicular IMF it only extends in the z-direction. In these regions, weaker magnetic field is present as well [21].

Lunar wake currents were examined in a hybrid model [11]. Moon is considered non-conductive in the model. As was already mentioned above in chap. 2.1, in hybrid models, displacement current is neglected. Therefore $\mu_0\mathbf{j} = \boldsymbol{\nabla} \times \mathbf{B}$. Thus, currents are directly linked to magnetic field perturbations. There are three currents in the wake of a non-conductive Moon:

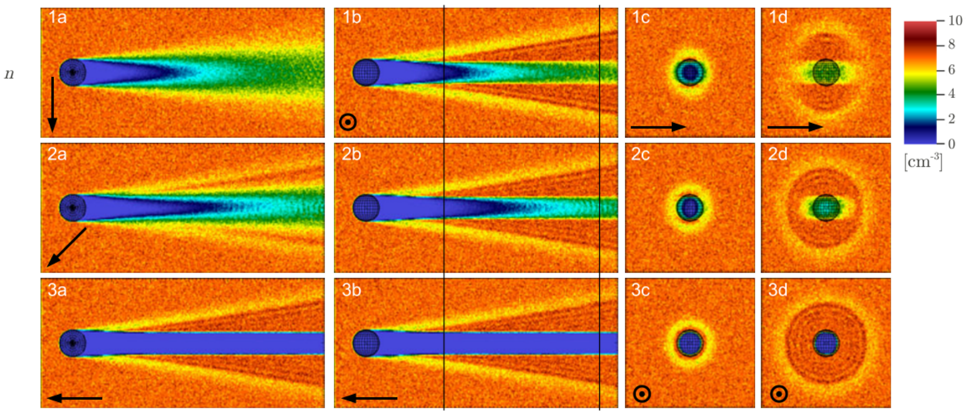

Figure 3.2: Ion density graph in the hybrid model of (non-conducting, particle-absorbing) Moon–SW interaction for various IMF orientations. Displayed sections are: (a) xy-plane, (b) xz-plane, (c) resp. (d) yz-planes for $x = -10000$ km resp. $x = -30000$ km; source: [21]

diamagnetic current $\mathbf{j_1}$ around plasma void, and currents around the rarefaction region ($\mathbf{j_2}$) and around the recompression region ($\mathbf{j_3}$). They can be seen on a diagram in fig. 3.3 for two cases: IMF perpendicular and parallel to solar wind flow. The authors looked at the situation in early simulation time – before macro-particles reached the outer boundary of the simulation domain – in order to determine if the currents are closed in case of IMF perpendicular. In this case, the currents are closed [11]. It is therefore reasonable to assume that the currents are in the case of real Moon closed in the far wake.

3.3.2 Induced Lunar Magnetic Dipole

In the last section, the Moon was assumed to be ideally non-conducting. In the case of a non-conductive body, the magnetic field diffuses through it quickly and thus the magnetic field is perturbed only negligibly by such an obstacle. If a conductive lunar core is taken into account, the situation becomes slightly more complicated. Currents will be induced inside the lunar core, which results in magnetic dipole induced in direction opposite to that of the external field [44].

Because the lunar core is not ideally conductive, the induced dipole will be suppressed in the case of stationary external field. The magnetic field will diffuse with the diffusion time

$$\tau = R^2 \mu_0 \sigma, \tag{3.1}$$

where R is the core's radius, σ is its conductivity and μ_0 is the magnetic permeability of vacuum.

When the magnetic field is changing quicker than τ, the previous holds true. In the case of slower changes, the field will penetrate into the core. A value of $\tau = 1000$ yrs is estimated for Moon [44]. We can therefore assume

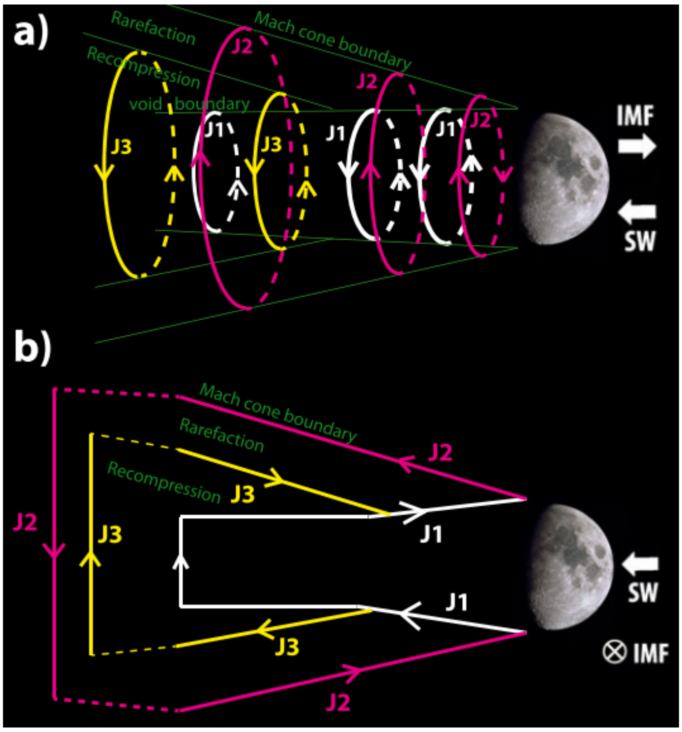

Figure 3.3: Currents in the lunar wake for IMF parallel (a) and perpendicular (b) to the flow of the solar wind. Source: [11]

the lunar core to be ideally conductive. In such core, the induced field will be

$$\mathbf{B}_{\text{ind}}(\mathbf{r}, t) = \frac{\mu_0}{4\pi} \left(\frac{3\mathbf{M}(t) \cdot \mathbf{r}}{r^5} \mathbf{r} - \frac{1}{r^3} \mathbf{M}(t) \right), \tag{3.2}$$

where

$$\mathbf{M}(t) = -\frac{2\pi}{\mu_0} \mathbf{B}_0(t) r_0^3,$$

where $\mathbf{B}_0(t)$ is the external magnetic field and r_0 is the radius of an infinitely-conductive core [52].

The interaction between SW and the Moon with an induced dipole was studied by a hybrid code [10].

Based on IMF data gathered by ARTEMIS probes, magnetic dipole moments of magnitudes $10^{15} - 10^{17}$ A m^2 were placed in the origin of the coordinate system. In fig. 3.4, there are graphs of magnetic fields in simulation (#A1, #B1) and with a magnetic moment of magnitude $||\mathbf{M}_{\text{ind}}|| = 10^{16}$ A m^2 (#A2, #B2). They concluded that even though on the day-side does not cause magnetic field perturbations, the wake is perturbed and the perturbations are not bound by a Mach cone [10]. This can be seen in fig. 3.4(i,j,k,l), where brighter colours symbolise stronger perturbations. The mach cone is denoted by a white dashed line.

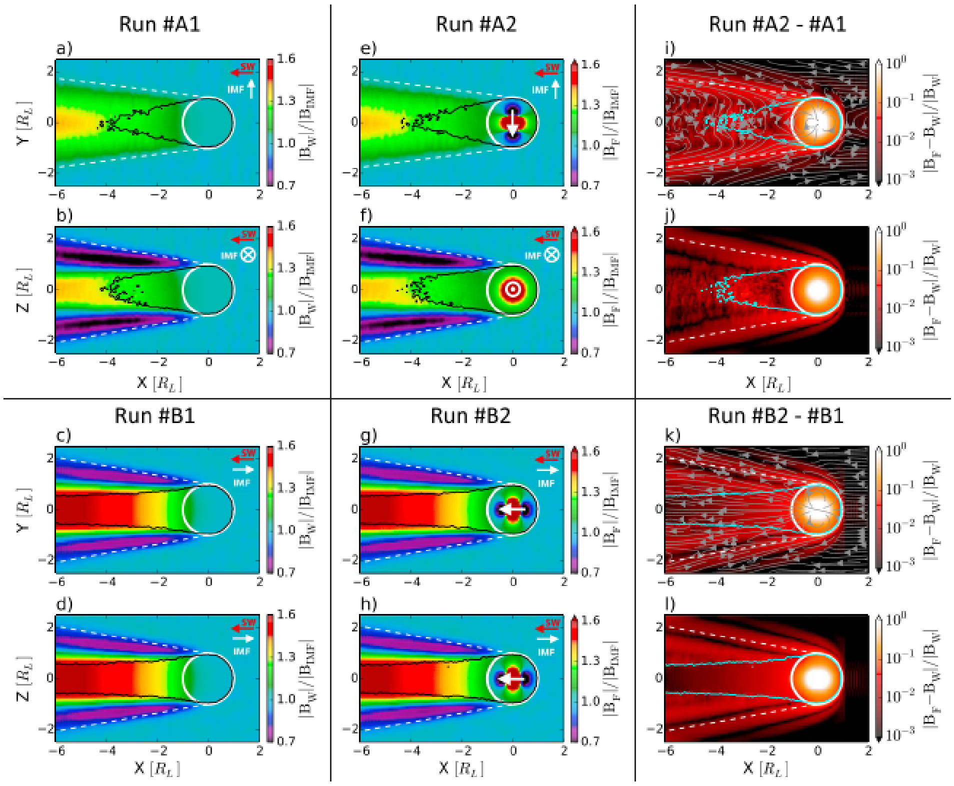

Figure 3.4: Graphs of the magnetic field in simulations without an induced dipole field (#A1, #B1) and with an induced dipole moment of 10^{16} A m^2 (#A2, #B2). Source: [10]

3.3.3 Lunar Crustal Magnetic Fields

Magnetised rocks in the lunar crust constitute magnetic anomalies. The largest are the South Pole/Aitken basin (SPA), Mare Marginis and the Gerasimovich anomaly [48].

In the plasma above magnetic anomalies, disturbances occur. The dipole-generated field only reaches in an area that is thinner than proton inertial length Λ [58]. Under the assumption of $\mathbf{M}$ perpendicular to the solar wind flow, by using (3.2) we obtain

$$x^3 = \frac{\mu_0}{4\pi}\frac{M}{B}.$$

If we are interested in the position of a magnetopause, we need to consider the equality of magnetic field and hydrodynamic plasma pressures, hence

$$\rho v^2 = \frac{B^2}{2\mu_0},$$

which after substitution to previous equation gives

$$L = \sqrt[6]{\frac{\mu_0 M^2}{16\pi^2 m_i n_0 v^2}}, \tag{3.3}$$

where n_0 is the plasma density in the undisturbed solar wind, v its velocity, M magnetic dipole moment in the anomaly. For lunar crustal anomalies this gives [58] $L < 100\,\mathrm{km}$.

Anomalies have probably originated as a result of meteor impacts onto lunar surface. They exist on the antipodal side of Moon than lunar maria, which have originated by impacts [41, 25]. An exception to that is the South Pole/Aitken (SPA), whose antipodes do not constitute magnetic anomalies. This may have been caused by later Mare Imbrium formation [23]. Another exception is an anomaly near the Descartes crater [25]. It probably constitutes Mare Imbrium ejecta, which is supported e.g. by a similar geological age [25, 47].

There are different theories about the anomalies' origin. The magnetic anomalies could have been created by the effects of a "planetary" dynamo or due to plasma created by impacts of meteors onto the lunar surface [61]. A planetary dynamo probably was present in the Moon until about 3.2 billion years ago, paleomagnetic studies suggest [55, 61].

The more probably cause seem to be the meteor impacts, because the Moon could not have such strong magnetic field given its size [23, 53]. By simulating the vapours after meteor impacts it was shown that a temporary magnetic field created by the impacts affected crustal magnetization and that the effect was the strongest in the place opposite to the point of impact [23].

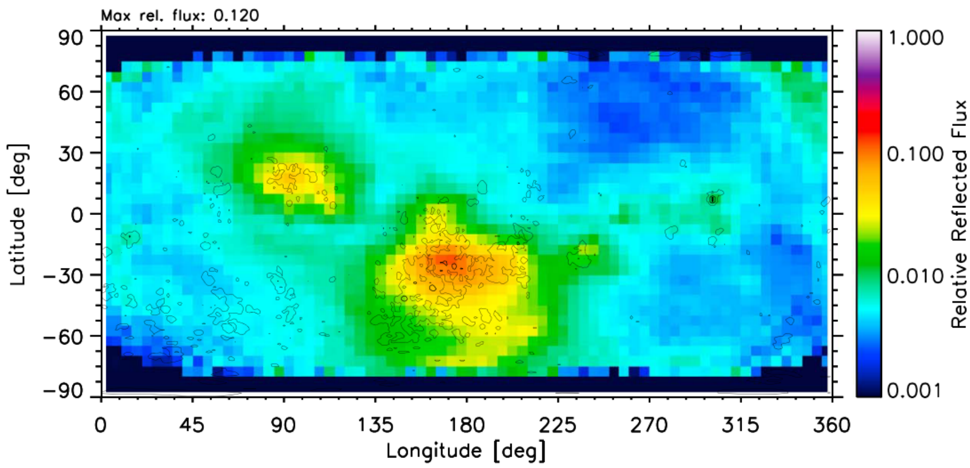

Figure 3.5: Selenographic map of reflected proton flux. Source: [48].

The magnetic fields of the anomalies reflect some of the incident protons [48]. The question remains what is the nature of this reflection.

The authors of [22] have found $\cos^2$-specular (i.e. the angle φ of reflection is a random variable with density $\cos^2\varphi$) to be in a good agreement with the data, on the other hand the global image of the interaction is not sensitive to the choice of the probability density function [14]. Using Liouville backtracing, the probability density $f^{(\phi,\vartheta)}(v,\chi,\psi)$, where (ϕ,ϑ) are selenographic coordinates, was found from data acquired from ARTEMIS (= Acceleration, Reconnection, Turbulence and Electrodynamics of the Moon's Interaction with the Sun) probe [48].

The crustal magnetic anomalies affect the surrounding plasma. Some of the anomalies seem to have fields strong enough to give rise to a mini-magnetosphere, as was induced from the existence of a shock wave above Mare Ibrium antipode [41]. Magnetohydrodynamic waves were also found above the anomalies [41].

Measurements conducted by the SWIM (Solar Wind Monitor) detector on-board the Chandrayaan-1 probe show that above anomalies, on average 10 % of protons are reflected, with local values up to 50 % [43]. Map showing reflected proton flux as a function of selenographic coordinates can be seen in Fig. 3.5. The reflected protons then fill the lunar wake [14].

A precise proton reflection mechanism is not yet known. One of the issues is a complicated topology of the anomalies' fields. An analysis of ions, electrons and energetic neutral atoms (ENA) detected by Kaguya probe has shown that electrostatic potential of up to 150 V appears in the height of 25 km [51]. It is given by the ions penetrating deeper into the fields than the lighter electrons. The charge separation gives rise to electric field [15]. ENA spectrometer on-board Chandrayaan-1 confirmed electrostatic potential of more than +135 V [16]. The interaction with the Gerasimovich anomaly was studied in detail via a hybrid model [15, 27]. The Gerasimovich anomaly can be easily studied by numerical simulations, because it has a simple structure despite being of the strongest known anomalies. Using the approximation of the field as a dipole field, the potential was shown to be a consequence of the Hall effect. The simulation resulted in $V < 300$ V, in accordance with previous measurements [27]. A more detailed structure was used in [15]. For magnetic field, scalar magnetic potential was used. The potential was expressed as a linear combination of spherical harmonics ($N = 170$)

$$V(r, \vartheta, \varphi) = R_{\mathrm{M}} \sum_{n=1}^{N} \left(\frac{R_{\mathrm{M}}}{r}\right)^{n+1} \sum_{m=0}^{n} (g_n^m \cos(m\varphi) + h_n^m \sin(m\varphi)) P_n^m(\cos\vartheta),$$

according to (2.15a).

Where (r, ϑ, φ) are spherical coordinates on lunar surface and P_n^m are associated Legendre polynomials. The coefficients g_n^m, h_n^m were taken from [49]. The field was shown to be affected by solar wind, e.g. in the case of a high dynamic pressure, the fields are compressed [15]. The mini-magnetosphere depends on the dynamic pressure of the solar wind. The potential sufficient to plasma shielding has a magnitude of

$$\varphi_S = -\frac{B_{\mathrm{m}}^2}{4e\mu_0 n_{\mathrm{SW}}},$$

where B_{m} is the magnitude of the magnetic filed of the anomaly, n_{SW} is solar wind density [15]. In the case of high dynamic pressure, magnetic anomalies are suppressed.

3.4 Galilean Moons

The size of the magnetospheric cavity is, according to equation (3.3), proportional to the sixth root of the ratio of magnetic moment squared to hydrodynamic solar wind pressure. The pressure is inversely proportional to the distance from Sun squared. This, combined with the fact that Jovian magnetic moment is larger than that of Earth, means that Jovian magnetosphere is very large relative to Earth's. All Galilean moons lie within it, which means they are shielded from solar wind and interact with Jovian magnetospheric plasma. The strongest source of Jovian magnetospheric plasma is the moon Io, whose atmosphere is maintained by volcanic activity [50]. The magnetospheric plasma is linked to Jovian ionosphere via field-aligned currents (FACs). As a result, it corotates with Jupiter – i.e. rotates with a period of about 10 h. In the outer regions of the Jovian magnetosphere, the plasma lags in rotation [39]. The incident plasma velocity is sub-alfvénic in the rest frame of each Galilean moon. This is a major difference from interactions between the solar wind and other moons and planets.

3.4.1 Ganymede

Ganymede is located inside inner Jovian magnetosphere, where the plasma energy density consists primarily of magnetic energy [39]. Ganymede probably has a metal core with radius 400 − 1300 km surrounded by silicate mantle, the surface is covered by ice crust approximately 800 km thick, which is an estimate based on gravitational measurements [3].

Ganymede's most important feature is its internal magnetic field. It is the only known moon in the Solar system with this property. Its magnetic dipole moment was measured by Galileo probe. It is sufficiently big to support a mini-magnetosphere embedded inside Jovian magnetosphere [35]. Ganymede's magnetic dipole moment is oriented opposite (176°) to its rotational axis [37]. This results in magnetic field line reconnection. Because the mini-magnetosphere is embedded in Jovian magnetosphere, it allows us to study reconnection under known, stable conditions [31].

As mentioned earlier, Ganymede interacts with plasma inside Jovian magnetosphere. This plasma corotates with Jupiter and thus rotates faster than Ganymede. The relative velocity of the corotating plasma with respect to Ganymede is smaller than both magnetosonic Mach velocity and Alfvén velocity [30].

Ganymedean magnetosphere has several distinct features which result from the small velocity of the incident plasma and the fact that it is embedded within Jovian magnetosphere. Ganymede lacks a bow shock [35]. Its Alfvén wings are nearly perpendicular to the plasma flow [35]. With super-alfvénic plasma flow the magnetosphere would have a bullet shape, because it would be confined by the hydrodynamic pressure $p \approx \rho v^2$ of solar wind (or any arbitrary plasma). In the case of Ganymede, the external pressure is $p \approx p_{\mathrm{mg}} = B^2/2\mu_0$, which sustains the magnetosphere perpendicular to rotational axis and its action on the magnetosphere is approximately axially symmetrical. In the case of $p \approx \rho v^2$, the external pressure force is direction-dependent, which results in the non-symmetrical bullet shape [39].

As a result of the Jovian magnetic dipole moment tilt with respect to the rotational axis of about 10°, the environment surrounding Ganymede varies. Two basic configurations can be distinguished. When Ganymede is inside Jovian plasma sheet, the plasma density is high and typically plasma beta $\beta_\mathrm{p} > 1$. When Ganymede is outside of it, the plasma density is small and $\beta_\mathrm{p} < 1$ [39]. Periodical changes in the external magnetic field allow for induced currents inside Ganymede's conducting layers (for analogy with Moon, see 3.3.2).

The possibility of an induced dipole moment was investigated by fitting magnetometer data gathered by Galileo probe during G1, G2, G7, G8, G28 and G29, using two theoretical models. The following two options were considered:

a) Ganymede has a permanent dipole moment and a permanent quadrupole moment,

b) Ganymede has a permanent dipole moment and an induced one.

The induced dipole is a good assumption, because other Galilean moons, namely Europa and Callisto, posses it as a result of changes in external magnetic fields as they orbit Jupiter. Contrary to Ganymede, they do not have a permanent magnetic dipole [36]. A boundary condition for the surface of Ganymede is consistent with an induced dipole with the magnetic field being $B = 100$ nT on the poles (and 50 nT on the equator). The magnetic dipole is oriented anti-parallel to field which is changing in the axis Jupiter-Ganymede. It is therefore approximately perpendicular to Ganymede's rotational axis [37]. This would suggest that Ganymede contains a conductive layer. That could be an ocean (i.e. partial melt of its icy crust) or conductive rocks [37]. Data gathered in situ by Galileo probe are consistent with both the options. Authors however prefer the option b) [37].

Because the magnetic field is inversely proportional to the cube of distance – equation(2.13), the currents induced by the external field need to be near the surface [39]. The icy crust, however, is not conductive enough (assuming that the ice is chemically similar to Earth's oceans) in the low temperatures. The crust needs to be partially molten, or near the melting point [39]. A heat source is needed. That could be a nuclear decay of elements in the mantle and core of Ganymede [39].

In the case of Ganymede there are three types of magnetic field lines. Open field lines are field lines that connect Ganymede to Jovian field lines. Closed field lines connect two point on Ganymede. The third type are Jovian magnetic field lines, which do not connect to Ganymede [37]. They can be seen in an MHD model in Fig. 3.6 [30].

Ganymede's interaction with corotating plasma has been modeled both magnetohydrodynamically [40, 26, 30, 31] and hybridly [13]. Fatemi *et al.* [13]

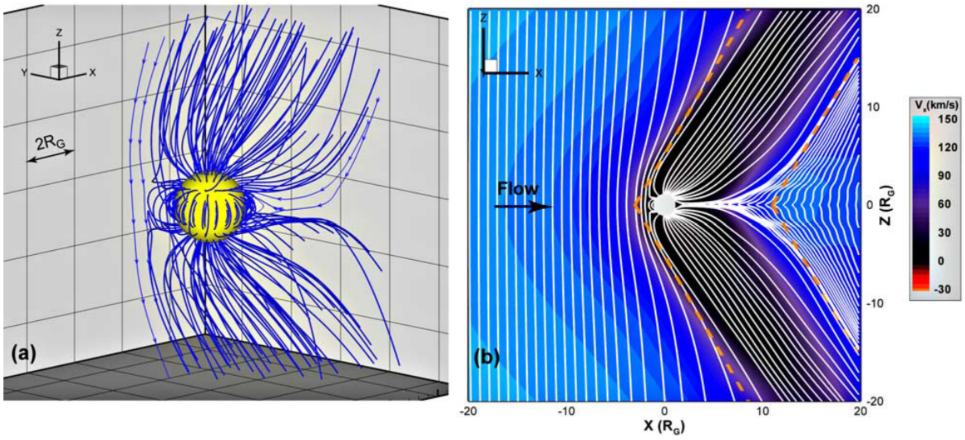

Figure 3.6: (a) 3D plot of field lines around Ganymede
(b) Plasma velocity map in the direction of undisturbed plasma flow. Orange lines show Alfvén characteristics. The white lines are magnetic field lines. Source: [30].

have studied asymmetries in particles incident on the surface of Ganymede. Closed field lines shield the surface of Ganymede, therefore in small latitudes ($-30° – 30°$) the incident particle flow is much smaller than outside [13]. The model does not take ionosphere into account, however.

Ganymede has an atmosphere and an ionosphere, which interact with the corotating plasma. Ganymede's atmosphere was discovered in 1972 thanks to the occultation of star SAO 186800. A lower bound on the atmospheric pressure above surface was set to be of order 0,1 Pa [7]. Later, from UV measurements of the occultation of κ Centauri, the upper bound was estimated to be five orders smaller than the lower bound [6], which was found to be consistent with later Hubble telescope measurements [19]. Hubble telescope also allowed to measure spectra, which led to the discovery that Ganymede's atmosphere is predominantly constitutes oxygen [19].

The atmospheric properties and its effects on the ionosphere are different in polar and equatorial regions. In the sputtering regions (as mentioned earlier, this means high latitudes), the interaction products depend on the energy of the incident ions. Temperatures in the polar regions do not allow sublimation though, and therefore all water vapour and hydroxyl released in this process recondense. Vapors of molecular oxygen are stable under these temperatures, which allows them to react with plasma through ENA [9].

In the equatorial regions, water vapour and hydroxyl can occur. After dissociation, the hydrogen has significantly higher velocity than the oxygen and there it is able to escape. This is not the case for atomic oxygen, as opposed to polar regions. This is the reason why Ganymede's ionosphere is composed of oxygen ions, but not protons [9].

The ionospheric oxygen interacts with electrons from Jovian magnetospheric plasma via three processes: $O_2 + e \rightarrow O + O + e$, $O_2 + e \rightarrow O_2^+ + e + e$, $O_2^+ + e \rightarrow O + O$. Molecular oxygen occurs primarily in polar regions, whereas in equatorial regions, atomic oxygen occurs dominantly [9].

Ganymede's interaction (including ionosphere) with the Jovian magnetospheric plasma was modeled magnetohydrodynamically (in spherical coordinates) [30, 31]. In the first case, the ionosphere was handled using boundary conditions: pressure and density have a uniform distribution which is temporally constant. The reasoning behind this is that the ionosphere is described as a reservoir filled with cold dense plasma. Next, the model had a boundary condition $\mathbf{v} = 0$ on Ganymede's surface. It was not in a good agreement with measurements [30], therefore it was improved by the authors in [31]. In the latter article, two possible boundary conditions were compared. A boundary condition that was in good agreement with data was that the component of v perpendicular to the magnetic field has to be continuous on the inner boundary ($1{,}05R_{\mathrm{G}}$ – this corresponds to the ionosphere's most conductive layer) [31]. The field inside Ganymede ($0{,}5R_{\mathrm{G}} < r < 1{,}05R_{\mathrm{G}}$) was in both cases calculated from diffusion equation [30, 31].

3.4.2 Europa

Before the first fly-bys of Galileo probe, Europa was not expected to be a source of interesting plasma phenomena. It turned out to be the case, however [39]. Europa does not have a homogeneous composition, which was inferred from gravitational measurements by Galileo probe. Europa's moment of inertia is smaller than that of a homogeneous ball. Therefore, deeper layers of Europa are denser than shallow layers. Europa has an icy crust. The mangle and the core are probably composed by silicates or iron compounds [4]. The state of the outer layer cannot be determined from these measurements however – it is unknown whether the ice is partially molten or not. A subsurface ocean would allow an induced current, which could affect Europa's interaction with the surrounding plasma.

As was mentioned earlier, Europa orbits Jupiter more slowly than the corotating Jovian plasma. The plasma thus flows from behind with respect to Europa's direction of orbit.

Similarly to Ganymede, Europa's orbit is tilted 10° with respect to the equator of Jovian magnetic dipole. Therefore, the external magnetic field surrounding Europa is harmonically changing with the period of 11,1 h (which is the synodic period of Jupiter's rotation). Next, as a result of the eccentricity ($\varepsilon = 0,009$) of Europa's orbit, the B_z component of external field is changing with period $T = 85,2$ h (which is period of Europa's orbiting) [34]. Europa is located on the outer edge of Io plasma torus, where the Jovian plasma sheet is thin. Because plasma sheet lies in the equatorial plane of Jovian dipole field, it is moving relative to Europa as Europa orbits Jupiter. The conditions are thus changing [34].

Pure water, ice, rocks and ionosphere similar to that of Earth have a skin depth bigger than Europa's dimensions for the changes in external field with period of 10 h. These materials cannot give rise to the induced fields measured by Galileo [34].

On the other hand, highly conducting materials such as magnetite, graphite or metals such as copper or iron have a small skin depth. It is however improbable for them to be abundant in Europa's icy (or partially molten) crust. A probable option is a salty oceans with conductivity similar to Earth's ocean with a thickness of the order of tens of kilometres [34].

An induced dipole field was observed in Europa [33].

Europa's interaction with plasma was observed in-situ by Galielo probe during E4, E6, E11, E12, E14, E15, E19 and E26 [36]. The interaction has the following attributes: Alfévn wing formation; induced magnetosphere; induced dipole magnetic field; magnetic field changes in the wake due to diamagnetic currents and plasma torus massloading as a result of the interaction of ions with Europa's surface [42].

For the modeling of Europa's interaction (including atmosphere) with plasma, time dependent Boltzmann equation was solved via PIC method along with hybrid model (kinetic ions, electrons as massless fluid) [42]. The Boltzmann part of the simulation was used to model the interaction between atmosphere and incident ions and pick-up ions . The result was compared to data from E4 fly-by [36], but it gave different magnetic field profile. According to the authors, this could be given by a small resolution and a small amount of macro-particles (and thus small resolution in velocity distribution) [42].

3.5 Mercury

Similarly to Earth, there is likely a planetary dynamo inside Mercury. Its magnetic field is weak compared to Earth and the dynamic pressure of the solar wind is much greater than at the level of Earth because of its proximity. Similarly to Earth, collision-less shock wave is formed at Mercury [1]. There are however many differences in the systems. Some processes in Mercury's magnetosphere are faster than those in Earth's. For example, the reconnection rate at Mercury is almost one order of magnitude higher that at the Earth [12]. Both MHD [29, e.g.] and hybrid [56, e. g.] approaches were used to model Mercury's interaction with Solar Wind.

The magnetic field of Mercury is much weaker (by two orders of magnitude at the surface) than that of Earth [12]. Measurements by MESSENGER (= MErcury Surface, Space, ENvironment, GEochemistry, and Ranging) probe reveal that Mercury's field is well represented by a dipole field offset from Mercury's equator by (484 ± 11) km northward. The dipole magnetic moment is tilted by less than 3° from the rotation axis of Mercury and is (195 ± 10) n$\mathrm{T}R_{\mathrm{M}}^3$, where R_M is the radius of Mercury [2].

If Mercury had a pure iron core, it would have at most a remanent magnetic field. That probably is not the case, because Mercury seems to have an internal magnetic field. Large longitudinal libration of Mercury suggests that it has a fluid outer core. If the core contains light elements as well as iron, the core can be partially molten. The candidate constituents are either sulphur, or elements present in the Earth's outer core (i.e. silicon, oxygen, etc.) [1].

If there is a molten shell inside Mercury, it can support a dynamo driven by thermal convection. If the shell is thin, this means the dynamo would yield magnetic field with significant non-dipole terms in the multipole expansion, whereas a thick shell would mean the higher-order terms of multipole expansion would be suppressed [1]. However, the dynamo mechanism is probably different from Earth's because Mercury's field is much weaker at surface than Earth's [54]. There are many dynamo models that try to explain Mercury's weak field and their review is given in [54].

Mercury also has a relatively strong inductive response. The induced field possibly contributes $\approx 10\%$ to Mercury's surface magnetic field [17]. It may be interesting to study how induced fields in Mercury affect its dynamo [1]. Besides that, remanent magnetic crustal fields are present at Mercury [1]. The magnetic field of Mercury is also greatly affected by magnetospheric currents [1], e.g. the *Chapman-Ferraro current*.

Chapter 4

Model

As a first order approximation, Moon can be considered a non-conduting obstable that absorbs all incident plasma [14, 48, 18, etc.].

The aim of this thesis is to create a geological model of the Moon and implement it into the hybrid simulation. When conductivity is taken into account, it will have an affect on $\frac{\eta}{\mu_0}\boldsymbol{\nabla}\times\mathbf{B}$ in equation (2.2).

There are two approaches to computing the magnetic field inside the Moon. One option is let macro-particles through the lunar surface, but to lower their density and omit them from the evaluation of physical quantities. This approach allows magnetic field lines to be continuous. Because charge density acts as a divisor in equation (2.2), it needs to be kept above a certain value [57]. The other option is to solve the diffusion equation for magnetic induction inside the Moon. This creates a problem: how to handle the field in lunar wake. Either particles can be re-injected behind the Moon [60] (because of field lines), or the diffusion equation can be computed in the lunar wake as well. The reasoning is that there is a plasma void in the near lunar wake. In order that the model approximates vacuum reasonably, resistivity in these regions needs to be as high as possible [20]. This approach is also used in articles [14, 10]. In magnetohydrodynamics, there is no plasma inside the planets and so the evolution of the magnetic field also reduces to diffusion equation inside the cosmic body [29, 31, 30].

The argument for using diffusion equation in hybrid model is based on the fact that resistivity is very high in regions of small density. The equation (2.2 reduces to

$$\mathbf{E} = \frac{\eta}{\mu_0}\boldsymbol{\nabla}\times\mathbf{B},$$

where η is resistivity. Assuming $\eta = \text{const.}$, we obtain the diffusion equation

$$\partial_t\mathbf{B} = \frac{\eta}{\mu_0}\nabla^2\mathbf{B}.$$

For derivation see the chapter below. The problem of this approach is a restraint for resistivity. On one hand it should be as high as possible, on the other hand, the stability condition requires η to be small so that time-step can be high. The higher the η, the smaller the time-step needs to be, which affects computational difficulty. Another option would be to keep the time-step the same and increase the spatial step. This would affect the precision of the numerical approximation of derivatives.

Another downside to this approach is that is assumes the conductivity to be homogeneous. In chapter 3, several objects have been listed that do not have homogeneous resistivity and where it is desired to take resistivity profiles in account (e.g. in the case of Galilean moons, where resistivity profile indicates the existence and location of subsurface oceans).

4.1 Boundary conditions

In the model, there are two boundaries present: a natural boundary and an artificial boundary. The natural boundary is given by the lunar surface, denoted by Γ_{LS}. The artificial boundary is introduced because the simulation domain is finite. The physical problem of solar wind flow around the Moon is unbounded and therefore boundary conditions have to be carefully imposed on the artificial boundary, in order that it is consistent with the unbounded problem.

The boundaries are shown in Fig. 4.1. The outer boundary is subdivided into Γ_{in}, Γ_{out} and Γ_{sides}, because they behave differently at least in the case of particles. Γ_{in} is a source, Γ_{out} a sink and Γ_{sides} has to be handled properly. As will later be explained, simply making it a sink is not a perfect solution.

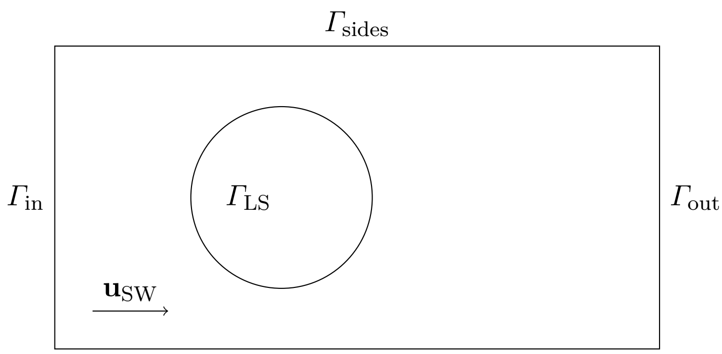

Figure 4.1: Schematic of the simulation domain (not to scale).

Three basic options come to mind with respect to particles. The boundary can either be a source or a sink of particles, or it can be periodic, that is, particles removed on one side are added on the opposite side of the simulation box. Γ_{in}, Γ_{out} are source and sink respectively. On Γ_{sides} two basic options can be used with regards to particles: sink, or periodic boundary conditions. In the former case, particles incident on Γ_{sides} are removed from the simulation and in the latter case, they are re-injected on the opposite face of the cuboid domain.

The simplest implementation, and the implementation used for the simulations presented in the following chapter, is to apply a periodic boundary condition on all sides of the simulation box. The initial condition follows the solar wind properties and the particles from behind the moon across Γ_{out} in front of it.

Implementing sink is simpler, as it means just removing particles from the simulation. However, particles are removed from the simulation that would have appeared in the domain again, as the gyrate about magnetic filed lines. This means that areas within one Larmor radius of the boundary have artificially lower density.

4.2 Layers of differing resistivity

Temporal changes in external magnetic field induce eddy currents in conductive layers of the moon. Likewise, the external magnetic field diffuses quicker into resistive layers. In the lunar case, the core is conductive and the crust is highly resistive, as was discussed in Chapter 3.

A set of six functions was written that are passed to the scheme through the library's API. The goal is to investigate how three different approaches are handled by the simulation, mostly with regards to stability.

These functions set up a resistive layer according to parameters passed through the initialization file. The three models use spherical symmetry and introduce a layer with a different resistivity. The interface between the layers is different. The models are:

1. *step function*, where there is a discontinuity where the layers with different conductivities interface,
2. *linear (by parts) function*, where the layers with differing conductivities are connected with a linear transition,
3. *tanh model*, where the layers are replaced with a hyperbolic tangent. function.

The implementation as used in the simulations is shown in subsection 4.2. It is however shown for the 2D case only for simplicity. The 3D case is completely analogous.

Step function

The 2D implementation of a step-function approach is as follows. Its 3D counterpart is analogous – only rz is added and taken into account when r2 is computed.

```
stwns_Real stwns_cam_resist_step_2d(
    STWNS_Cam cam, stwns_Real x, stwns_Real y)
{
  STWNS_CamFuncGlobals pg = cam->func->globals;
  double rx = x - pg->planet_posx;
  double ry = y - pg->planet_posy;
```

```
  double res_ampl = pg−>planet_res_ampl;
  double res_layer_thickness = pg−>planet_res_layer_thickness;
  double res_layer_pos = pg−>planet_res_layer_pos;

  double r2 = rx ∗ rx + ry ∗ ry;
  double rmin2 = (res_layer_pos − res_layer_thickness) ∗ (res_layer_pos −
       res_layer_thickness);
  double rmax2 = (res_layer_pos + res_layer_thickness) ∗ (res_layer_pos +
       res_layer_thickness);

  if (rmin2 < r2 && r2 < rmax2)
  {
    return res_ampl;
  }

  return cam−>resist;
}
```

Linear function

The linear function requires the computation of a square root and therefore it is expected to be slower than the step-function approach. Tests confirm this. Again, 3D version is quite straightforward. The parameter ramp_width is hard-coded to be equal to the thickness of the layer. Steepness could be introduced as a parameter initialized from an initialization file.

```
stwns_Real stwns_cam_resist_linear_2d(
    STWNS_Cam cam, stwns_Real x, stwns_Real y)
{
  STWNS_CamFuncGlobals pg = cam−>func−>globals;
  double rx = x − pg−>planet_posx;
  double ry = y − pg−>planet_posy;

  double res_amb = cam−>resist;

  double res_ampl = pg−>planet_res_ampl;
  double res_layer_thickness = pg−>planet_res_layer_thickness;
  double res_layer_pos = pg−>planet_res_layer_pos;

  double r = sqrt(rx ∗ rx + ry ∗ ry);
  double rmin = res_layer_pos − res_layer_thickness;
  double rmax = res_layer_pos + res_layer_thickness;

  double ramp_width = pg−>planet_res_layer_thickness;
```

```
  double ramp_start = res_layer_pos − res_layer_thickness − ramp_width;
  double ramp_end = res_layer_pos + res_layer_thickness + ramp_width;

  if (ramp_start < r && r < rmin)
  {
    return (res_ampl − res_amb) / (rmin − ramp_start) ∗ (
    r − ramp_start) + res_amb;
  }
  if (rmin < r && r < rmax)
  {
    return res_ampl;
  }
  if (rmax < r && r < ramp_end)
  {
    return (res_ampl − res_amb) / (rmin − ramp_start) ∗ (
    rmax − r) + res_ampl;
  }
  return res_amb;
}
```

Tanh model

The hyperbolic tangent model does not require the computation of square roots and therefore is faster than the linear model, as confirmed by tests.

```
double tgh_profile(STWNS_Cam cam, double r)
{
  STWNS_CamFuncGlobals pg = cam−>func−>globals;

  double res_amb = cam−>resist;
  double res_ampl = pg−>planet_res_ampl;
  double res_layer_thickness = pg−>planet_res_layer_thickness;
  double res_layer_pos = pg−>planet_res_layer_pos;
  double ramp_width = res_layer_thickness;
  /∗ could be set via another parameter ∗/

  double res = res_amb + (res_ampl − res_amb) ∗ 0.5 ∗
    (tanh((4 ∗ (r − res_layer_pos) + 2 ∗ res_layer_thickness) / ramp_width
         + 2)
    − tanh((4 ∗ (r − res_layer_pos) − 2 ∗ res_layer_thickness) /
         ramp_width − 2));

  return res;
}

stwns_Real stwns_cam_resist_tgh_2d(
```

```
    STWNS_Cam cam, stwns_Real x, stwns_Real y)
{
  STWNS_CamFuncGlobals pg = cam->func->globals;
  double rx = x - pg->planet_posx;
  double ry = y - pg->planet_posy;

  double r = sqrt(rx * rx + ry * ry);

  return tgh_profile(cam, r);
}
```

Chapter 5

Results

5.1 Resistivity model

Three approaches have been used to model Moon's resistivity profile. All of them assume spherical symmetry. The models are:

1. step function,
2. linear (by parts) function,
3. hyperbolic tangent model.

The simulations were done in a 2D case only in order that multiple parameters may be investigated. 3D simulations would have been too computationally expensive to compare 7 different cases. A resistive layer was introduced – for further explanation, see Chapter 4. The implementation as used in the simulations is shown in subsection 4.2. It is however shown for the 2D case only for simplicity. The 3D case is analogous. The resistive layer is put either in 0.8 to represent a highly resistive crust, or in 0.2 to represent a conductive core. The simulation runs are summarized in the following table:

#	RL position $[R_L]$	RL thickness $[R_L]$	resistivity	notes
1	0.8	0.2	0.1	default
2	0.8	0.2	1	
3	0.8	0.2	10	
4	0.8	0.2	100	crashes
5	0.2	0.2	0.01	
6	0.2	0.2	0.001	
7	0.2	0.2	0.0001	

All the test were done with magnetic field $\mathbf{B} = (1/\sqrt{2}, -1/\sqrt{2}, 0)$, $dt = 0.01$, $n_x, n_y = 1000, 200$. Tanh turned out to be even faster than linear in tests. The linear model was slowest – probably due to the computation of square roots.

Graphs of differences between configurations were generated. Below is a selection of them. The difference in wake field is the most significant in the case of a highly resistive layer. The noise in the lunar wake is likely due to the random removal of incident particles.

Parameter	Value
IMF orientation	$(\sqrt{2}/2, -\sqrt{2}/2, 0)$
Bulk velocity of ions	$(5, 0, 0)v_A$
Simulation box size	1000×200
Cell size	0.4Λ
Time step	0.01Λ

Table 5.1: Simulation parameters for the investigation of various resistivity models

5.1.1 Step function

There are no significant differences between the configurations when it come to ion charge density – see Fig. 5.1.

As the solar wind passes around the Moon, a plasma void is left in the lunar wake. This cavity is filled from both sides, until it is refilled at about $x = 5R_\mathrm{L}$. The perturbations in the lunar wake are confined by a Mach cone with the apex angle of about 14°. Near the surface of the Mach cone, the ion charge density is less than ρ_SW. From $x = 5R_\mathrm{L}$, a recompression cone emerges with approximately equal apex angle to the Mach cone. In this region, the ion charge density rapidly increases. For $y < 0$, it is greater than ρ_SW – this are can be seen in all graphs stretching from $x = 5R_\mathrm{L}, y = -1R_\mathrm{L}$ to $x = 13R_\mathrm{L}$.

The most notable difference is between configurations 3 and 1 – see Fig. 5.2. The magnetic field is mostly affected inside the lunar crust, as expected. The perturbation in magnetic field of crustal origin propagates alongside Mach cone. However, these perturbations are comparable to the random noise and therefore cannot be viewed as significant.

The difference between configurations 7 and 1 is in Fig. 5.3. There, only the noise in lunar wake is noticeable and there are no significant differences between the two cases.

5.1.2 Linear function

The most notable difference is between configurations 3 and 1 – see Fig. 5.4. In the case of the linear model, this difference is much more significant, especially for magnetic field B_x and B_z, where the perturbations propagate alongside both sides of the Mach cone.

The difference between configurations 7 and 1 is not significant.

5.1.3 Hpyerbolic tangent model

The most notable difference is between configurations 3 and 1 – see Fig. 5.4. In the case of the hyperbolic tangent model, this difference is comparable to that of step function model. The magnetic field is mostly affected inside the lunar crust, as expected. The perturbation in magnetic field of crustal

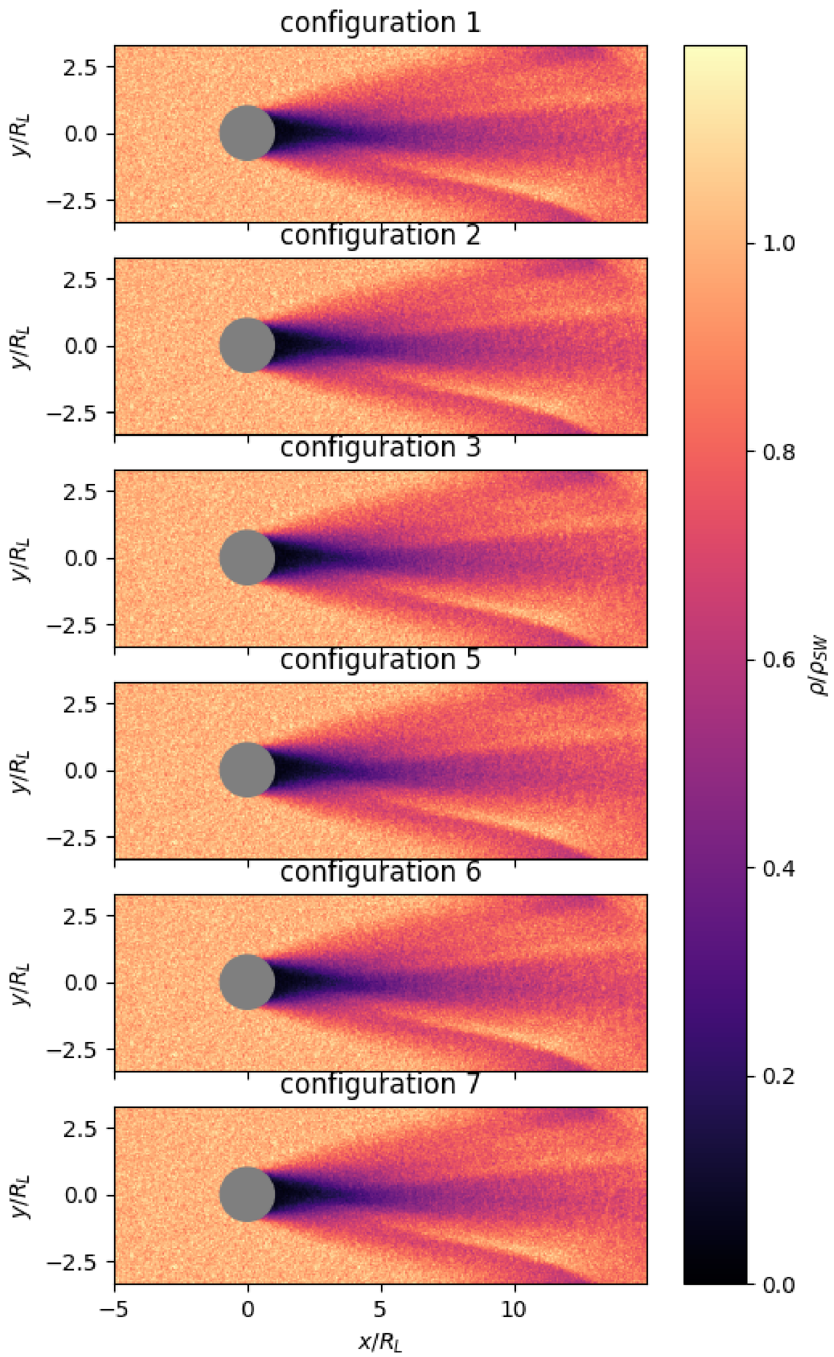

Figure 5.1: Plot of ion charge densities for various parameter configurations, n, $\Omega t = 40$. Configuration 1 serves as a control. Configurations 2 and 3 contain a crustal layer of enhanced resistivity. Configurations 5, 6 and 7 contain a layer of decreased resistivity represnting a conducting core.

origin propagates alongside Mach cone. The perturbation are small compared to the noise in lunar wake. There are no significant differences between configurations 7 and 1 apart from noise in the lunar wake.

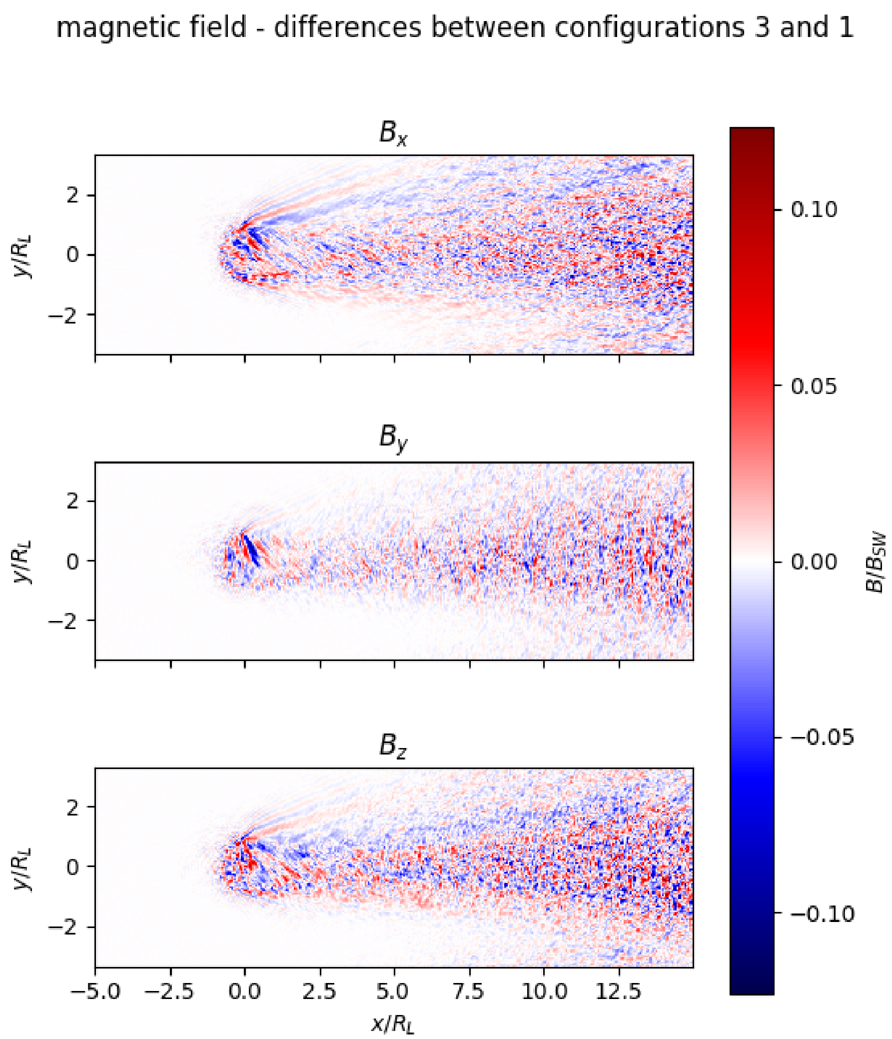

Figure 5.2: Plot of the magnitude of differences in magnetic field in configurations 3 (highly resistive crust) and 1 (control) for the step function model; $\Omega t = 40$.

The differences in perturbations near the boundary of Mach cone seem most profound in the case of a the linear function and least with the hyperbolic tangent model. The smoother the transition is, the smaller the influence – the question remains what is the desired behaviour for the model to be realistic.

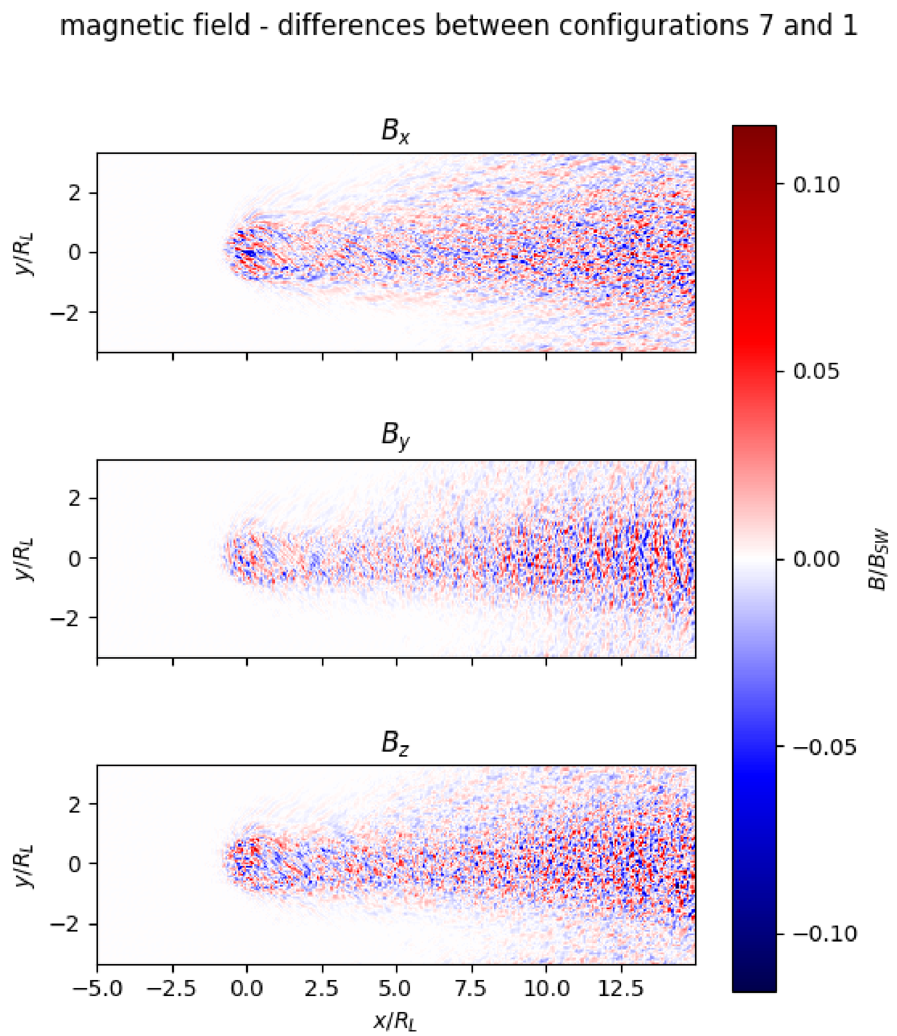

Figure 5.3: Plot of the magnitude of differences in magnetic field in configurations 7 (conducting core) and 1 (control) for the step function model; $\Omega t = 40$.

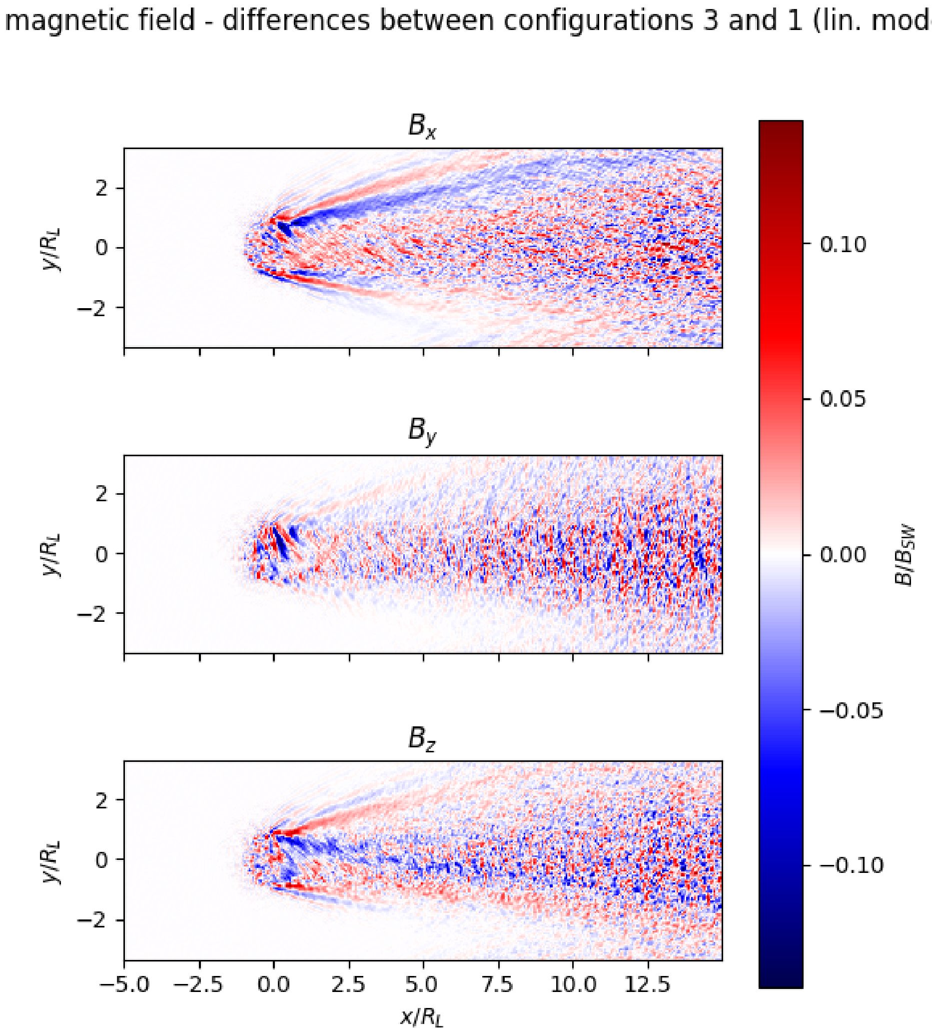

Figure 5.4: Plot of the magnitude of differences in magnetic field in configurations 3 (highly resistive crust) and 1 (control) for the linear function model; $\Omega t = 40$.

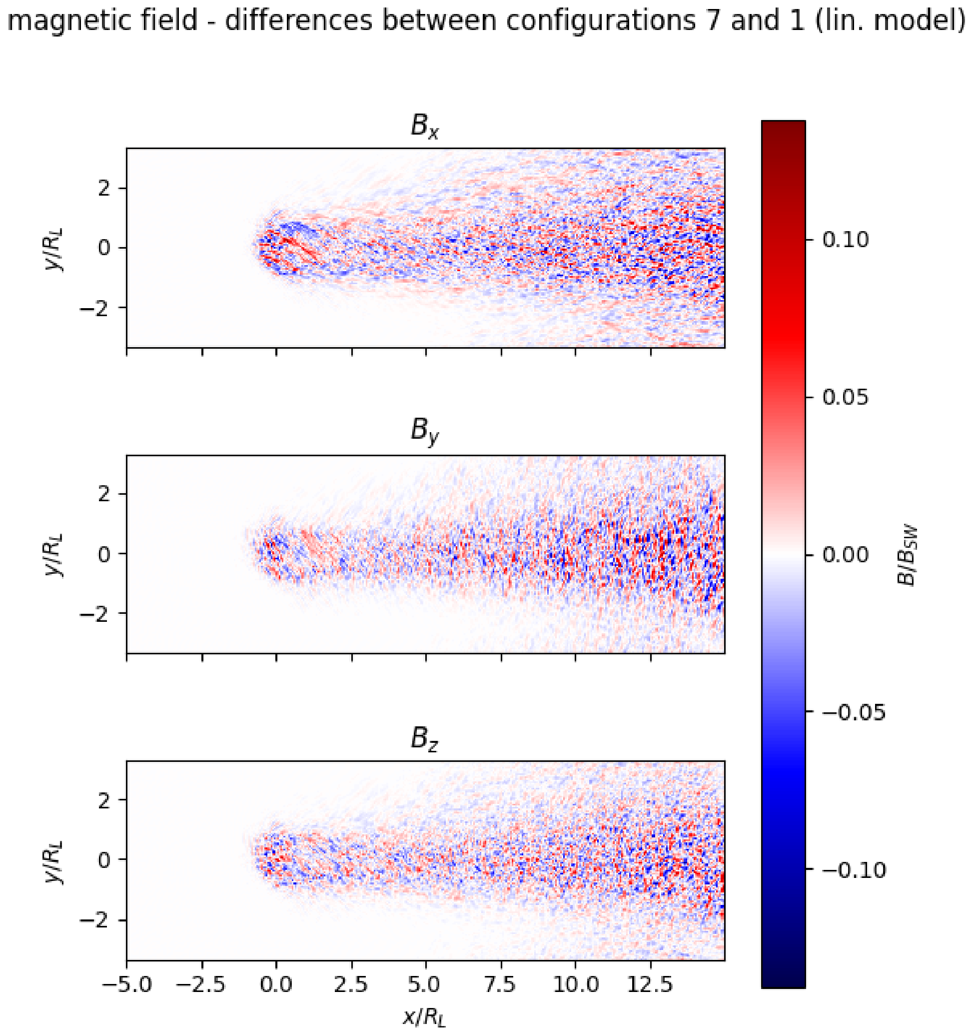

Figure 5.5: Plot of the magnitude of differences in magnetic field in configurations 7 (conducting core) and 1 (control) for the linear function model; $\Omega t = 40$.

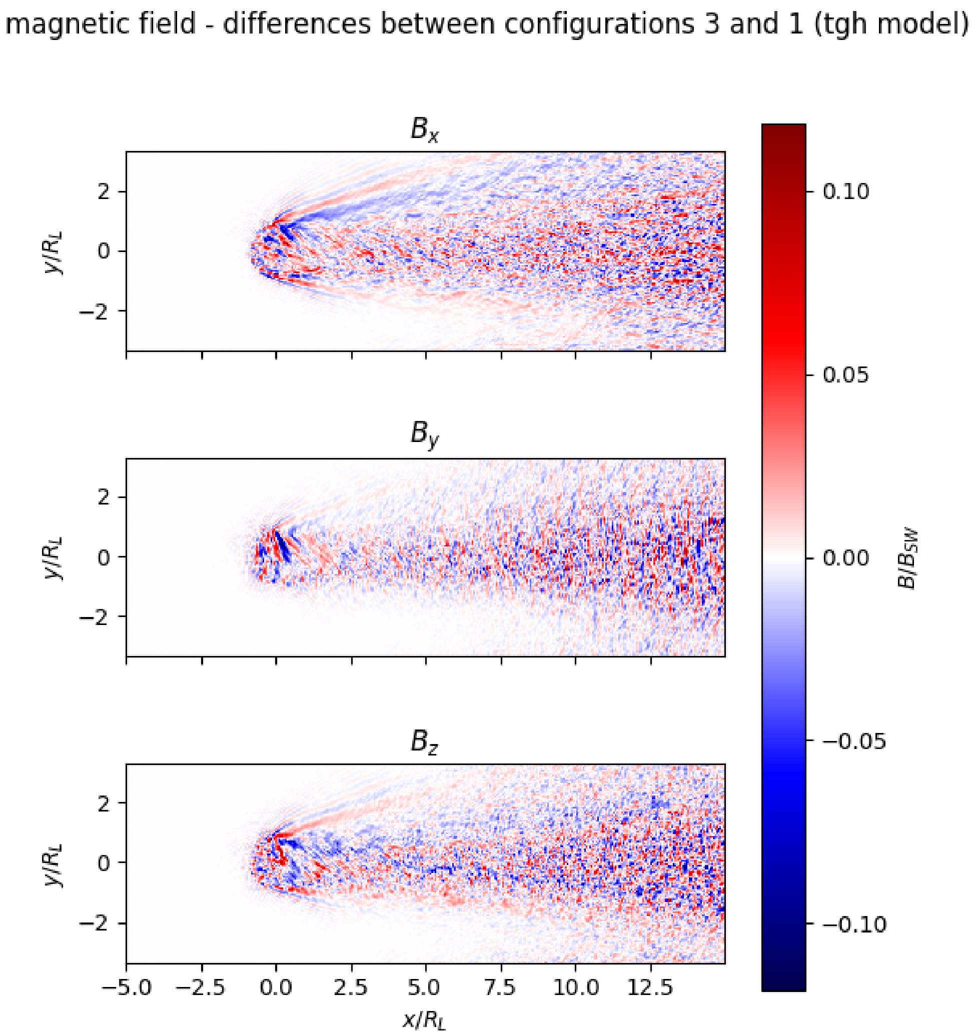

Figure 5.6: Plot of the magnitude of differences in magnetic field in configurations 3 (highly resistive crust) and 1 (control) for the hyperbolic tangent model; $\Omega t = 40$.

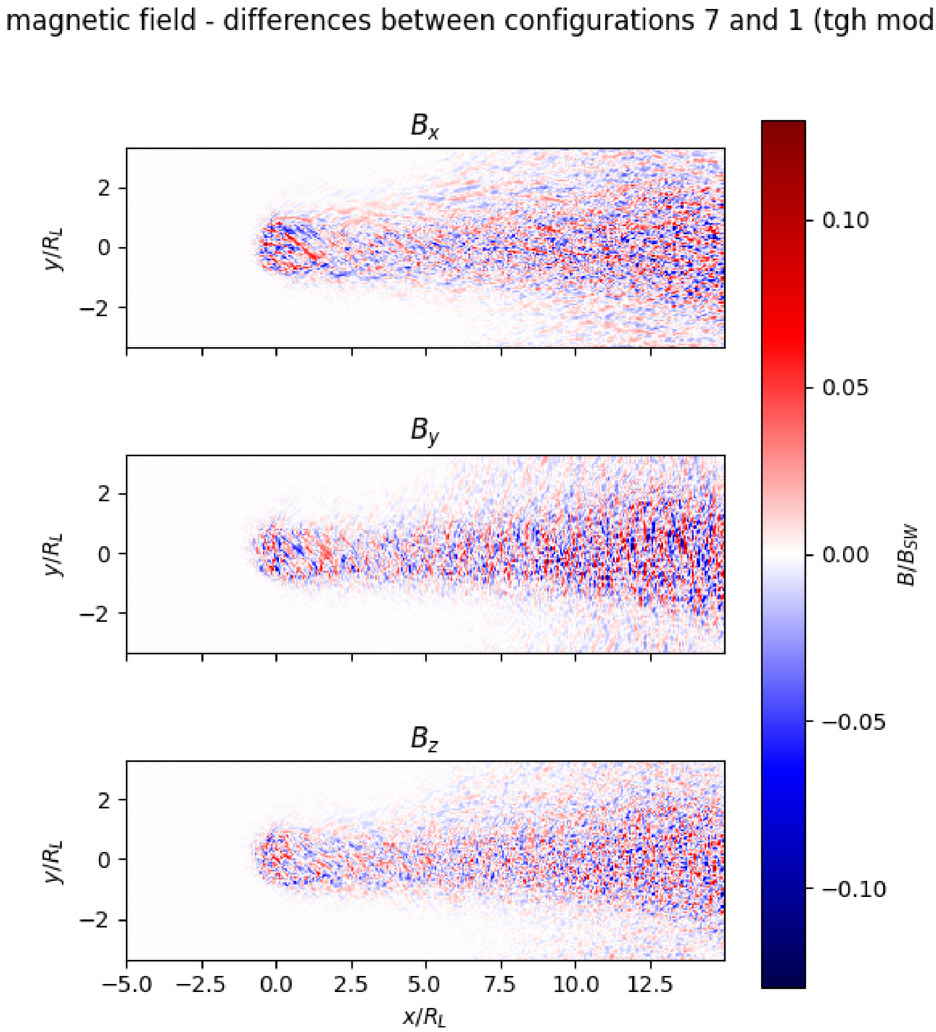

Figure 5.7: Plot of the magnitude of differences in magnetic field in configurations 7 (conducting core) and 1 (control) for the hyperbolic tangent model; $\Omega t = 40$.

5.2 Two species plasma interaction with Moon

A simulation with two species is analysed to see how the model is affected by adding another ion specie, i.e. apart from H+ ions to have a specie of He++ ions. The parameters of the simulation are summarized in Table 5.2.

Parameter	Value
IMF orientation	$(\sqrt{2}/2, -\sqrt{2}/2, 0)$
Bulk velocity of hydrogen ions	$(5, 0, 0)v_A$
Bulk velocity of helium ions	$(5.212, -0.212, 0)v_A$
Simulation box size	$500 \times 400 \times 304$
Cell size	$0.4\Omega^{-1}$

Table 5.2: Simulation parameters of the two specie simulation

Figure 5.8 shows graphs of the charge density of the first specie (H+) in the xy plane at $z = 0$ and the xz plane at $y = 0$, respectively. Figure 5.9 shows four yz planar sections for varying x that is shown in the titles of the subfigures. Graphs of the charge density of the second specie (He++) are in Figures 5.10 and 5.11.

The H+ ion specie charge density looks generally similar to the ion charge density in the case of simulation of only one specie solar wind interaction with the Moon. A plasma cavity is formed in the lunar wake, which is refilled primarily along magnetic field lines. The rarefaction cone has the apex angle approximately equal to 14°. Further down the wake, there is a compression region surrounding the central plasma cavity. There is a notable asymmetry – the proton charge density is enhanced in an area that can be seen at approximately $x = 5R_L, y = -2R_L, z = 0$. This could be due to the introduction of the He++ species, but is likely due to the asymmetry introduced by the magnetic field. As the ions move along field lines, the compression region is filled quicker on that side of the lunar wake. While x-axis is defined by the movement of H+, He++ cavity is oriented with a non-zero angle (stretching toward $-y$). The movement of He++ ions is slower due to their higher mass-to-charge ratio. The angle formed by the ion bulk velocity vector and the magnetic field lines is smaller in the case of bulk velocity of helium ions, which means they will not refill the cavity as quick as hydrogen ions, as ions move along field lines. This suggests that the cavity formed by helium ions is refilled by hydrogen ions, as is evidenced by the y component of the bulk velocity of hydrogen ions.

The ratio of the charge densities of ions (He++/H+) is shown in Figures 5.12 and 5.13. The ratio is rather high in the plasma cavity due to the different directions of the bulk velocities of H+ and He++ ions in the solar wind, respectively. The cavity in He++ ions is not aligned along the x axis whereas the cavity in H+ ions is and therefore the ratio of He++/H+ ion charge density is very high along the x axis, corresponding with the cavity

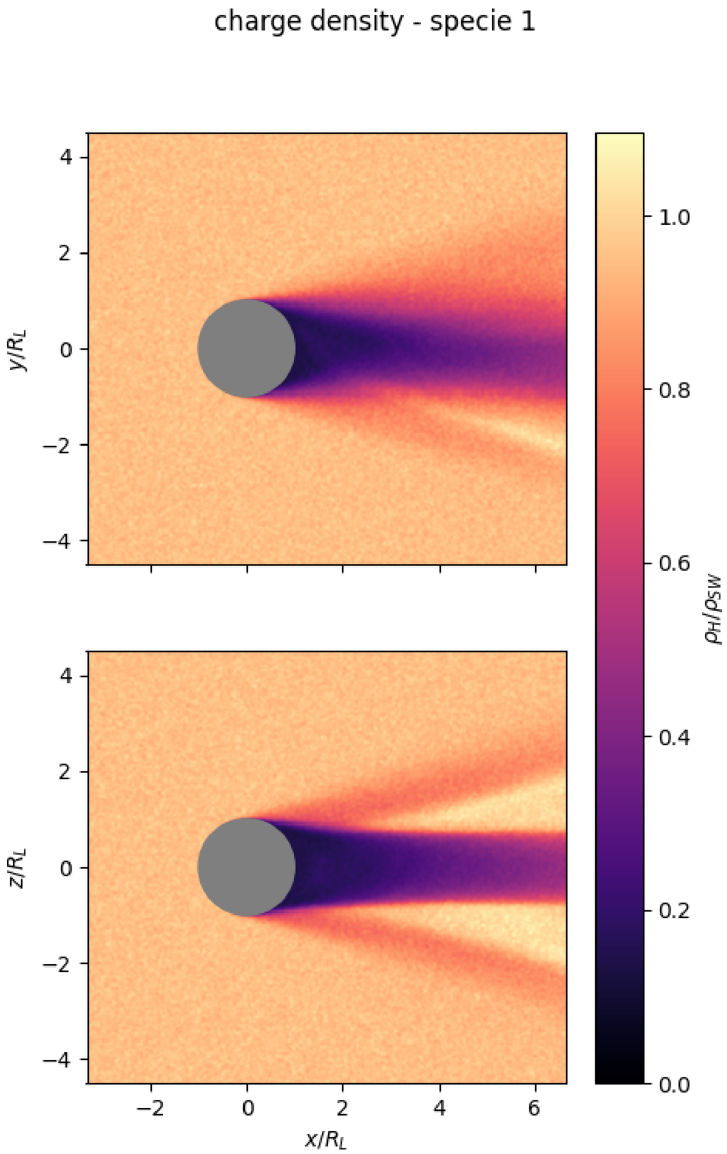

Figure 5.8: Charge density of H+ ions: top – xy plane at $z = 0$, bottom xz plane at $y = 0$

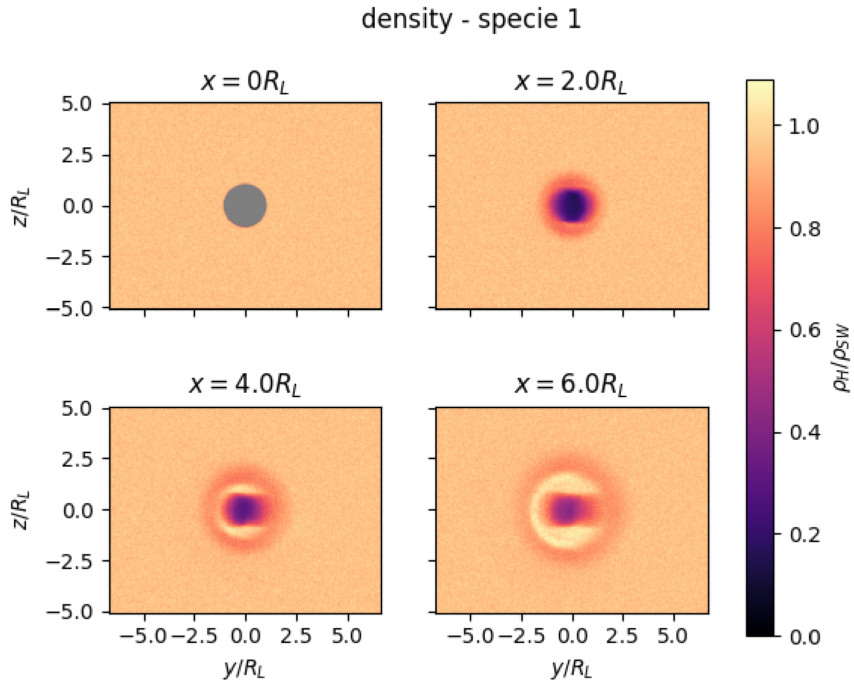

Figure 5.9: Charge density of H+ ions: transversal sections at $x = 0, x = 2R_L, x = 4R_L, 6 = R_L$

in H+ ions. In the graphs of the ratio of charge density of He++ and H+ ions, the rarefaction region and compression region of H+ ions is apparent – the lighter cone (higher relative density of He++) is the rarefaction region and the darker cone (higher relative density of H+) is the compression region. In the graphs in Fig. 5.13, these regions appear as annuli. There are no significant features due to He++ ions.

The bulk velocity of the two ion species is shown in Figures 5.14, 5.15, 5.16 (H+ specie, longitudinal sections), 5.20, 5.21, 5.22 (He++ specie, longitudinal sections), 5.17, 5.18, 5.19 (H+ specie, transversal sections), 5.23, 5.24, 5.25 (He++ specie, transversal sections). The bulk velocity is directed to the centre as ions refill the lunar cavity by H+ ions – this can be seen in Figures 5.24 and 5.25. The refilling is confined within the Mach cone. At $x = 0.6R_{\mathrm{L}}$, the central region is surrounded by an annulus where the y-component of bulk velocity is approximately zero. This area corresponds to the compression cone – see Fig. 5.9. Outside this annulus, the y component of hydrogen ion bulk velocity is greater than zero for y less than zero and vice versa; the same holds for the z component of hydrogen ion bulk velocity – this shows that hydrogen ions are transported from the rarefaction cone toward the compression region. The graph y-component of hydrogen bulk velocity in the near wake shows that ions refill the wake predominantly from the side of $y > 0$. In the graph of xy plane, the field is less than zero on the x axis in the near wake from R_{L} to approximately $2R_{\mathrm{L}}$ – see graphs on Figs. 5.15,

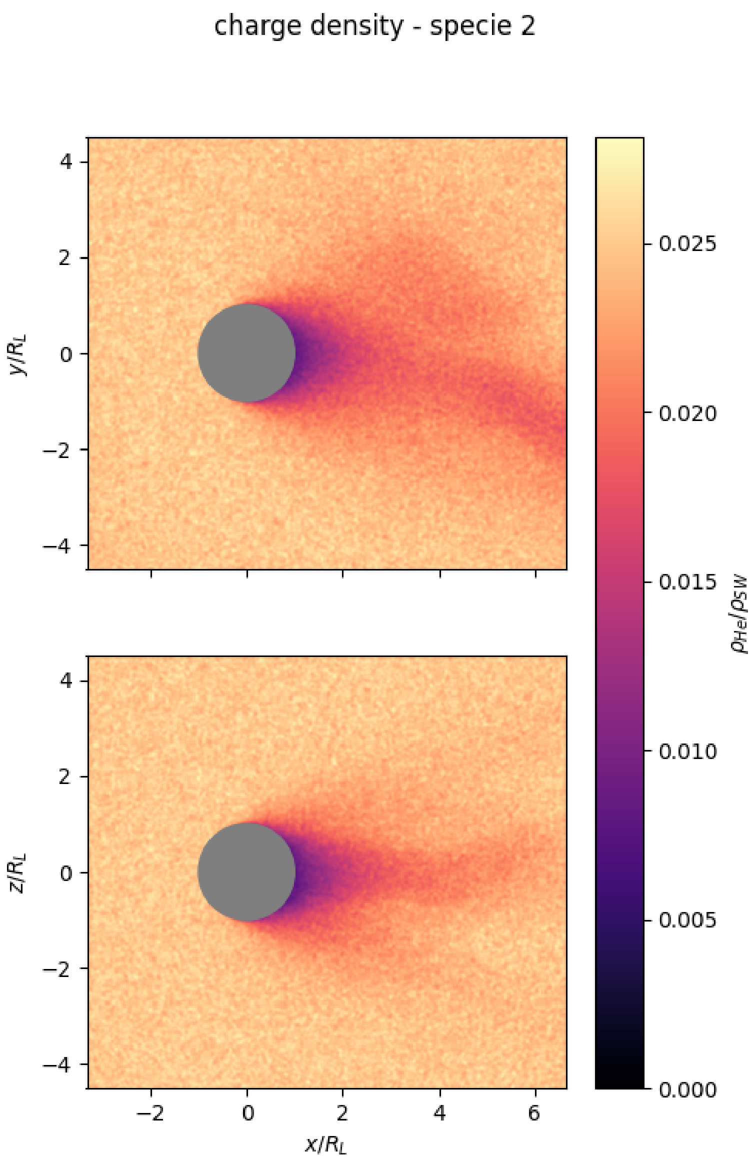

Figure 5.10: Charge density of He++ ions: top − xy plane at $z = 0$, bottom xz plane at $y = 0$

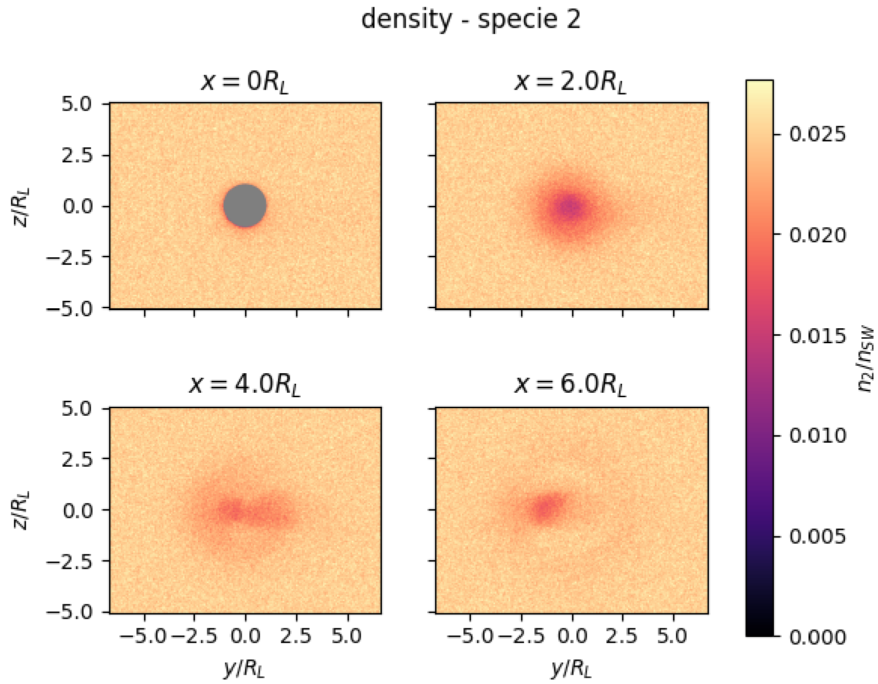

Figure 5.11: Charge density of He++ ions: transversal sections at $x = 0, x = 2R_L, x = 4R_L, 6 = R_L$

5.18. This is likely due to the ions moving along magnetic field lines across the mach cone and rarefaction region. The hydrogen ions thus refill also the plasma cavity formed by He++ ions, which the slow He++ ions do not refill to this extent – see that the graph 5.21 does not contain this feature. The y-component of bulk velocity of He++ ions is approximately zero on the x axis – the bulk velocity of He++ ions does not show the aforementioned asymmetry.

The graphs of temperature anisotropy are shown in Figures 5.26, 5.27, 5.28 and 5.29. H+ ions have a high perpendicular temperature within the Mach cone in areas surrounding the plasma cavity that stretch in the y-direction as can be seen in Figure 5.26 and 5.27. The H+ ions within the rarefaction cone have low $T_\perp/T_\parallel$. He++ ions' $T_\perp/T_\parallel$ ratio is enhanced in an area that stretches in the direction of approximately $\sim 9°$ with respect to x axis, which is a larger angle than the direction of the bulk velocity of He++ ions in the solar wind.

Figures 5.30, 5.31, 5.32 show the graphs of the x, y and z component of magnetic field, respectively, where the top subfigures shows the xy plane at $z = 0$ and the bottom subfigures show the xz plane at $y = 0$. Figures 5.33, 5.34, 5.35 show the x, y and z component of magnetic field, respectively, at yz plane at various x (shown in the subtitles). Magnetic field lines are plotted in Figures 5.36 and 5.37. The magnetic field wake structure does not differ significantly from that of a single specie model. The x and y components of

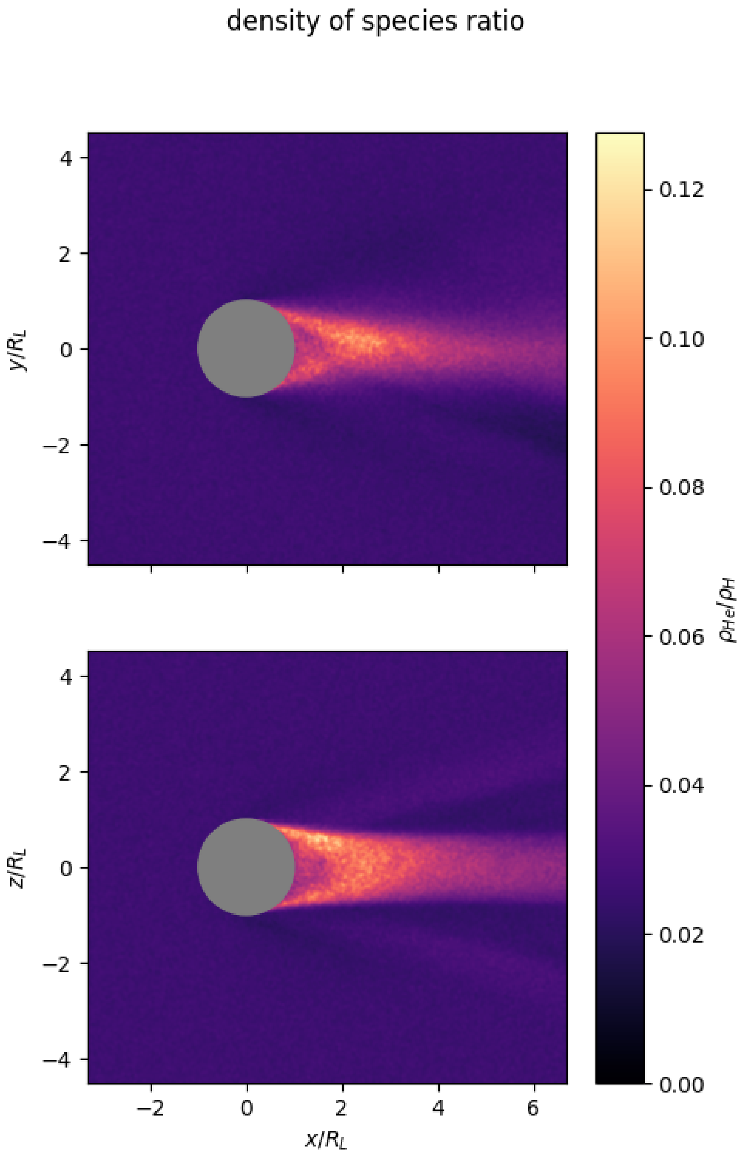

Figure 5.12: Ratio of ion specie densities: top – xy plane at $z = 0$, bottom xz plane at $y = 0$

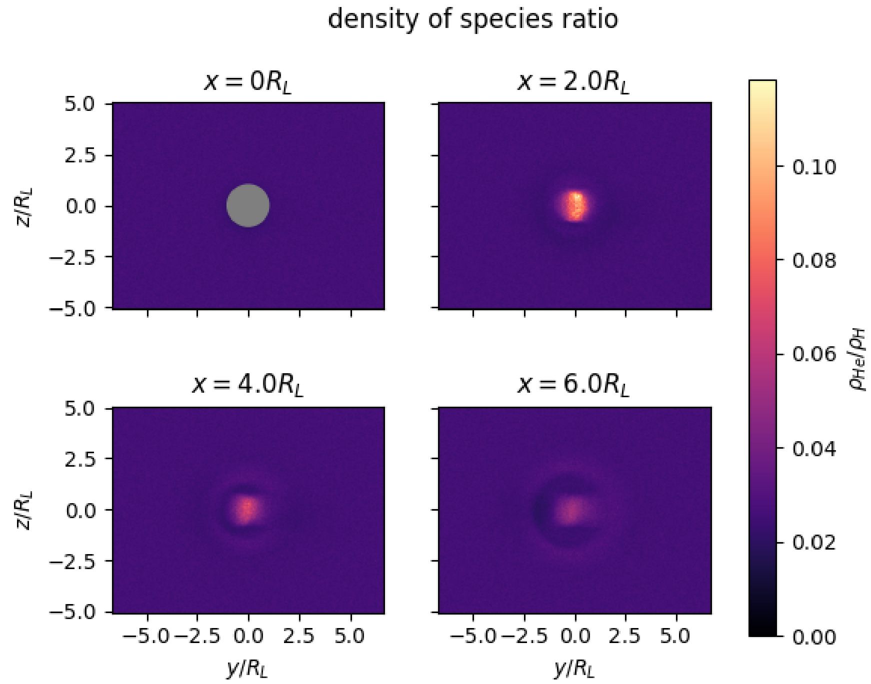

Figure 5.13: Ratio of ion specie densities: transversal sections at $x = 0, x = 2R_L, x = 4R_L, 6 = R_L$

the magnetic field are enhanced in the central part of the lunar wake. The x component is weakened in the entire rarefaction region. The y component of the magnetic field has similar features – it is enhanced in the centre of the wake and weakened in the rarefaction region. However, this weakening is mostly prevalent in the z direction – see Fig. 5.34. The enhancement of the magnetic field in the central wake is also apparent in the graph of magnetic field lines (Fig. 5.37), where the field lines are compressed in the central part of the wake.

Figures 5.38, 5.39 and 5.40 show components of electrical current in xy (top) and xz (bottom), respectively. Transversal sections at $x = 0, 2R_L, 4R_L$ and $6R_L$ respectively are shown in figures 5.41, 5.42 and 5.43. The stream plots are in Figures 5.44 and 5.45. The electrical current perpendicular to the wake is counter-clockwise around the plasma cavity. The y component of the magnetic field is prevalent along the surface of the central plasma cavity. The electrical currents are closed at the end of the wake structure – these areas of the lunar wake structure for high x are however not relevant because they are a product of the initial conditions of the numerical simulation.

The graphs of electric field are in Figures 5.46, 5.47, 5.48, 5.49, 5.50 and 5.51. The electric field is not significantly different from a single-specie case. The x component of the electric field greater than zero in the lunar wake for $z > 0$ and lower than zero for $z < 0$. The y component of the electric field in the lunar wake is divided into four quadrants stretching alongside x axis –

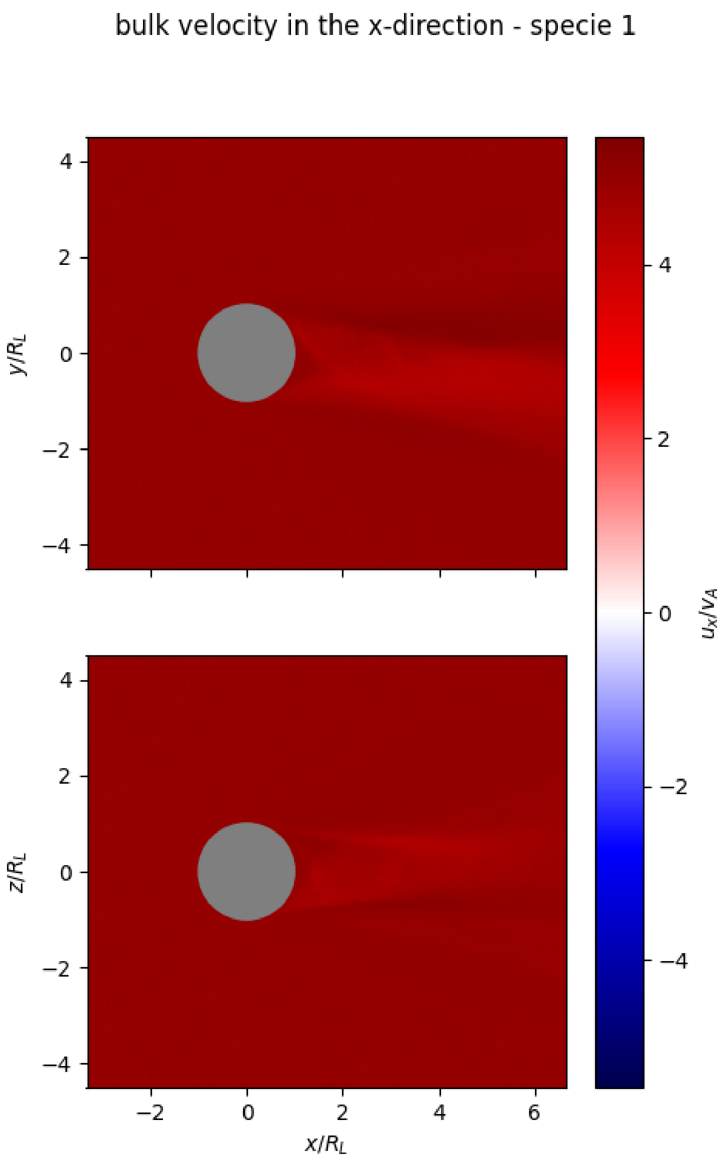

Figure 5.14: Bulk velocity in x-direction of H+ ions: top $-$ xy plane at $z = 0$, bottom xz plane at $y = 0$

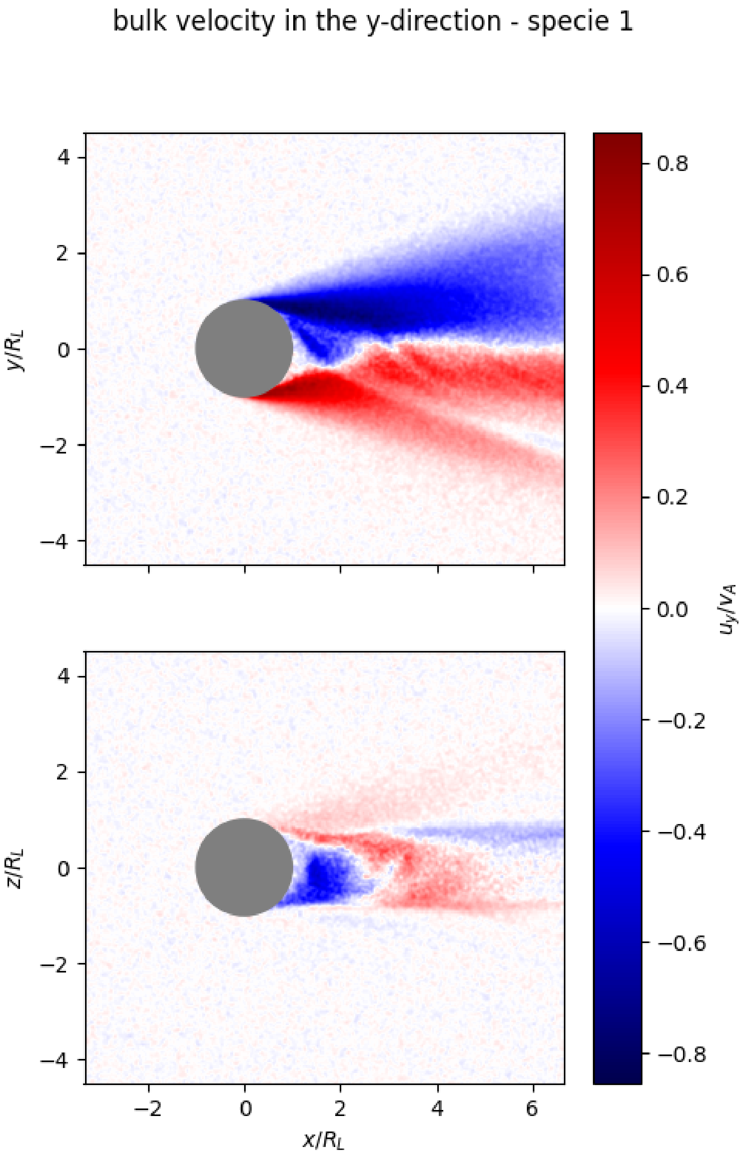

Figure 5.15: Bulk velocity in y-direction of H+ ions: top – xy plane at $z = 0$, bottom xz plane at $y = 0$

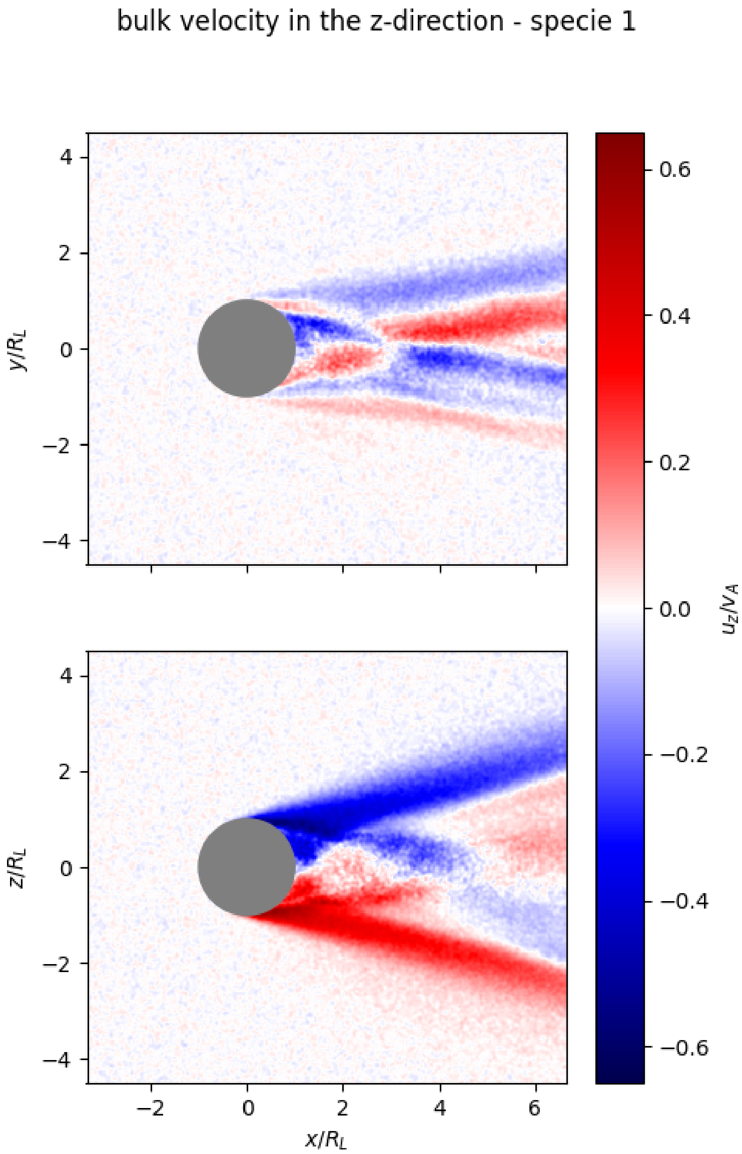

Figure 5.16: Bulk velocity in z-direction of H+ ions: top – xy plane at $z = 0$, bottom xz plane at $y = 0$

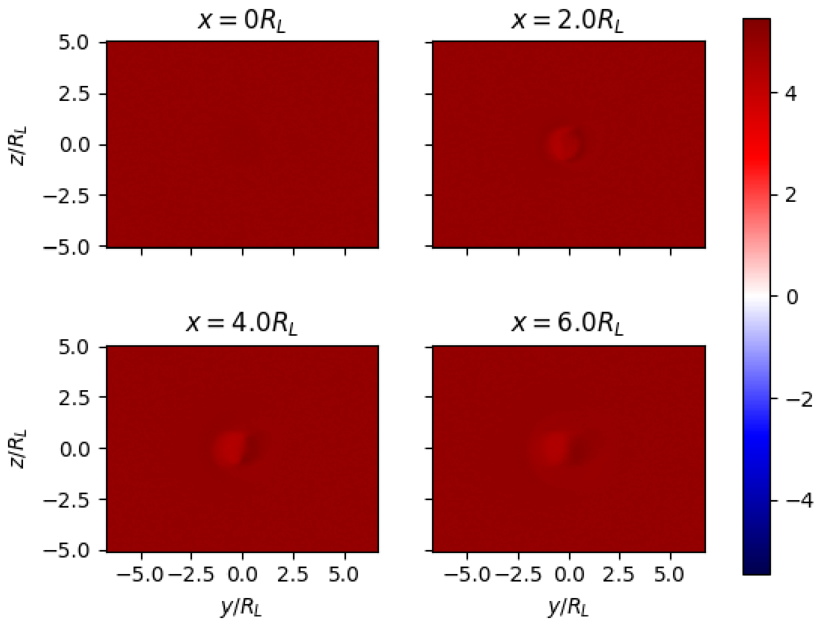

Figure 5.17: Bulk velocity in x-direction of H+ ions: transversal sections at $x = 0, x = 2R_L, x = 4R_L, 6 = R_L$

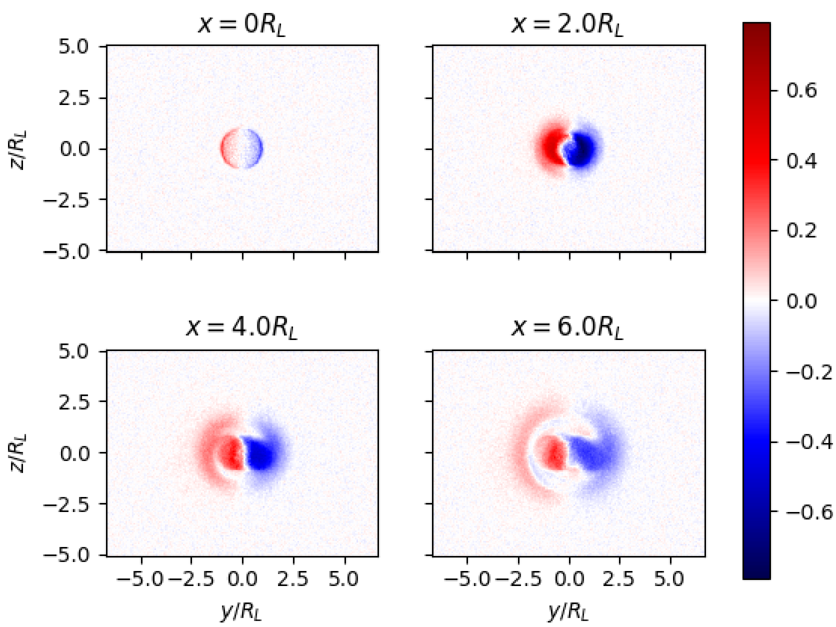

Figure 5.18: Bulk velocity in y-direction of H+ ions: transversal sections at $x = 0, x = 2R_L, x = 4R_L, 6 = R_L$

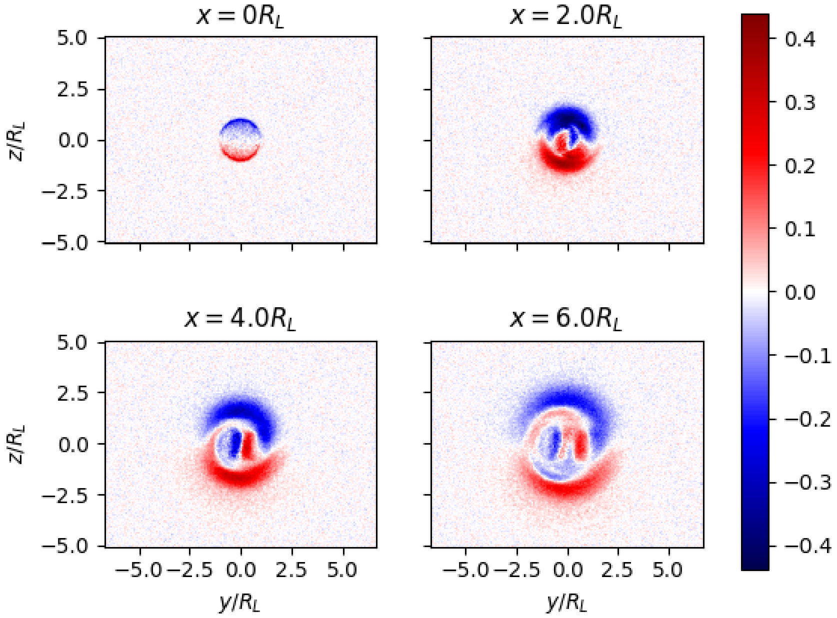

Figure 5.19: Bulk velocity in z-direction of H+ ions: transversal sections at $x = 0, x = 2R_L, x = 4R_L, 6 = R_L$

see 5.49.

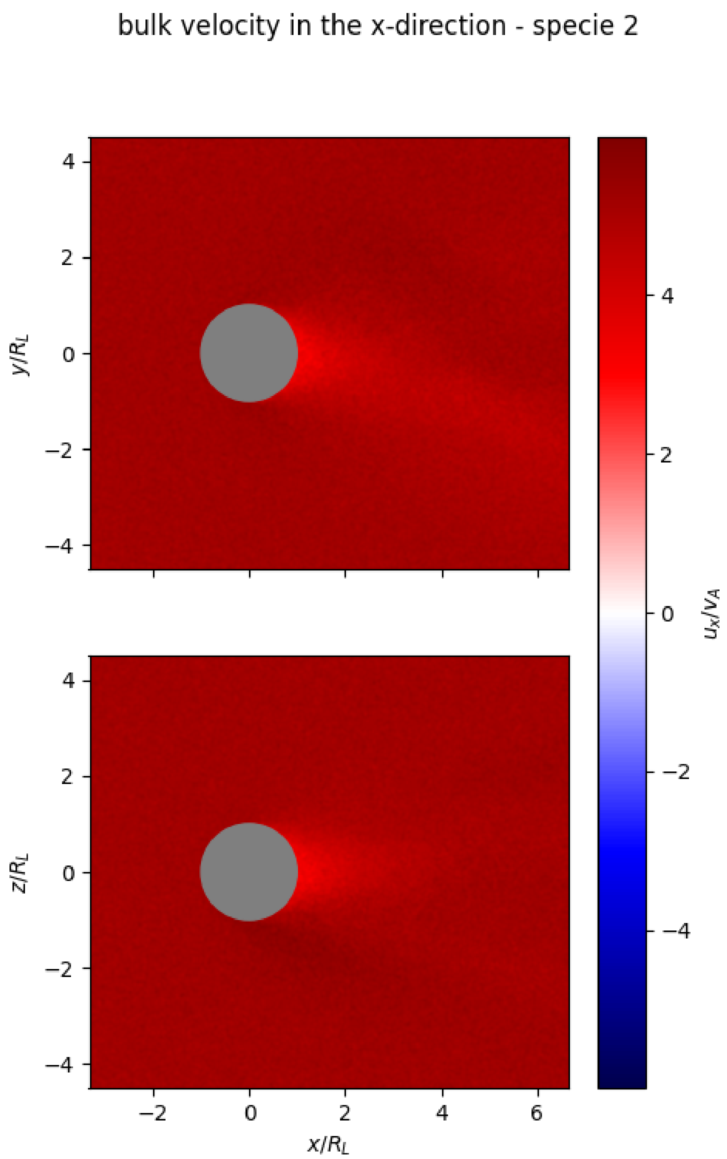

Figure 5.20: Bulk velocity in x-direction of He++ ions: top – xy plane at $z = 0$, bottom xz plane at $y = 0$

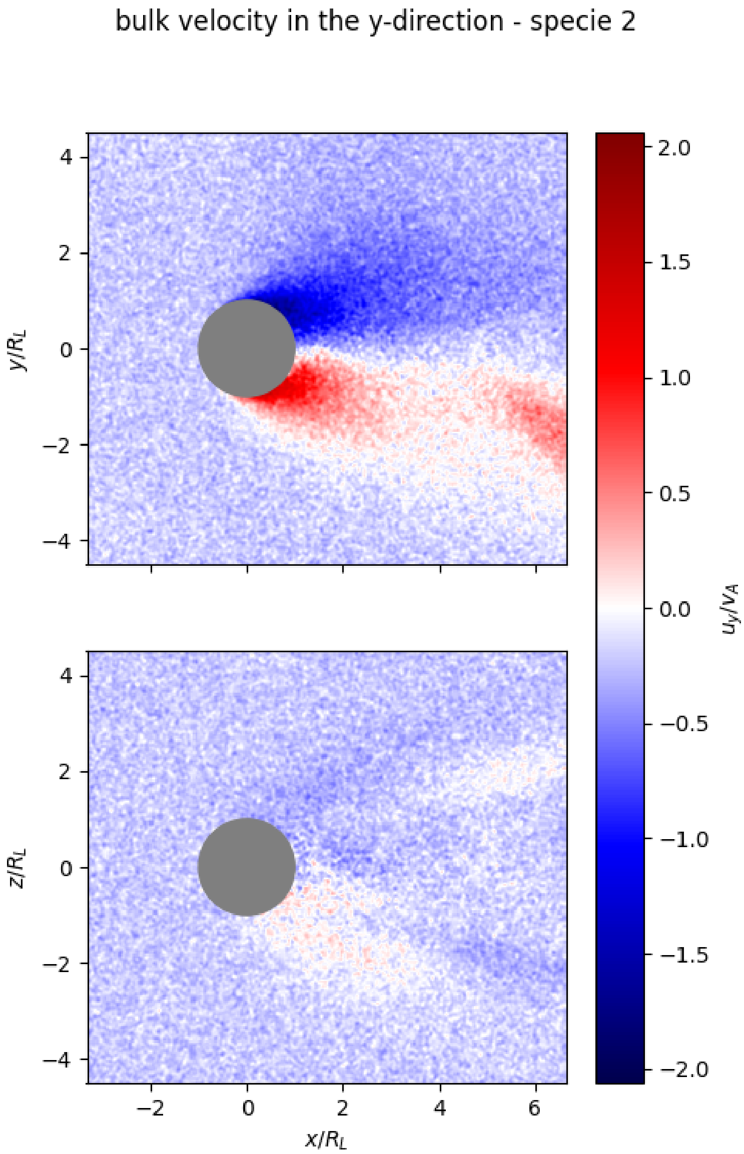

Figure 5.21: Bulk velocity in y-direction of He++ ions: top – xy plane at $z = 0$, bottom xz plane at $y = 0$

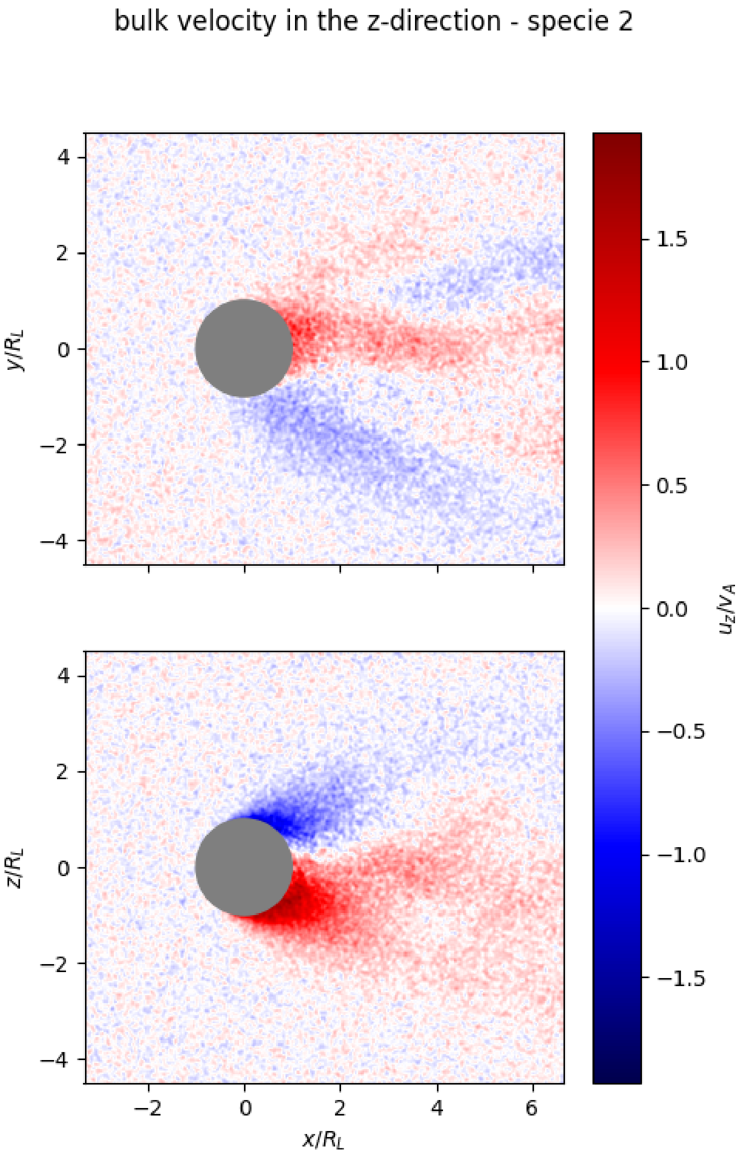

Figure 5.22: Bulk velocity in z-direction of He++ ions: top – xy plane at $z = 0$, bottom xz plane at $y = 0$

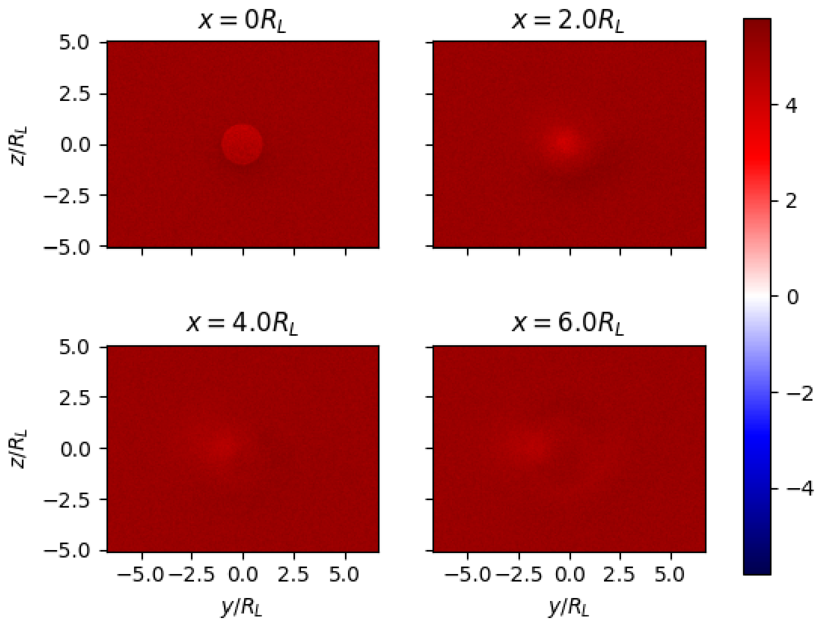

Figure 5.23: Bulk velocity in x-direction of He++ ions: transversal sections at $x = 0, x = 2R_L, x = 4R_L, 6 = R_L$

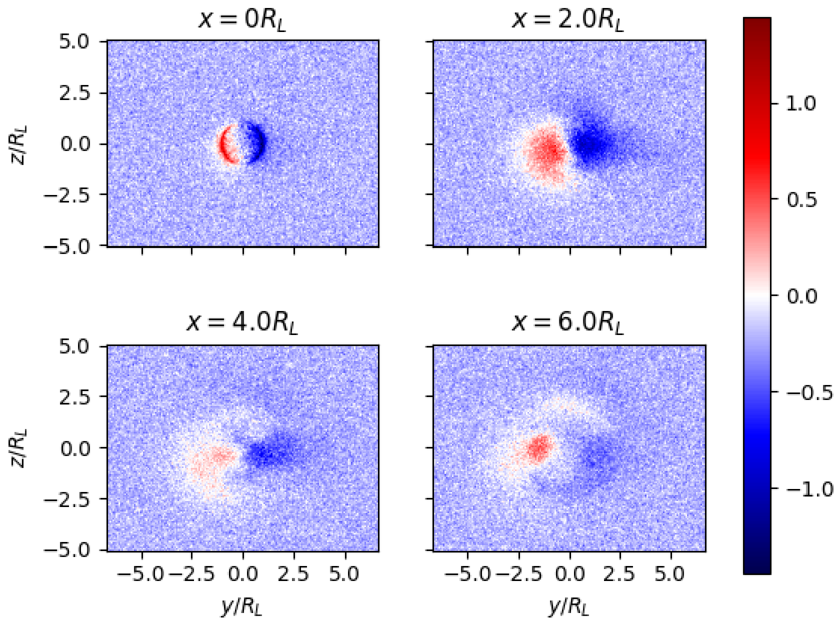

Figure 5.24: Bulk velocity in y-direction of He++ ions: transversal sections at $x = 0, x = 2R_L, x = 4R_L, 6 = R_L$

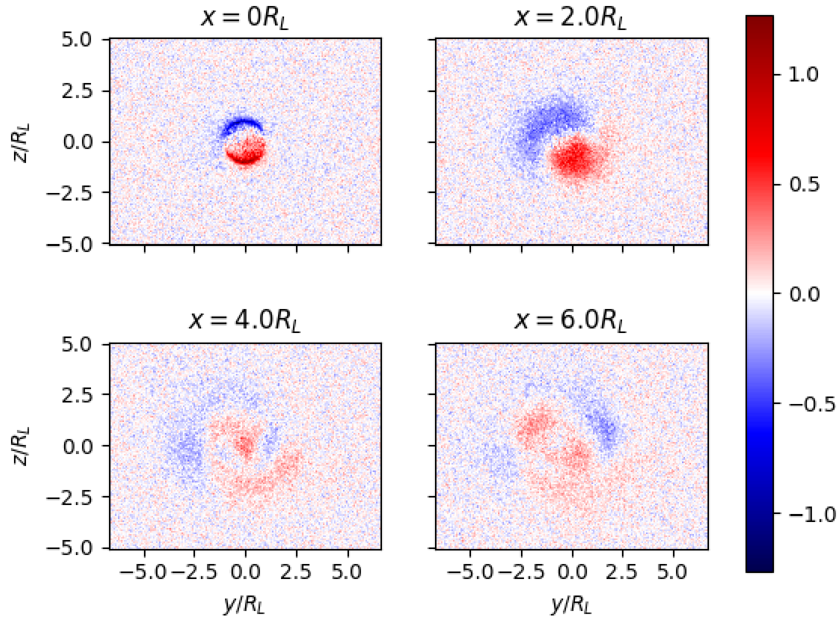

Figure 5.25: Bulk velocity in z-direction of He++ ions: transversal sections at $x = 0, x = 2R_L, x = 4R_L, 6 = R_L$

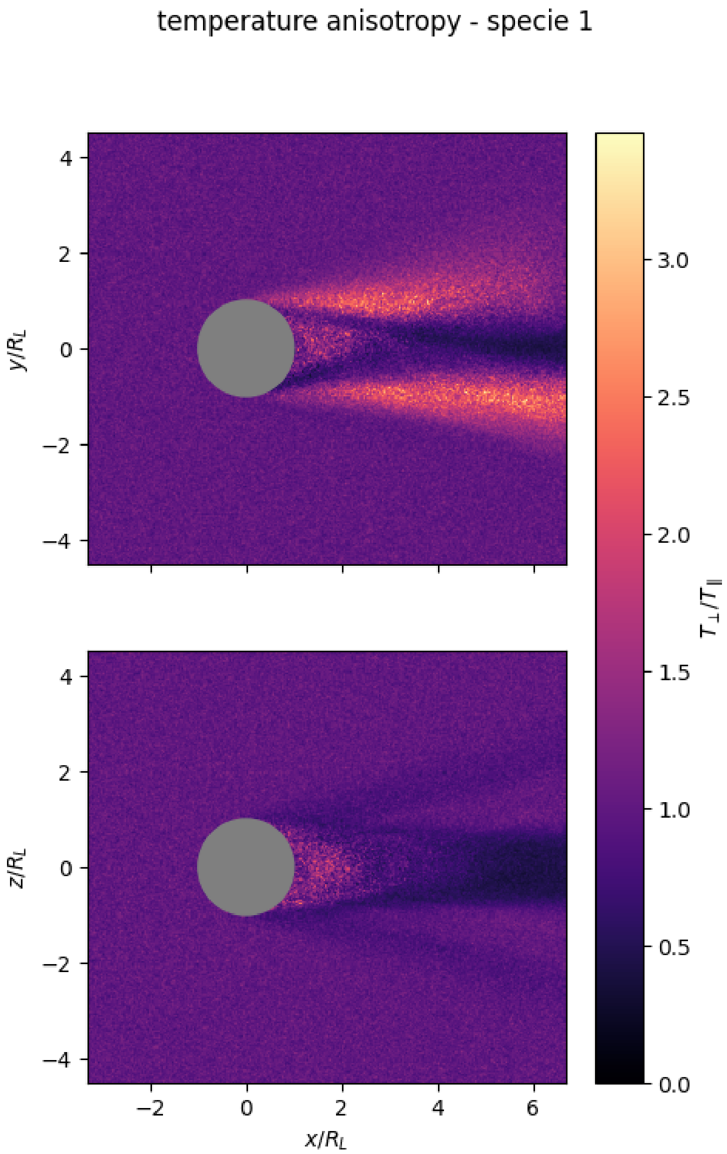

Figure 5.26: Temperature anisotropy of H+ ions: top − xy plane at $z = 0$, bottom xz plane at $y = 0$

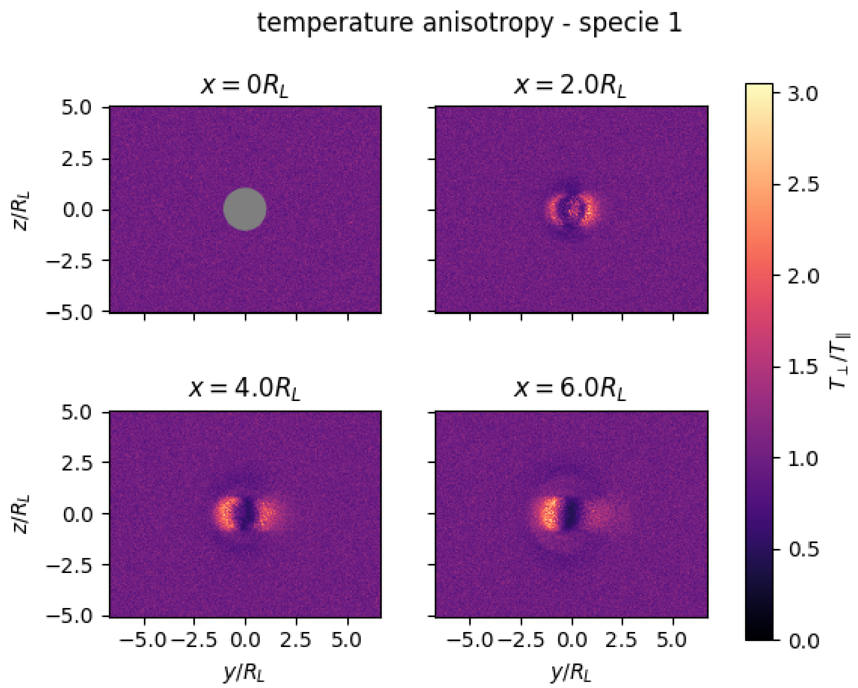

Figure 5.27: Temperature anisotropy of H+ ions: transversal sections at $x = 0, x = 2R_L, x = 4R_L, 6 = R_L$

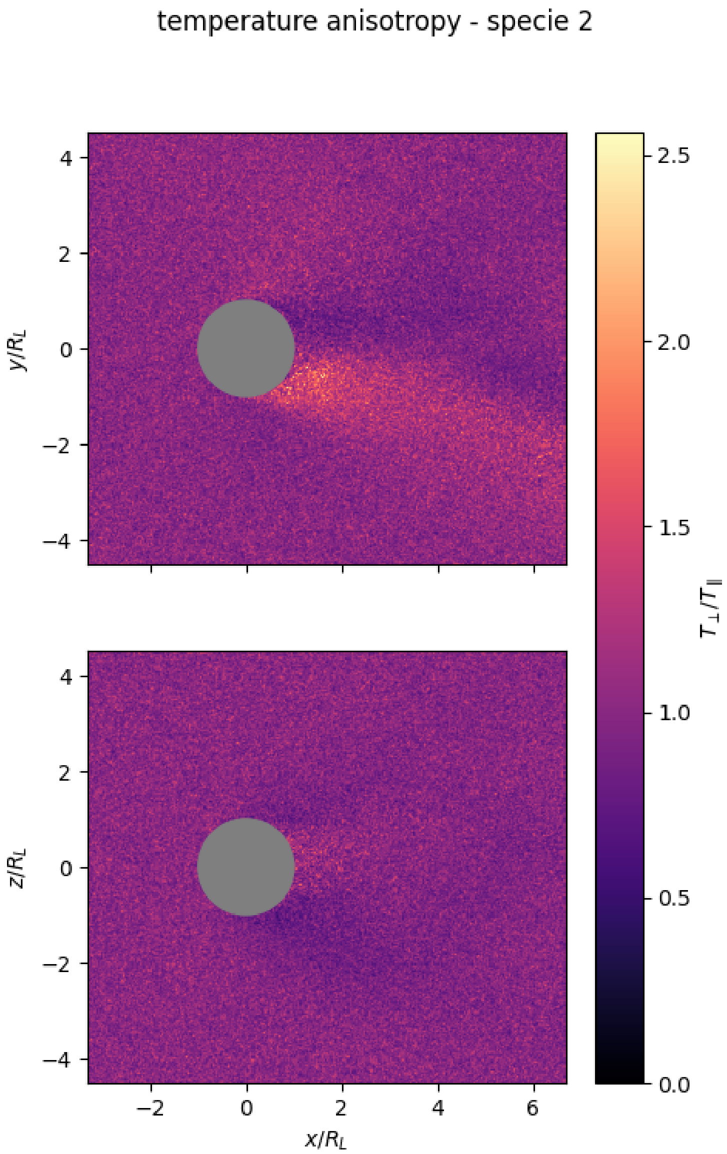

Figure 5.28: Temperature anisotropy of He++ ions: top − xy plane at $z = 0$, bottom xz plane at $y = 0$

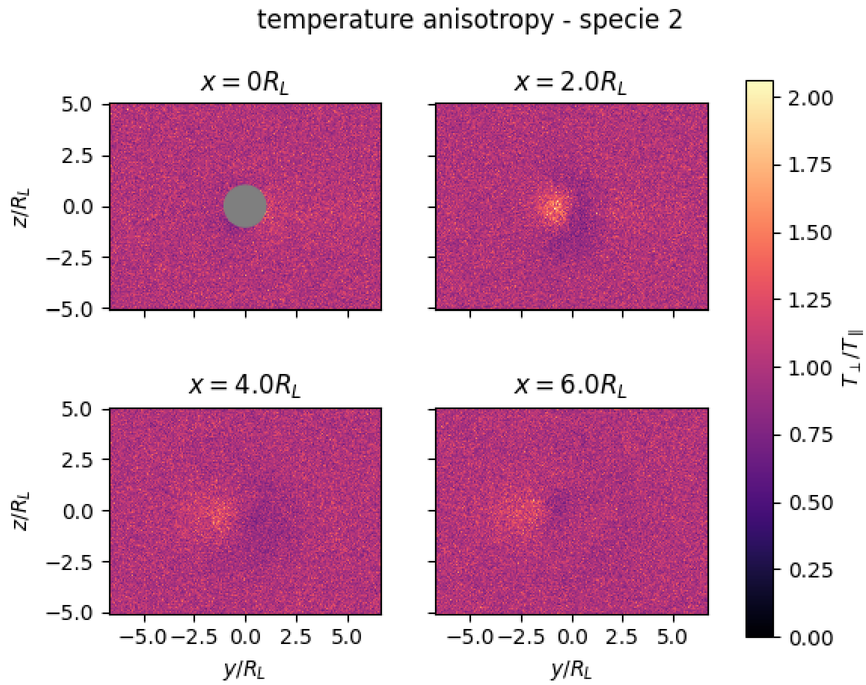

Figure 5.29: Temperature anisotropy of He++ ions: transversal sections at $x = 0, x = 2R_L, x = 4R_L, 6 = R_L$

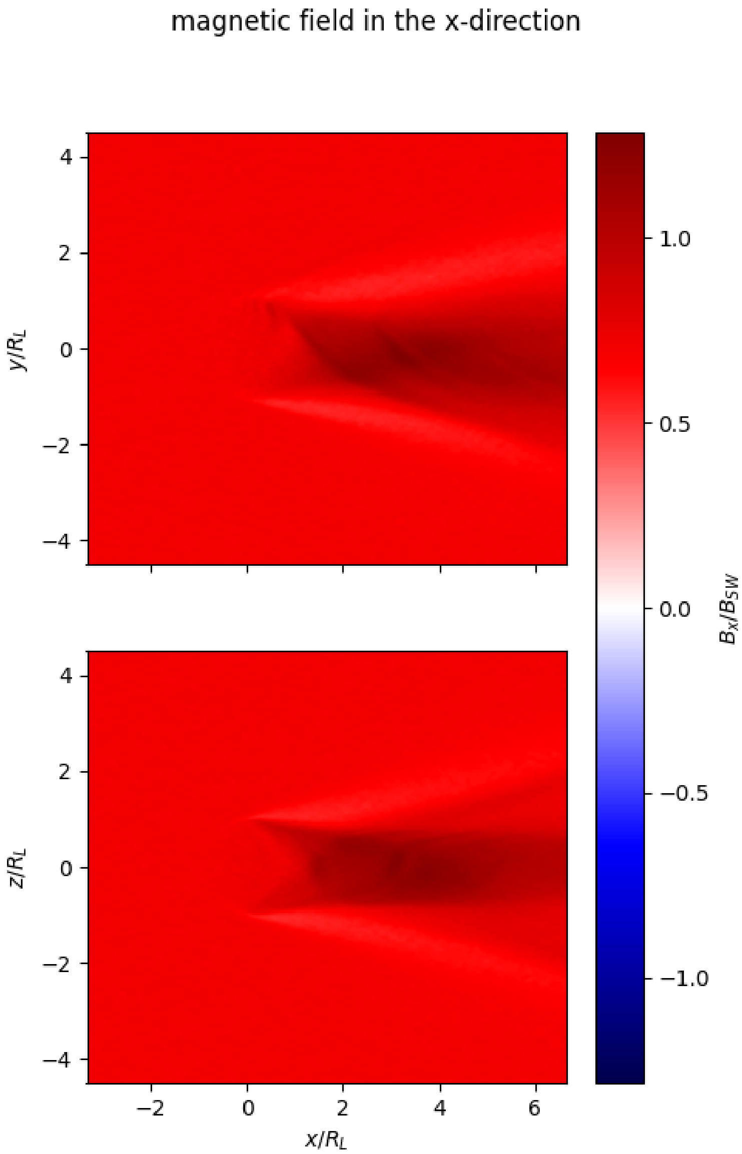

Figure 5.30: x-component of the magnetic field: top – xy plane at $z = 0$, bottom xz plane at $y = 0$

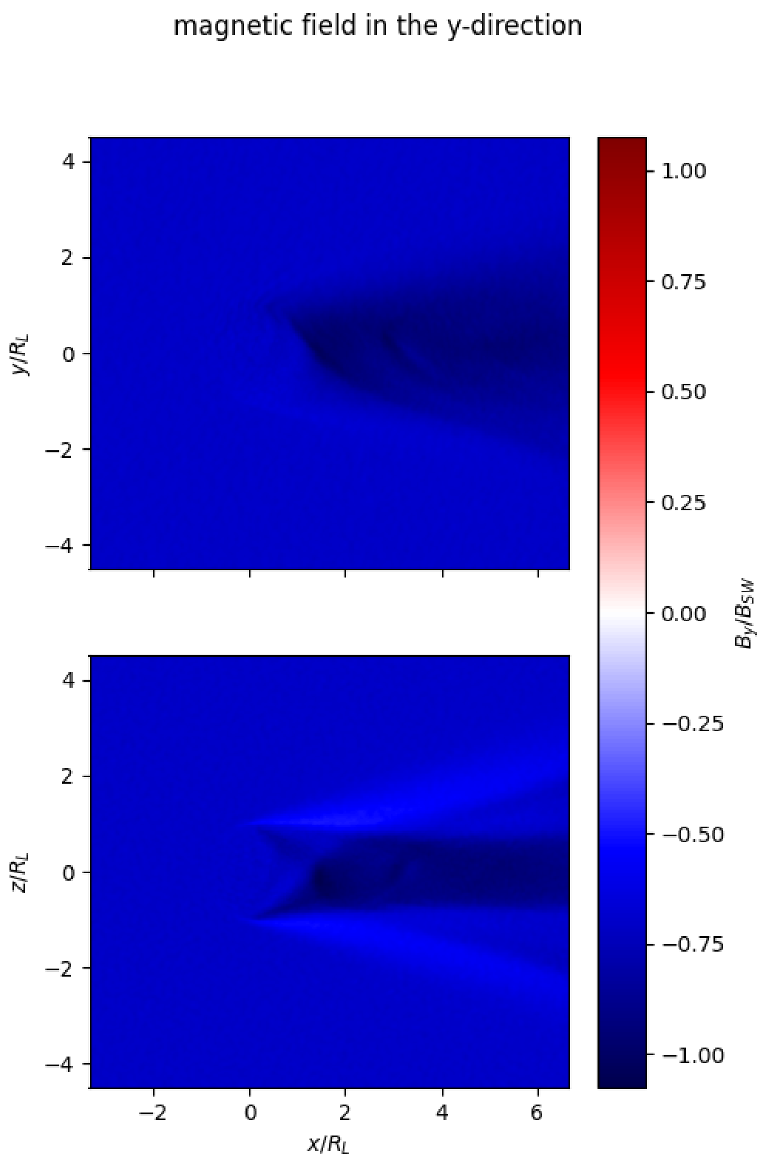

Figure 5.31: y-component of the magnetic field: top – xy plane at $z = 0$, bottom xz plane at $y = 0$

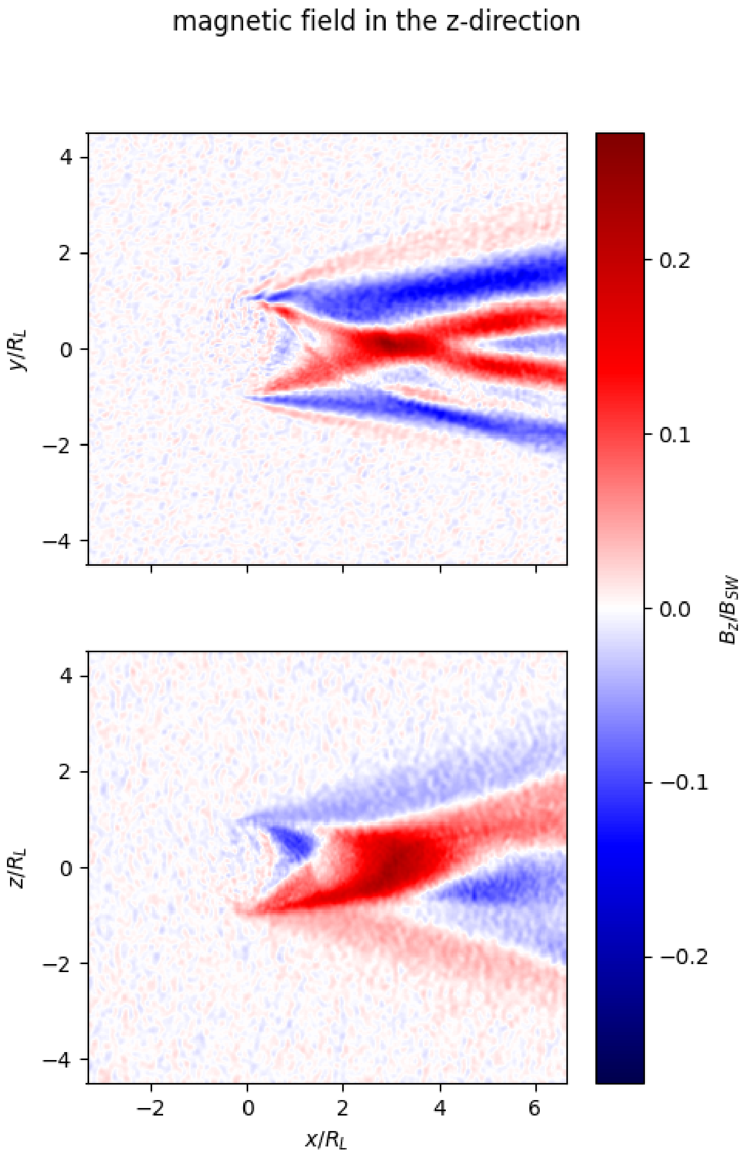

Figure 5.32: z-component of the magnetic field: top – xy plane at $z = 0$, bottom xz plane at $y = 0$

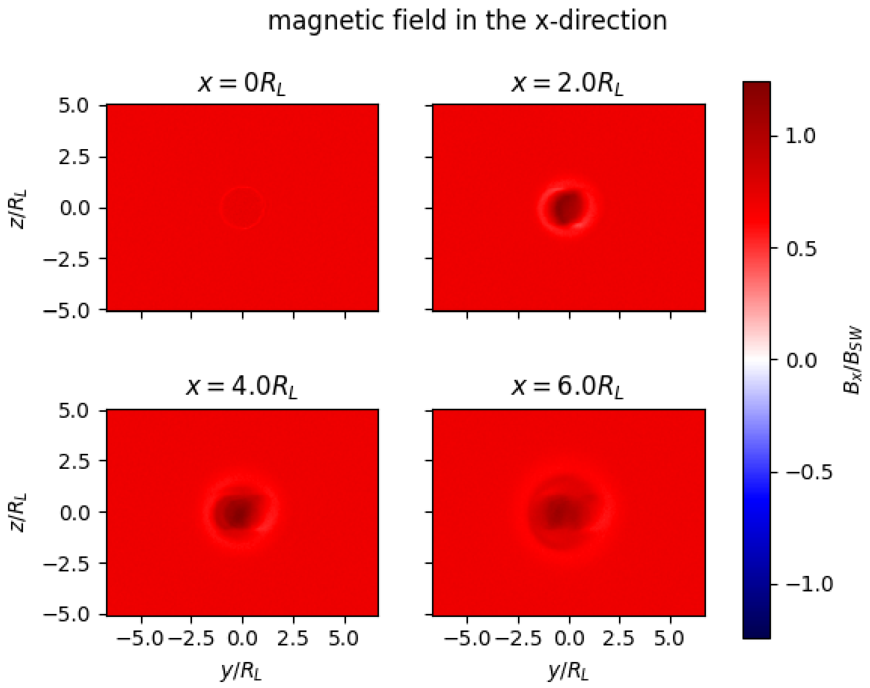

Figure 5.33: x-component of the magnetic field: transversal sections at $x = 0, x = 2R_L, x = 4R_L, 6 = R_L$

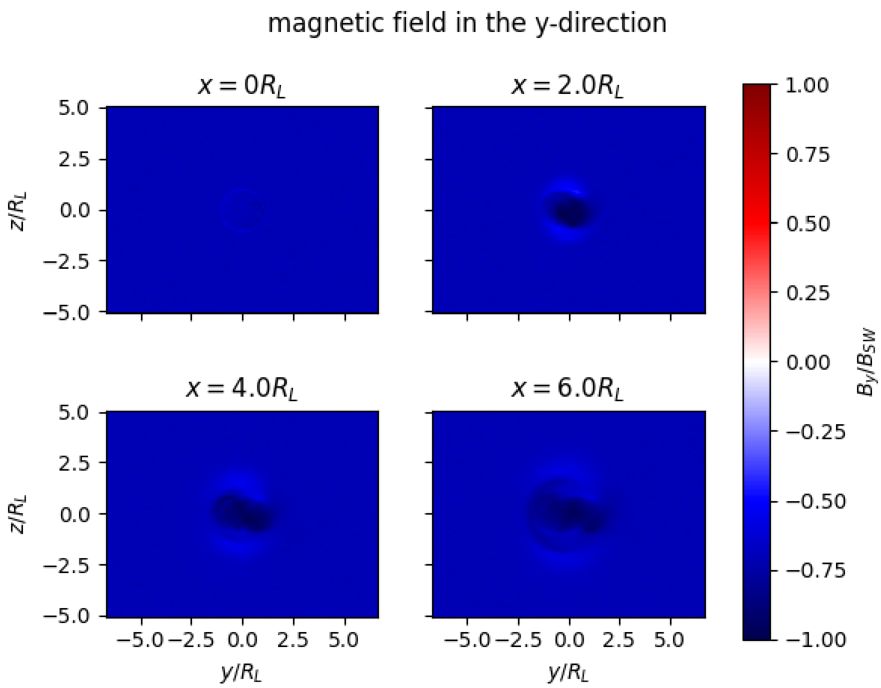

Figure 5.34: y-component of the magnetic field: transversal sections at $x = 0, x = 2R_L, x = 4R_L, 6 = R_L$

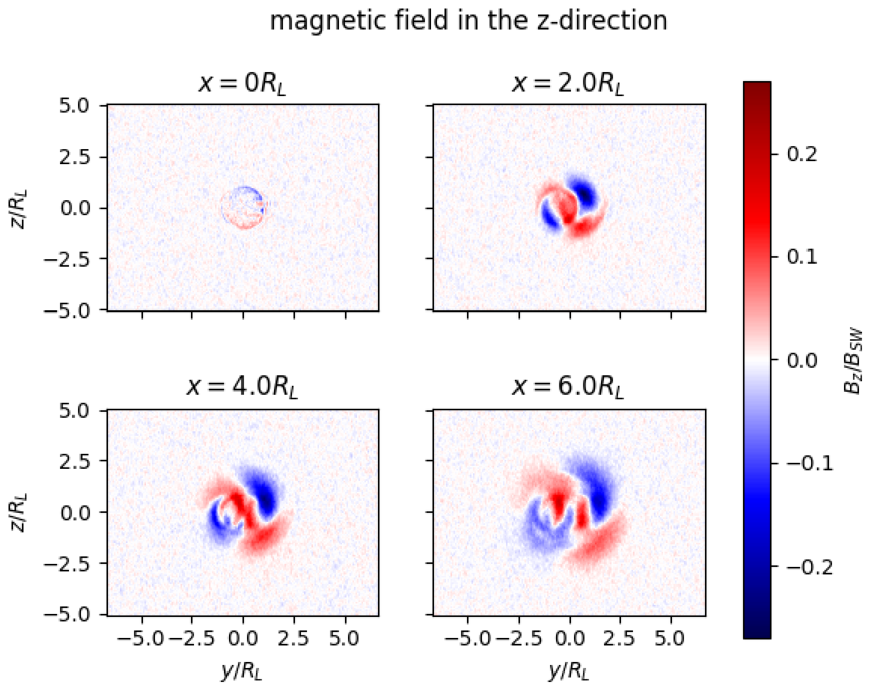

Figure 5.35: z-component of the magnetic field: transversal sections at $x = 0, x = 2R_L, x = 4R_L, 6 = R_L$

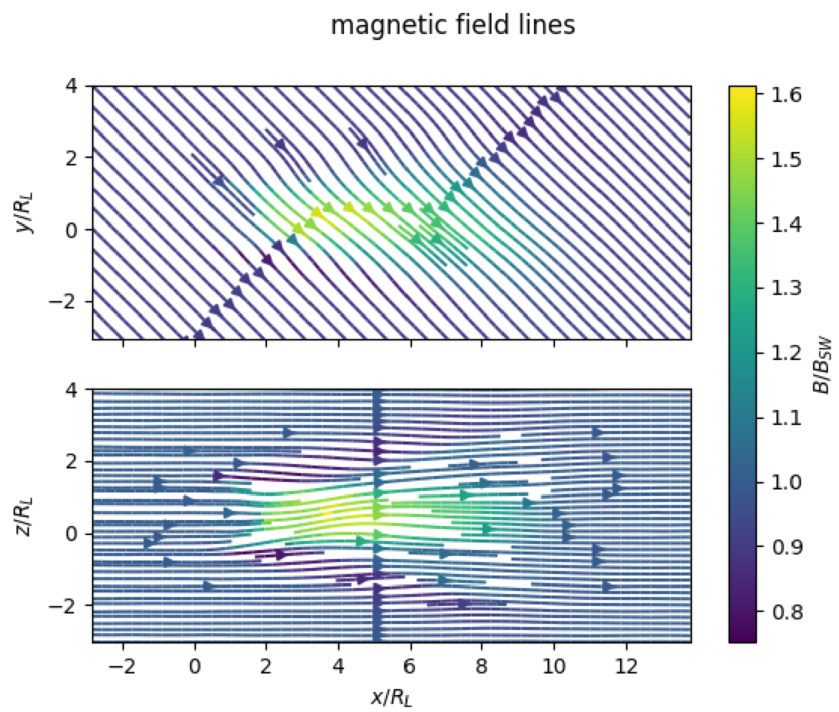

Figure 5.36: Graph of magnetic field lines: top – xy plane at $z = 0$, bottom xz plane at $y = 0$

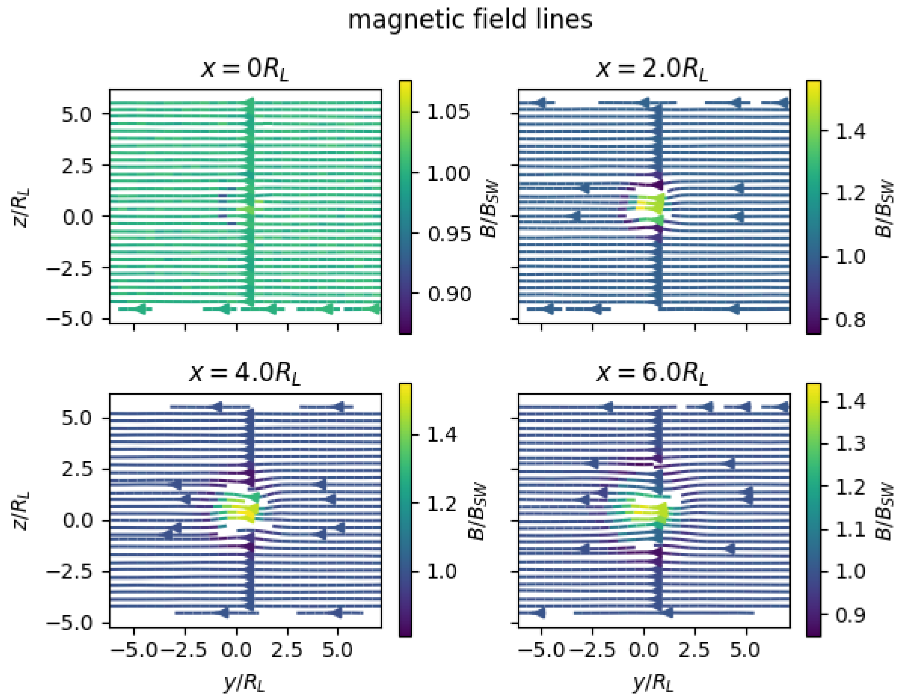

Figure 5.37: Graph of magnetic field lines: transversal sections at $x = 0, x = 2R_L, x = 4R_L, 6 = R_L$

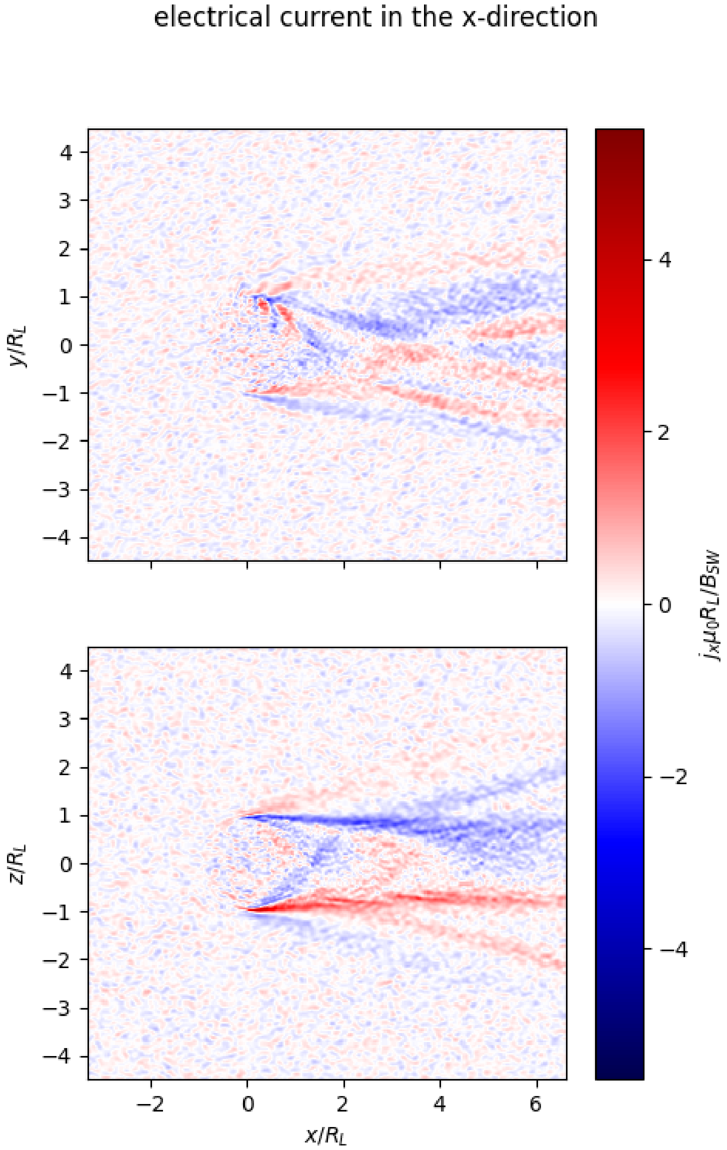

Figure 5.38: x-component of electrical current: top – xy plane at $z = 0$, bottom xz plane at $y = 0$

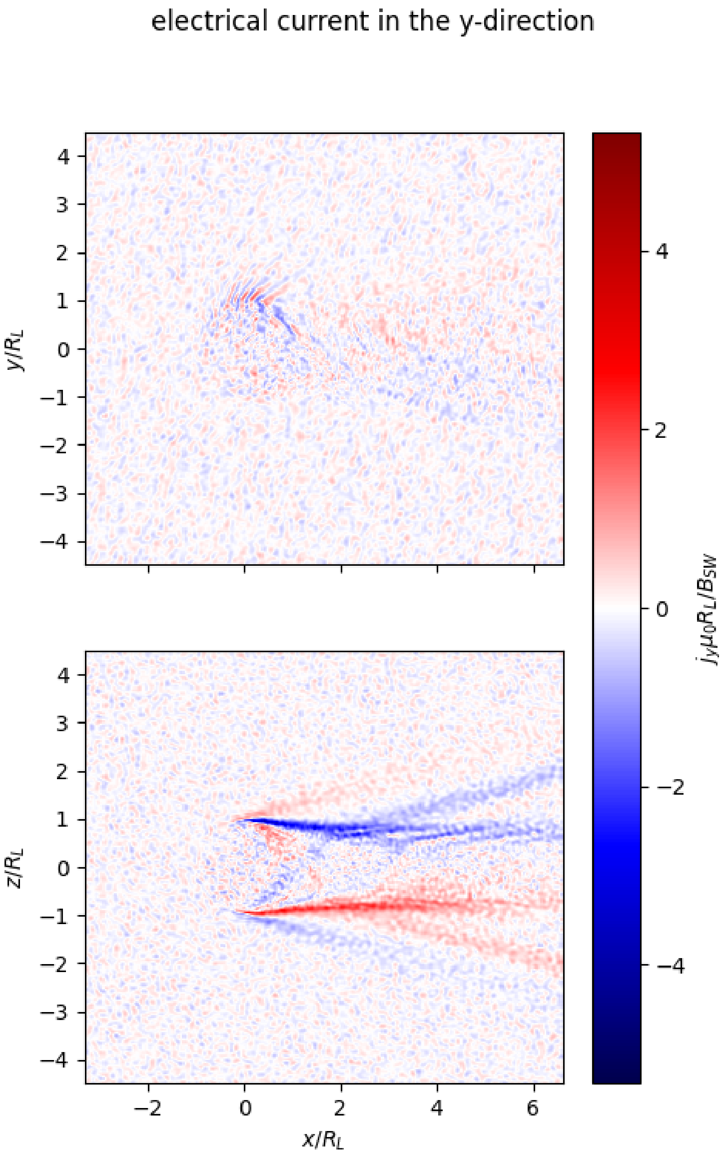

Figure 5.39: y-component of the magnetic field: top – xy plane at $z = 0$, bottom xz plane at $y = 0$

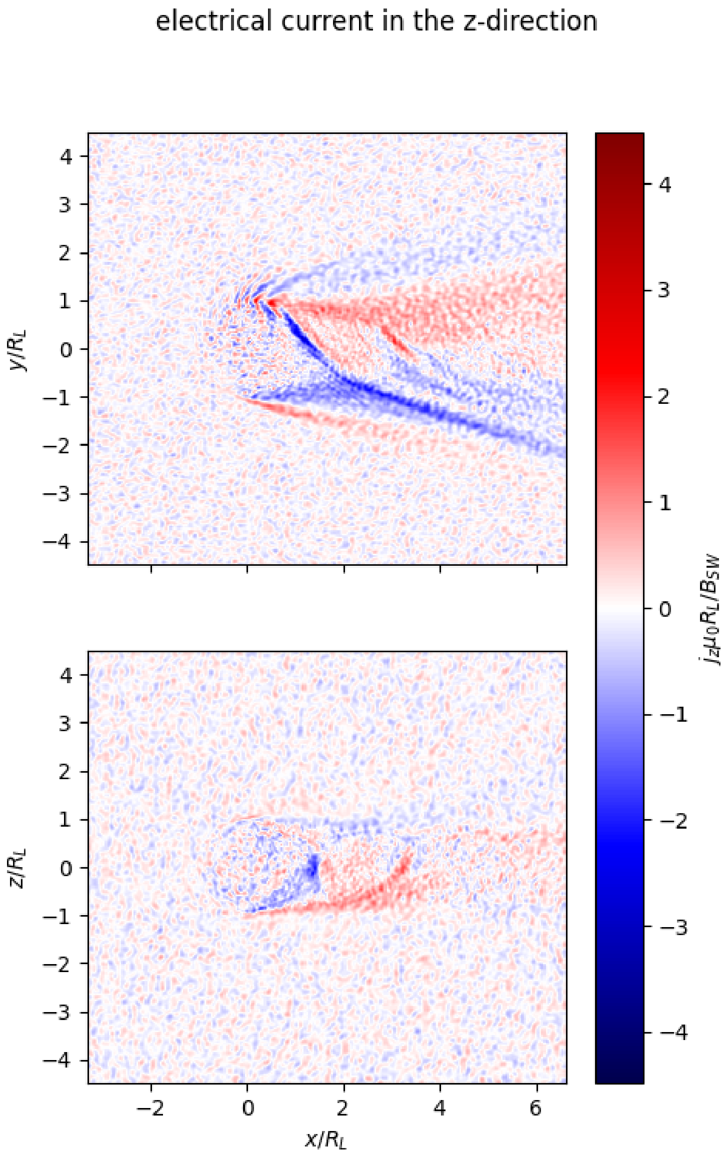

Figure 5.40: z-component of electrical current: top – xy plane at $z = 0$, bottom xz plane at $y = 0$

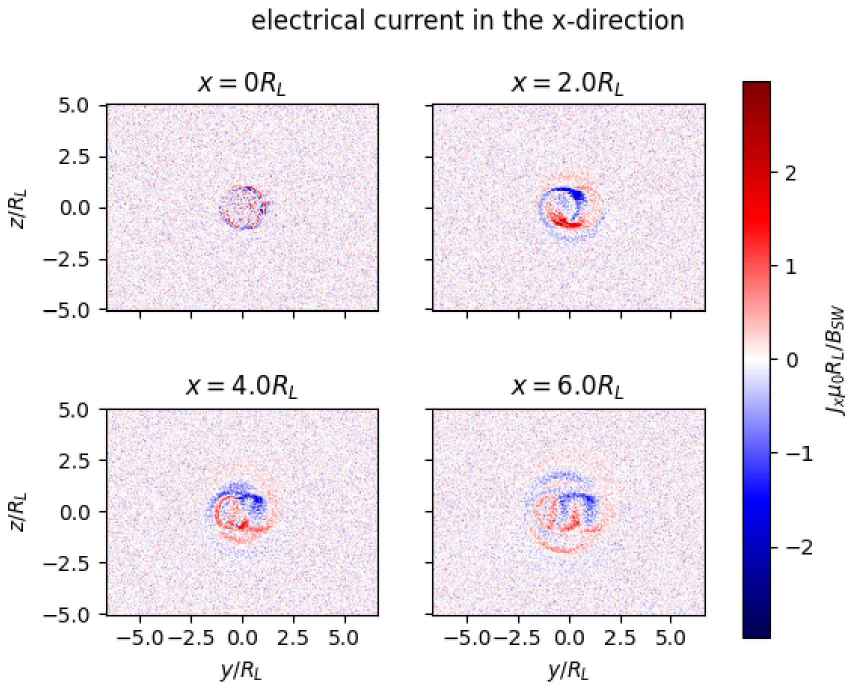

Figure 5.41: x-component of electrical current: transversal sections at $x = 0, x = 2R_L, x = 4R_L, 6 = R_L$

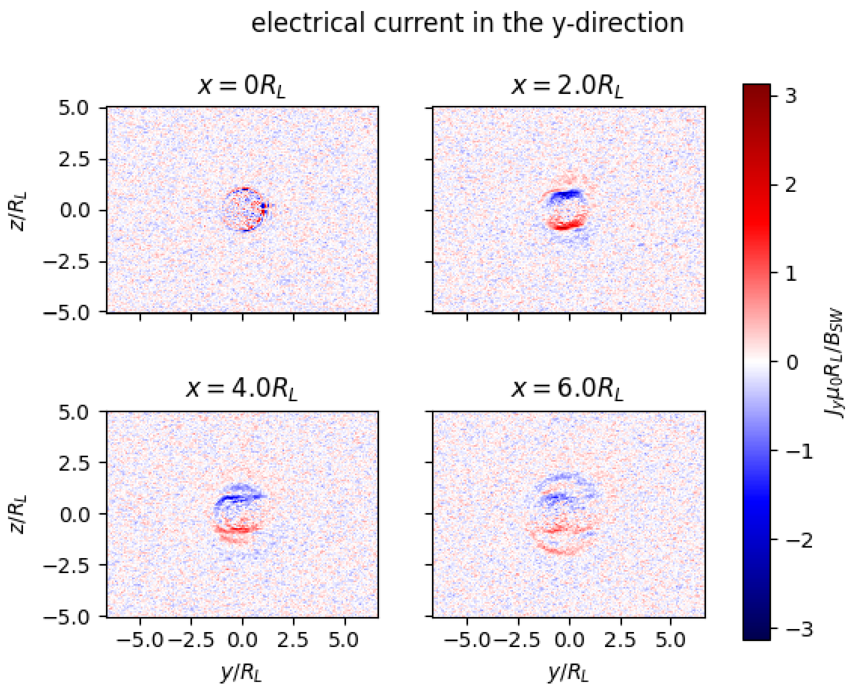

Figure 5.42: y-component of electrical current: transversal sections at $x = 0, x = 2R_L, x = 4R_L, 6 = R_L$

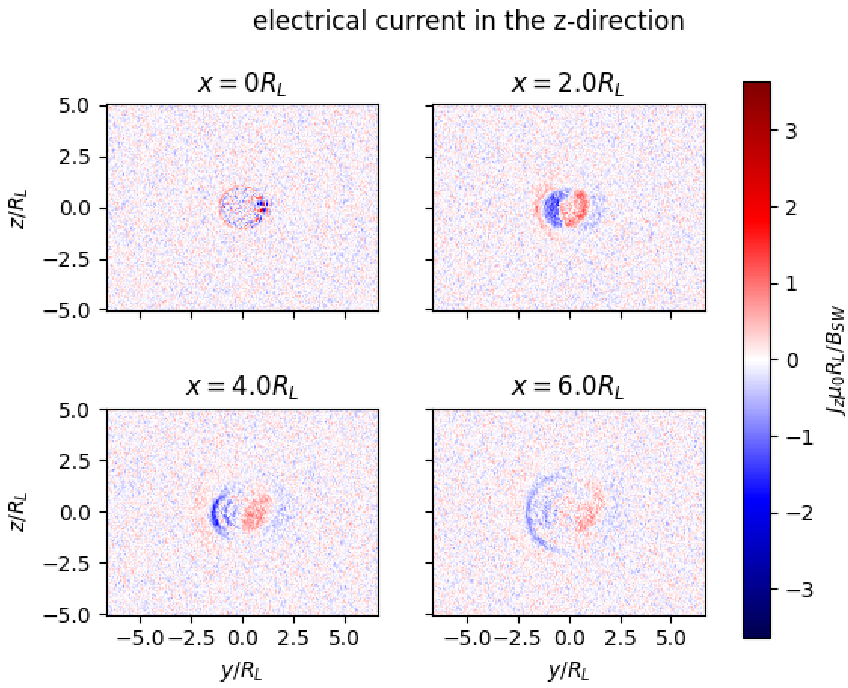

Figure 5.43: z-component of electrical current: transversal sections at $x = 0, x = 2R_L, x = 4R_L, 6 = R_L$

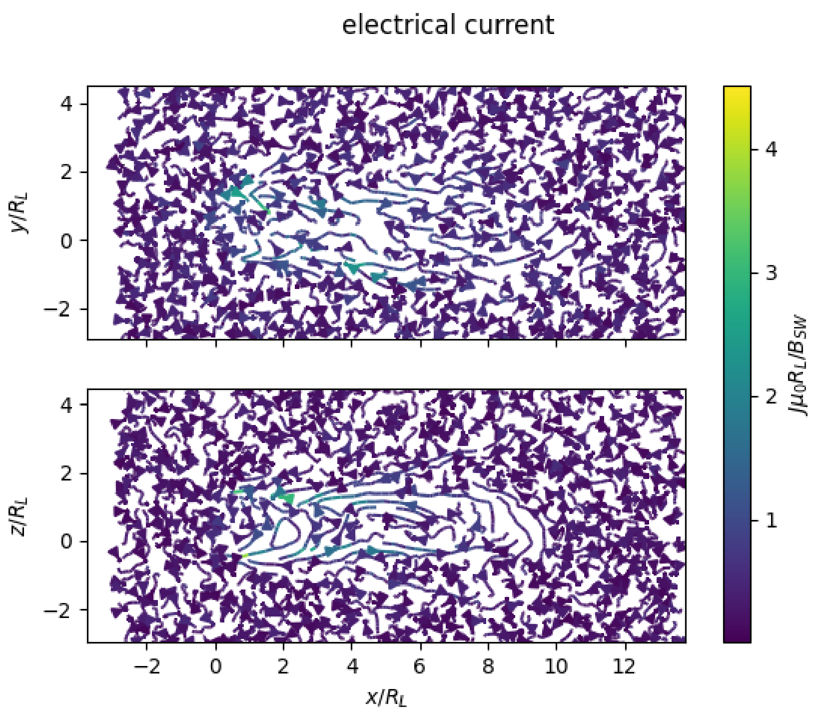

Figure 5.44: Graph of electric current: top – xy plane at $z = 0$, bottom xz plane at $y = 0$

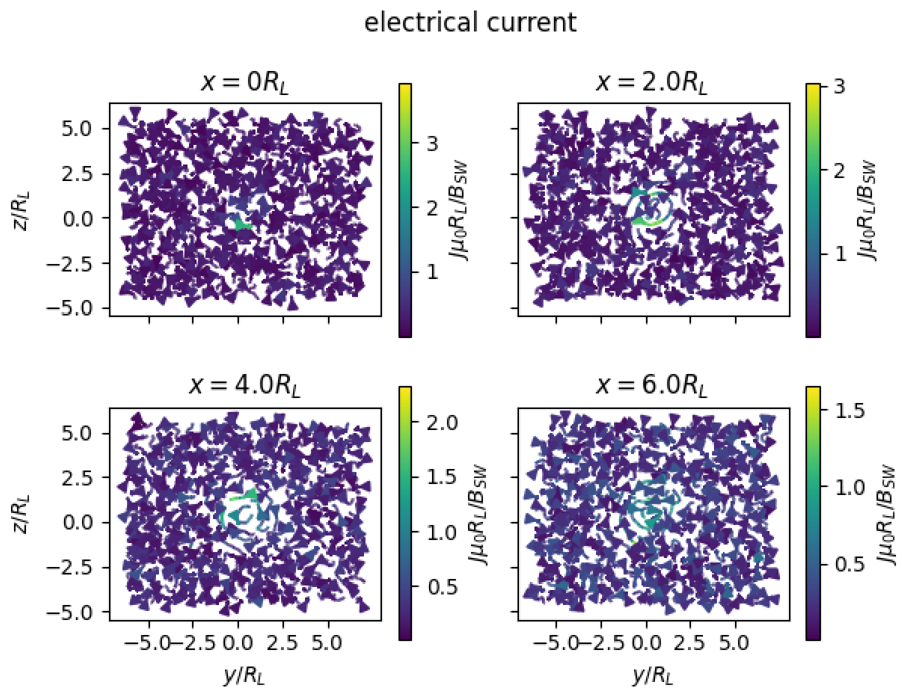

Figure 5.45: Graph of electric current: transversal sections at $x = 0, x = 2R_L, x = 4R_L, 6 = R_L$

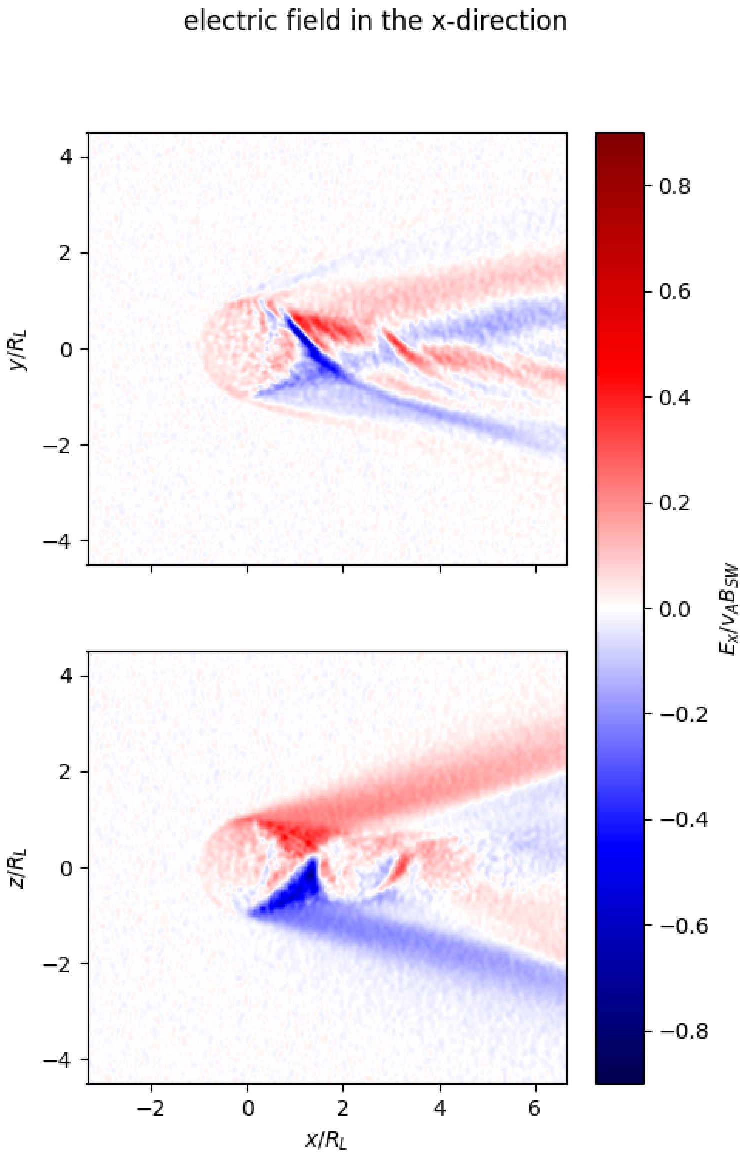

Figure 5.46: x-component of electric field: top − xy plane at $z = 0$, bottom xz plane at $y = 0$

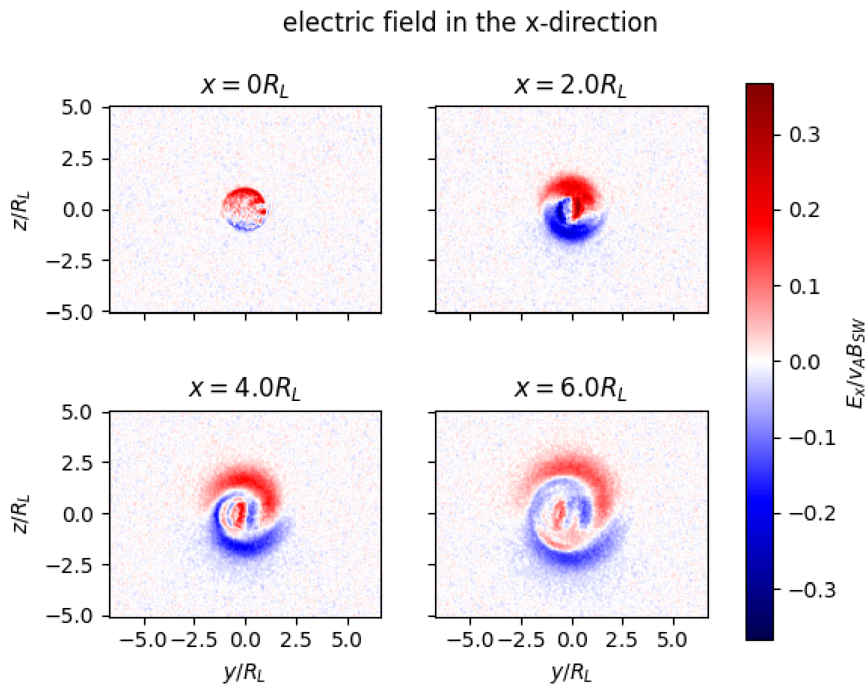

Figure 5.47: x-component of electric field: transversal sections at $x = 0, x = 2R_L, x = 4R_L, 6 = R_L$

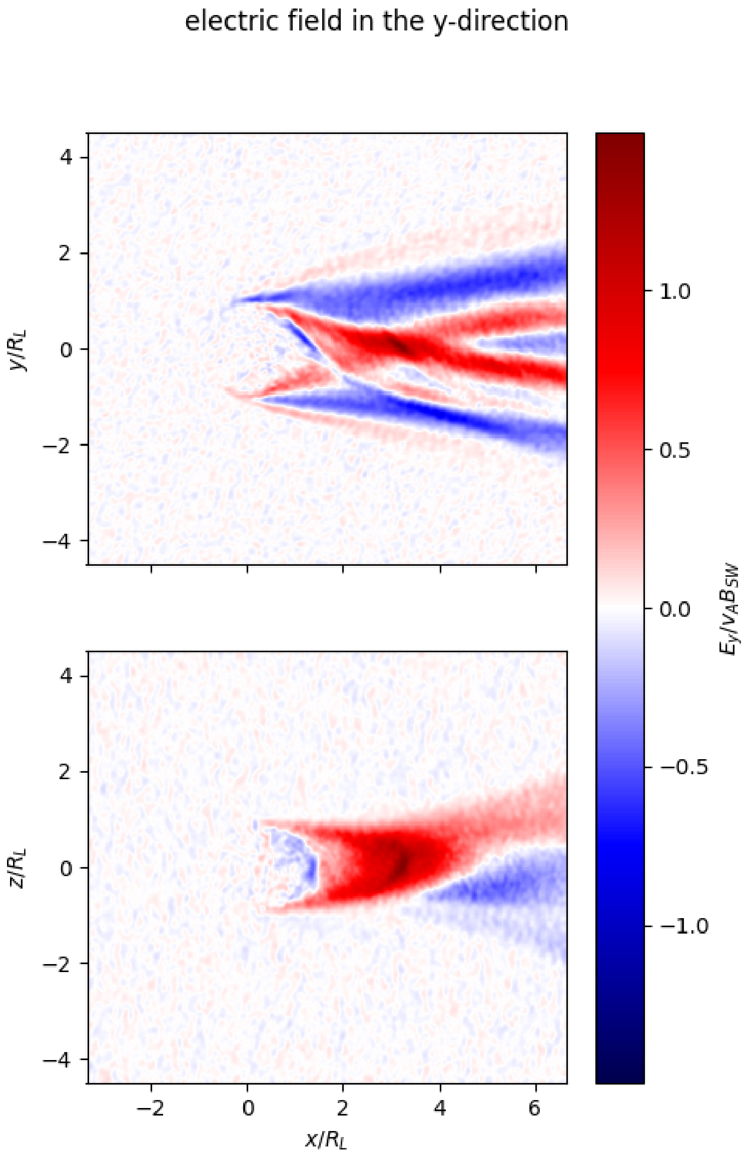

Figure 5.48: y-component of electric field: top – xy plane at $z = 0$, bottom xz plane at $y = 0$

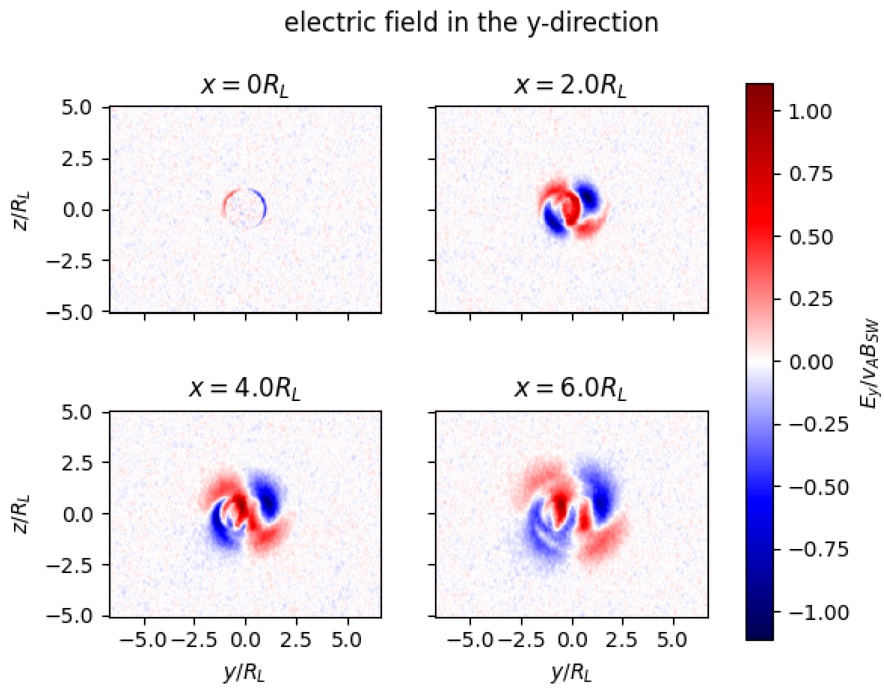

Figure 5.49: y-component of electric field: transversal sections at $x = 0, x = 2R_L, x = 4R_L, 6 = R_L$

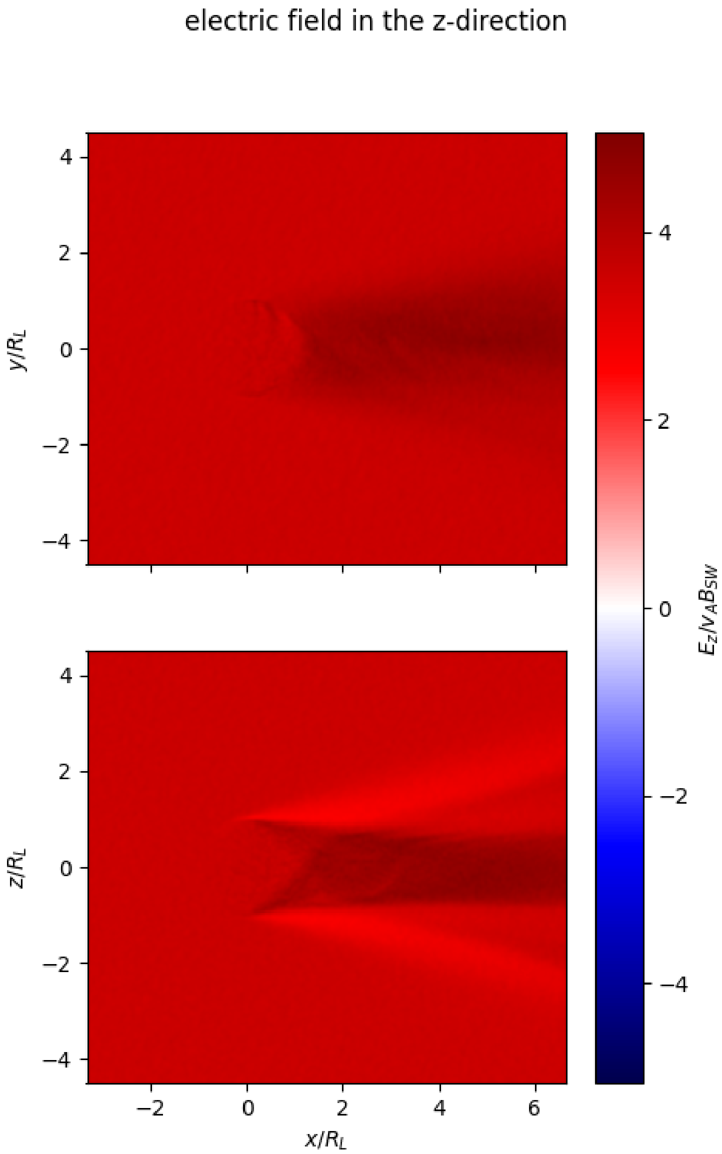

Figure 5.50: z-component of electric field: top $-$ xy plane at $z = 0$, bottom xz plane at $y = 0$

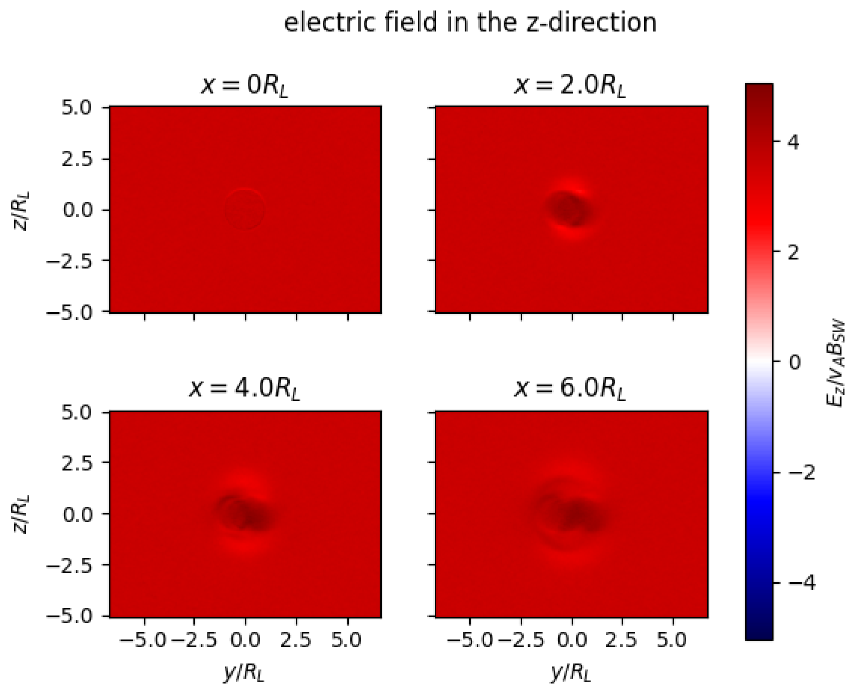

Figure 5.51: z-component of electric field: transversal sections at $x = 0, x = 2R_L, x = 4R_L, 6 = R_L$

Chapter 6

Summary

In this work, a hybrid numerical model was used for the case of Lunar interaction with solar wind. Two phenomena were studied – the influence of a resistive crust and/or conducting core on the lunar interaction with the solar wind; and the influence of a relative movement of hydrogen and helium species. Three models were employed to modify the resistivity of a spherical layer within the Moon:

1. the layer of modified resistivity is inserted without handling the interface – the interface is a step function,
2. the layer of modified resistivity is connected to the background using a spherical ramp – a linear function,
3. the layer of modified resistivity and the background are replaced by a tangent hyperbolic function of radius.

For further description, see Chapter 4. The parameters of the spherical layer can be set using the simulation initialization file, meaning that the layers can be set arbitrarily – this allows the user to simulate the conducting layers within bodies such as Europa, Ganymede, Mercury.

The effect of the introduction of a resistive layer was studied using seven 2D simulations, where one served as a control, three had a layer of increased resistivity introduced in the crust, and three had a layer of decreased resistivity introduced in the core. The model reached of the stability of the numerical scheme for high resistivity – this limit can be bypassed using a higher spatial or temporal resolution at the cost of computational difficulty.

The lunar wake structure of ion charge density does not seem to be affected when layers with modified resistivity are employed – see 5.1. The plasma void (area of very low charge density in the centre of the near wake) in the lunar wake is filled from both sides of the wake and is refilled at approximately $x \approx 5R_{\mathrm{L}}$ regardless of the resistivity set in the model – neither a highly conducting core, or a highly resistive crust seem to have a significant effect. All simulations produce a Mach cone of the same apex angle of 14°. However, there were perturbations in the magnetic field prominent on the surface of the Mach cone due to the introduction of a highly resistive crust in the model. See the graph of differences between configurations 3 (highly resistive crust) and 1 (control) – Fig. 5.2, 5.4 and 5.6. These perturbations are however comparable in magnitude to the noise produced by the procedure of randomly removing ions incident on the lunar surface. The three models employed all affected the stability of the simulation in the same way. However, there was a significant difference between the models with regard to their computational expensiveness – the model employing linear function on the interface between the layers with different resistivity is significantly slower, while the other two models were comparable in speed. There was also a difference in the influence on the magnetic field itself, where the linear model impacted the magnetic field more – see Figs. 5.2, 5.4 and 5.6. This is likely due to the ramp it introduces on the interface between the background and the layer with modified resistivity, which makes the layer thicker overall. A 3D model can be employed to study the influence of high crustal resistivity on the model further. Temporal changes in the external magnetic field may be interesting to study as well – it is expected to affect the magnetic field in the case of the highly conducting Lunar core.

The interaction of a solar wind including He++ ions was studied using a 3D hybrid numerical simulations whose parameters can be seen in 5. The lunar wake is bifurcated due to the bulk velocities of the H+ and He++ species being in different directions. The main features of the single specie interaction are preserved in the two specie case. Because the ratio of the charge densities of the species is 20, the interaction is mainly driven by the hydrogen specie. There are seemingly no distinct differences in the features of the magnetic field between the two specie model and a one specie simulation. The H+ ion specie charge has generally similar features to the the ion charge density structures in the case of a simulation of only H+ specie solar wind interaction with the Moon. The plasma cavity produced in the wake as ions are absorbed by the lunar surface is refilled primarily in the y direction – along magnetic field lines. All perturbations are bound by Mach cone with the apex angle approximately equal to 14°. Further down the wake, there is a compression region surrounding the central plasma cavity. The cavity formed by helium ions appears to be refilled by hydrogen ions moving along the magnetic field lines, as is evidenced by the y component of the bulk velocity of hydrogen ions. The H+ ions within the rarefaction cone have low $T_\perp/T_\parallel$. He++ ions' $T_\perp/T_\parallel$ ratio is enhanced in an area that stretches in a direction that seems to be a greater angle (with respect to x axis) than the direction of the bulk velocity of He++ ions in the solar wind. A longer simulation may reveal more information as the wake structure becomes longer. The magnetic field wake structure does not differ significantly from a single specie simulation magnetic wake field structure, the x and y components of the magnetic field are enhanced in the central part of the lunar wake and weakened in the rarefaction region. Around the central plasma cavity in the wake, there is a counter-clockwise electrical current (when viewed along x axis).

Bibliography

[1] Brian J. Anderson, Mario H. Acuña, Haje Korth, James A. Slavin, Hideharu Uno, Catherine L. Johnson, Michael E. Purucker, Sean C. Solomon, Jim M. Raines, Thomas H. Zurbuchen, George Gloeckler, and Ralph L. McNutt. The Magnetic Field of Mercury. *Space Science Reviews*, 152(1):307–339, May 2010.

[2] Brian J. Anderson, Catherine L. Johnson, Haje Korth, Michael E. Purucker, Reka M. Winslow, James A. Slavin, Sean C. Solomon, Ralph L. McNutt, Jim M. Raines, and Thomas H. Zurbuchen. The Global Magnetic Field of Mercury from MESSENGER Orbital Observations. *Science*, 333(6051):1859–1862, September 2011. Publisher: American Association for the Advancement of Science Section: Report.

[3] J. D. Anderson, E. L. Lau, W. L. Sjogren, G. Schubert, and W. B. Moore. Gravitational constraints on the internal structure of Ganymede. *Nature*, 384(6609):541–543, December 1996.

[4] J. D. Anderson, G. Schubert, R. A. Jacobson, E. L. Lau, W. B. Moore, and W. L. Sjogren. Europa's Differentiated Internal Structure: Inferences from Four Galileo Encounters. *Science*, 281(5385):2019–2022, September 1998.

[5] C. Aoshima and N. Namiki. Structures Beneath Lunar Basins: Estimates of Moho and Elastic Thickness from Local Analysis of Gravity and Topography. volume 32, March 2001. Conference Name: Lunar and Planetary Science Conference.

[6] A. L. Broadfoot, B. R. Sandel, D. E. Shemansky, J. C. McConnell, G. R. Smith, J. B. Holberg, S. K. Atreya, T. M. Donahue, D. F. Strobel, and J. L. Bertaux. Overview of the Voyager ultraviolet spectrometry results through Jupiter encounter. *Journal of Geophysical Research: Space Physics*, 86(A10):8259–8284, September 1981. Publisher: John Wiley & Sons, Ltd.

[7] R. W. Carlson, J. C. Bhattacharyya, B. A. Smith, T. V. Johnson, B. Hidayat, S. A. Smith, G. E. Taylor, B. O'Leary, and R. T. Brinkmann. An Atmosphere on Ganymede from Its Occultation of SAO 186800 on 7

June 1972. *Science*, 182(4107):53–55, October 1973. Publisher: American Association for the Advancement of Science Section: Reports.

[8] P. Dyal, C. W. Parkin, and W. D. Daily. Structure of the lunar interior from magnetic field measurements. volume 7, pages 3077–3095, April 1976.

[9] Aharon Eviatar, Vytenis M. Vasyliūnas, and Donald A. Gurnett. The ionosphere of Ganymede. *Planetary and Space Science*, 49(3):327–336, March 2001.

[10] S. Fatemi, H. A. Fuqua, A. R. Poppe, G. T. Delory, J. S. Halekas, W. M. Farrell, and M. Holmström. On the confinement of lunar induced magnetic fields. *Geophysical Research Letters*, 42(17):6931–6938, 2015. _eprint: https://agupubs.onlinelibrary.wiley.com/doi/pdf/10.1002/2015GL065576.

[11] S. Fatemi, M. Holmström, Y. Futaana, S. Barabash, and C. Lue. The lunar wake current systems. *Geophysical Research Letters*, 40(1):17–21, 2013. _eprint: https://agupubs.onlinelibrary.wiley.com/doi/pdf/10.1029/2012GL054635.

[12] S. Fatemi, N. Poirier, M. Holmström, J. Lindkvist, M. Wieser, and S. Barabash. A modelling approach to infer the solar wind dynamic pressure from magnetic field observations inside Mercury's magnetosphere. *Astronomy & Astrophysics*, 614:A132, June 2018. Publisher: EDP Sciences.

[13] S. Fatemi, A. R. Poppe, K. K. Khurana, M. Holmström, and G. T. Delory. On the formation of Ganymede's surface brightness asymmetries: Kinetic simulations of Ganymede's magnetosphere. *Geophysical Research Letters*, 43(10):4745–4754, 2016. _eprint: https://agupubs.onlinelibrary.wiley.com/doi/pdf/10.1002/2016GL068363.

[14] Shahab Fatemi, Mats Holmström, Yoshifumi Futaana, Charles Lue, Michael R. Collier, Stas Barabash, and Gabriella Stenberg. Effects of protons reflected by lunar crustal magnetic fields on the global lunar plasma environment. *Journal of Geophysical Research: Space Physics*, 119(8):6095–6105, 2014. _eprint: https://agupubs.onlinelibrary.wiley.com/doi/pdf/10.1002/2014JA019900.

[15] Shahab Fatemi, Charles Lue, Mats Holmström, Andrew R. Poppe, Martin Wieser, Stas Barabash, and Gregory T. Delory. Solar wind plasma interaction with Gerasimovich lunar magnetic anomaly. *Journal of Geophysical Research: Space Physics*, 120(6):4719–4735, 2015. _eprint: https://agupubs.onlinelibrary.wiley.com/doi/pdf/10.1002/2015JA021027.

[16] Y. Futaana, S. Barabash, M. Wieser, C. Lue, P. Wurz, A. Vorburger, A. Bhardwaj, and K. Asamura. Remote energetic neutral atom imaging of electric potential over a lunar magnetic

anomaly. *Geophysical Research Letters*, 40(2):262–266, 2013. _eprint: https://agupubs.onlinelibrary.wiley.com/doi/pdf/10.1002/grl.50135.

[17] Karl-Heinz Glassmeier, Jan Grosser, Uli Auster, Dragos Constantinescu, Yasuhito Narita, and Stephan Stellmach. Electromagnetic Induction Effects and Dynamo Action in the Hermean System. *Space Science Reviews*, 132(2):511–527, October 2007.

[18] J. S. Halekas, G. T. Delory, D. A. Brain, R. P. Lin, and D. L. Mitchell. Density cavity observed over a strong lunar crustal magnetic anomaly in the solar wind: A mini-magnetosphere? *Planetary and Space Science*, 56(7):941–946, May 2008.

[19] D. T. Hall, P. D. Feldman, M. A. McGrath, and D. F. Strobel. The Far-Ultraviolet Oxygen Airglow of Europa and Ganymede. *The Astrophysical Journal*, 499(1):475, May 1998. Publisher: IOP Publishing.

[20] M. Holmstrom. Handling vacuum regions in a hybrid plasma solver. *arXiv:1301.0272 [physics]*, January 2013. arXiv: 1301.0272.

[21] M. Holmström, S. Fatemi, Y. Futaana, and H. Nilsson. The interaction between the Moon and the solar wind. *Earth, Planets and Space*, 64(2):237–245, February 2012. Number: 2 Publisher: SpringerOpen.

[22] M. Holmström, M. Wieser, S. Barabash, Y. Futaana, and A. Bhardwaj. Dynamics of solar wind protons reflected by the Moon. *Journal of Geophysical Research: Space Physics*, 115(A6), 2010. _eprint: https://agupubs.onlinelibrary.wiley.com/doi/pdf/10.1029/2009JA014843.

[23] Lon L. Hood and Natalia A. Artemieva. Antipodal effects of lunar basin-forming impacts: Initial 3D simulations and comparisons with observations. *Icarus*, 193(2):485–502, February 2008.

[24] Lon L. Hood, David L. Mitchell, Robert P. Lin, Mario H. Acuna, and Alan B. Binder. Initial measurements of the lunar induced magnetic dipole moment using Lunar Prospector Magnetometer data. *Geophysical Research Letters*, 26(15):2327–2330, 1999. _eprint: https://agupubs.onlinelibrary.wiley.com/doi/pdf/10.1029/1999GL900487.

[25] Lon L. Hood, Nicola C. Richmond, and Paul D. Spudis. Origin of strong lunar magnetic anomalies: Further mapping and examinations of LROC imagery in regions antipodal to young large impact basins. *Journal of Geophysical Research: Planets*, 118(6):1265–1284, 2013. _eprint: https://agupubs.onlinelibrary.wiley.com/doi/pdf/10.1002/jgre.20078.

[26] Wing-Huen Ip and Andreas Kopp. Resistive MHD simulations of Ganymede's magnetosphere 2. Birkeland currents and particle energetics. *Journal of Geophysical Research: Space Physics*, 107(A12):SMP 42–1–SMP 42–7, 2002. _eprint: https://agupubs.onlinelibrary.wiley.com/doi/pdf/10.1029/2001JA005072.

[27] R. Jarvinen, M. Alho, E. Kallio, P. Wurz, S. Barabash, and Y. Futaana. On vertical electric fields at lunar magnetic anomalies. *Geophysical Research Letters*, 41(7):2243–2249, 2014. _eprint: https://agupubs.onlinelibrary.wiley.com/doi/pdf/10.1002/2014GL059788.

[28] R. Jaumann, H. Hiesinger, M. Anand, I. A. Crawford, R. Wagner, F. Sohl, B. L. Jolliff, F. Scholten, M. Knapmeyer, H. Hoffmann, H. Hussmann, M. Grott, S. Hempel, U. Köhler, K. Krohn, N. Schmitz, J. Carpenter, M. Wieczorek, T. Spohn, M. S. Robinson, and J. Oberst. Geology, geochemistry, and geophysics of the Moon: Status of current understanding. *Planetary and Space Science*, 74(1):15–41, December 2012.

[29] Xianzhe Jia, James A. Slavin, Tamas I. Gombosi, Lars K. S. Daldorff, Gabor Toth, and Bart van der Holst. Global MHD simulations of Mercury's magnetosphere with coupled planetary interior: Induction effect of the planetary conducting core on the global interaction. *Journal of Geophysical Research: Space Physics*, 120(6):4763–4775, 2015. _eprint: https://agupubs.onlinelibrary.wiley.com/doi/pdf/10.1002/2015JA021143 tex.ids: Jia2015a.

[30] Xianzhe Jia, Raymond J. Walker, Margaret G. Kivelson, Krishan K. Khurana, and Jon A. Linker. Three-dimensional MHD simulations of Ganymede's magnetosphere. *Journal of Geophysical Research: Space Physics*, 113(A6), 2008. _eprint: https://agupubs.onlinelibrary.wiley.com/doi/pdf/10.1029/2007JA012748.

[31] Xianzhe Jia, Raymond J. Walker, Margaret G. Kivelson, Krishan K. Khurana, and Jon A. Linker. Properties of Ganymede's magnetosphere inferred from improved three-dimensional MHD simulations. *Journal of Geophysical Research: Space Physics*, 114(A9), 2009. _eprint: https://agupubs.onlinelibrary.wiley.com/doi/pdf/10.1029/2009JA014375.

[32] Bradley L. Jolliff, Jeffrey J. Gillis, Larry A. Haskin, Randy L. Korotev, and Mark A. Wieczorek. Major lunar crustal terranes: Surface expressions and crust-mantle origins. *Journal of Geophysical Research: Planets*, 105(E2):4197–4216, 2000. _eprint: https://agupubs.onlinelibrary.wiley.com/doi/pdf/10.1029/1999JE001103.

[33] K. Kabin, M. R. Combi, T. I. Gombosi, D. L. DeZeeuw, K. C. Hansen, and K. G. Powell. Io's magnetospheric interaction: an MHD model with day-night asymmetry. *Planetary and Space Science*, 49(3):337–344, March 2001.

[34] Krishan K. Khurana, Margaret G. Kivelson, Kevin P. Hand, and C. T. Russell. Electromagnetic Induction from Europa's Ocean and the Deep Interior. In Robert T. Pappalardo and William B. McKinnon, editors, *Europa*. University of Arizona Press, 2009.

[35] M. Kivelson. The Magnetosphere of Ganymede (Invited). In *AGU Fall Meeting Abstracts*, volume 12, pages SM12B–01, December 2013.

[36] M. G. Kivelson, K. K. Khurana, D. J. Stevenson, L. Bennett, S. Joy, C. T. Russell, R. J. Walker, C. Zimmer, and C. Polanskey. Europa and Callisto: Induced or intrinsic fields in a periodically varying plasma environment. *Journal of Geophysical Research: Space Physics*, 104(A3):4609–4625, 1999. _eprint: https://agupubs.onlinelibrary.wiley.com/doi/pdf/10.1029/1998JA900095.

[37] M. G. Kivelson, K. K. Khurana, and M. Volwerk. The Permanent and Inductive Magnetic Moments of Ganymede. *Icarus*, 157(2):507–522, June 2002.

[38] M. G. Kivelson and C. T. Russell, editors. *Introduction to space physics*. Cambridge University Press, Cambridge ; New York, 1995.

[39] Margaret G. Kivelson, Fran Benegal, William S. Kurth, Fritz M. Neubauer, Chris Paranicas, and Joachim Saur. Magnetospheric Interactions with Satellites. In Fran Bagenal, Timothy Dowling, and William McKinnon, editors, *Jupiter: The planet, satellites and magnetosphere*, page 732. Cambridge University Press, December 2006. tex.chapter: Magnetospheric Interactions with Satellites tex.ean: 9780521035453.

[40] Andreas Kopp and Wing-Huen Ip. Resistive MHD simulations of Ganymede's magnetosphere 1. Time variabilities of the magnetic field topology. *Journal of Geophysical Research: Space Physics*, 107(A12):SMP 41–1–SMP 41–5, 2002. _eprint: https://agupubs.onlinelibrary.wiley.com/doi/pdf/10.1029/2001JA005071.

[41] R. P. Lin, D. L. Mitchell, D. W. Curtis, K. A. Anderson, C. W. Carlson, J. McFadden, M. H. Acuña, L. L. Hood, and A. Binder. Lunar Surface Magnetic Fields and Their Interaction with the Solar Wind: Results from Lunar Prospector. *Science*, 281(5382):1480–1484, September 1998. Publisher: American Association for the Advancement of Science Section: Report.

[42] A. S. Lipatov, J. F. Cooper, W. R. Paterson, E. C. Sittler, R. E. Hartle, and D. G. Simpson. Jovian plasma torus interaction with Europa: 3D hybrid kinetic simulation. First results. *Planetary and Space Science*, 58(13):1681–1691, November 2010.

[43] Charles Lue, Yoshifumi Futaana, Stas Barabash, Martin Wieser, Mats Holmström, Anil Bhardwaj, M. B. Dhanya, and Peter Wurz. Strong influence of lunar crustal fields on the solar wind flow. *Geophysical Research Letters*, 38(3), 2011. _eprint: https://agupubs.onlinelibrary.wiley.com/doi/pdf/10.1029/2010GL046215.

[44] J. G. Luhmann. Plasma interactions with unmagnetized bodies. In Margaret G. Kivelson and Christopher T.Editors Russell, editors, *Introduction to space physics*, pages 203–226. Cambridge University Press, 1995. tex.place: Cambridge.

[45] Yosio Nakamura, Gary Latham, David Lammlein, Maurice Ewing, Frederick Duennebier, and James Dorman. Deep lunar interior inferred from recent seismic data. *Geophysical Research Letters*, 1(3):137–140, 1974. _eprint: https://agupubs.onlinelibrary.wiley.com/doi/pdf/10.1029/GL001i003p00137.

[46] Yosio Nakamura, Gary V. Latham, and H. James Dorman. Apollo Lunar Seismic Experiment—Final summary. In *Proceedings of the Thirteenth Lunar and Planetary Science Conference*, pages A117–A123. John Wiley & Sons, Ltd, November 1982.

[47] M. D. Norman, R. A. Duncan, and J. J. Huard. Imbrium provenance for the Apollo 16 Descartes terrain: Argon ages and geochemistry of lunar breccias 67016 and 67455. *Geochimica et Cosmochimica Acta*, 74(2):763–783, January 2010.

[48] A. R. Poppe, J. S. Halekas, C. Lue, and S. Fatemi. ARTEMIS observations of the solar wind proton scattering function from lunar crustal magnetic anomalies. *Journal of Geophysical Research: Planets*, 122(4):771–783, 2017. _eprint: https://agupubs.onlinelibrary.wiley.com/doi/pdf/10.1002/2017JE005313.

[49] Michael E. Purucker and Joseph B. Nicholas. Global spherical harmonic models of the internal magnetic field of the Moon based on sequential and coestimation approaches. *Journal of Geophysical Research: Planets*, 115(E12), 2010. _eprint: https://agupubs.onlinelibrary.wiley.com/doi/pdf/10.1029/2010JE003650.

[50] C. T. Russell and R. J. Walker. The magnetospheres of the outer planets. In Margaret G. Kivelson and Christopher T.Editors Russell, editors, *Introduction to space physics*, pages 503–520. Cambridge University Press, 1995. tex.place: Cambridge.

[51] Yoshifumi Saito, Masaki N. Nishino, Masaki Fujimoto, Tadateru Yamamoto, Shoichiro Yokota, Hideo Tsunakawa, Hidetoshi Shibuya, Masaki Matsushima, Hisayoshi Shimizu, and Futoshi Takahashi. Simultaneous observation of the electron acceleration and ion deceleration over lunar magnetic anomalies. *Earth, Planets and Space*, 64(2):83–92, February 2012. Number: 2 Publisher: SpringerOpen.

[52] Joachim Saur, Fritz M. Neubauer, and Karl-Heinz Glassmeier. Induced magnetic fields in solar system bodies. *Space Science Reviews*, 152(1-4):391–421, December 2009. tex.publisher: Springer Nature.

[53] C. P. Sonett. Electromagnetic induction in the Moon. *Reviews of Geophysics*, 20(3):411–455, 1982. _eprint: https://agupubs.onlinelibrary.wiley.com/doi/pdf/10.1029/RG020i003p00411.

[54] Sabine Stanley and Gary A. Glatzmaier. Dynamo Models for Planets Other Than Earth. *Space Science Reviews*, 152(1):617–649, May 2010.

[55] S. M. Tikoo, B. P. Weiss, M. Fuller, J. Gattacceca, D. L. Shuster, and T. L. Grove. The decline of the ancient lunar core dynamo. In *AGU Fall Meeting Abstracts*, volume 51, pages GP51B–03, December 2012.

[56] Pavel Trávníček, Petr Hellinger, and David Schriver. Structure of Mercury's magnetosphere for different pressure of the solar wind: Three dimensional hybrid simulations. *Geophysical Research Letters*, 34(5), 2007. _eprint: https://agupubs.onlinelibrary.wiley.com/doi/pdf/10.1029/2006GL028518.

[57] Pavel Trávníček, Petr Hellinger, David Schriver, and Stuart D. Bale. Structure of the lunar wake: Two-dimensional global hybrid simulations. *Geophysical Research Letters*, 32(6), 2005. _eprint: https://agupubs.onlinelibrary.wiley.com/doi/pdf/10.1029/2004GL022243.

[58] Hideyuki Usui, Yohei Miyake, Masaki N. Nishino, Takuma Matsubara, and Joseph Wang. Electron dynamics in the minimagnetosphere above a lunar magnetic anomaly. *Journal of Geophysical Research: Space Physics*, 122(2):1555–1571, 2017. _eprint: https://agupubs.onlinelibrary.wiley.com/doi/pdf/10.1002/2016JA022927.

[59] R. J. Walker and C. T. Russell. Solar-wind interactions with magnetized planets. In Margaret G. Kivelson and Christopher T.Editors Russell, editors, *Introduction to space physics*, pages 164–182. Cambridge University Press, 1995. tex.place: Cambridge.

[60] Y. C. Wang, J. Müller, W. H. Ip, and U. Motschmann. A 3D hybrid simulation study of the electromagnetic field distributions in the lunar wake. *Icarus*, 216(2):415–425, December 2011.

[61] B. P. Weiss, C. R. Suavet, S. M. Tikoo, D. L. Shuster, J. Gattacceca, and M. Fuller. The Lunar Core Dynamo. In *AGU Fall Meeting Abstracts*, volume 34, pages P34B–01, December 2012.

[62] Mark A. Wieczorek, Bradley L. Jolliff, Amir Khan, Matthew E. Pritchard, Benjamin P. Weiss, James G. Williams, Lon L. Hood, Kevin Righter, Clive R. Neal, Charles K. Shearer, I. Stewart McCallum, Stephanie Tompkins, B. Ray Hawke, Chris Peterson, Jeffrey J. Gillis, and Ben Bussey. The Constitution and Structure of the Lunar Interior. *Reviews in Mineralogy and Geochemistry*, 60(1):221–364, January 2006. Publisher: GeoScienceWorld.